Optical Fiber Sensors for Temperature and Strain Measurement

by

Dapeng Zhou

A thesis
presented to the University of Waterloo
in fulfillment of the
thesis requirement for the degree of
Doctor of Philosophy
in
Physics

Waterloo, Ontario, Canada, 2010

I hereby declare that I am the sole author of this thesis. This is a true copy of the thesis, including any required final revisions, as accepted by my examiners.

I understand that my thesis may be made electronically available to the public.

Abstract

Optical fiber sensors have already been developed from the experimental stage to practical applications in the past 20 years. There is no doubt that this technology can bring a wealth of applications, ranging from sensors in medical industry, aerospace and wind-energy industries, through to distributed sensors in oil and gas industry. Among a large amount of physical and chemical parameters which optical fiber sensors could measure, temperature and strain are the most widely studied. This thesis presents several low-cost optical fiber sensor configurations primarily for temperature and strain measurement.

Several basic optical fiber components which are good candidates as optical fiber sensors are used in our experiments, such as fiber Bragg gratings (FBGs), multimode fibers (MMFs), small-core dispersion compensation fibers (SCDCFs), high-birefringence fiber loop mirrors (HBFLMs), and polarization-maintaining photonic crystal fibers (PMPCFs). Temperature and strain cross sensitivity is a crucial issue when designing high performance optical fiber sensors, since most of the sensing components are both sensitive to temperature and strain. This would introduce an error when measuring each of them independently. We developed several schemes to overcome this problem by cascading an FBG and a section of MMF, inserting an FBG into an HBFLM, and space division multiplexing two HBFLMs. By measuring the wavelength shifts of the two independent components' spectra in each scheme, simultaneous measurement of temperature and strain could be achieved. However, all the above schemes need optical spectrum analyzers to monitor the spectral information, which increases the cost of the system and limits the operation speed. In order to avoid using optical spectrum analyzers, we use an intensity-based interrogation method with MMFs and HBFLMs as edge filters. By measuring power ratio changes, instead of monitoring spectra shifts, simultaneous measurement of temperature and strain could be realized with a low cost and high speed. The resolutions of the above five configurations are between $0.26 - 1.2$ °C in temperature and $9.21 - 29.5$ $\mu\varepsilon$ in strain, which are sufficient for certain applications.

We also investigate the sensing applications with the SCDCF. Since the cutoff wavelength of this kind of fiber is around 1663 nm, which makes it naturally an MMF in the wavelength range of 1550 nm. By slightly offsetting the core of the SCDCF with respect to that of the standard single-mode fiber (SMF), a high extinction ratio could be achieved with almost 9 dB. When a lateral force (lateral strain) applied on the SCDCF, extinction ratio will decrease. The change of the extinction ratio is almost independent of temperature variation. The measured extinction ratio change has a good quadratic relationship with respect to applied lateral force. This feature could be used to measure lateral force (lateral strain). In addition, we also use this feature to realize simultaneous measurement of both the longitudinal strain and lateral strain, since the applied longitudinal strain results in the whole spectrum shift. Moreover, a miniature high temperature sensor could also be

made using the SCDCF. One end of a 4-mm long SCDCF is spliced directly to SMF with the other end cleaved. By monitoring the reflection spectrum of the SCDCF, temperature information could be obtained. This sensing head is very compact and could realize high temperature measurement up to 600 °C.

Recently, a kind of PMPCF has been found to have very small responses to temperature change. This offers an opportunity to measure other parameters without considering temperature influence. We construct a compact 7-mm long transmission-type sensor with this kind of PMPCF. The interference spectrum generated by the coupling of cladding modes and core mode is obtained by slightly offsetting the PMPCF core to SMF core. The experiment shows that the interference spectrum is almost unchanged within the temperature range of $25 - 60$ °C. The presented sensor has the potential to be used to measure strain and refractive index in the normal environment without temperature discrimination for practical applications.

Acknowledgements

I would like to thank my supervisors, Prof. Wing-Ki Liu and Prof. Li Wei, for their guidance and patience over the past four years. They are always willing to help whenever I have problems with my study, research, and everyday life. I am so impressed by Prof. Liu's solid and profound theoretical knowledge, and I appreciate his encouragement and support. When I am working in the lab, Prof. Wei is always available to guide me, give suggestions, and share her ideas with me, which greatly help me develop a thorough understanding of the subject. I really enjoy working with them. I am so lucky that I have both of them as my supervisors, and I have had a very happy life during my PhD study.

I very much appreciate Prof. David Yevick, Prof. Joseph Sanderson, and Prof. Zoran Miskovic for being on my committee. During committee meetings and PhD qualifying examination, I benefit greatly from their questions and suggestions. I would also like to thank Prof. Donna Strickland, who gave me great support for my laser experiment and letting me work in her lab. My thanks go to Dr. Bo Dong, who joined our group in July 2008, for his great help and useful discussions. I would also like to thank Dr. Ying Jiang for his help with my simulation work, and Helen Fan who helped greatly for my experiment when she was working in our group as a summer student. I appreciate Dr. John W. Y. Lit for his support to our laboratory and my experiment. My thanks go to Judy McDonnell for her numerous help over the past four years. I would also like to thank Sharcnet for providing computer clusters to support my simulation work. Further, thank you to Prof. Xiaoyi Bao for examining my thesis and attending my defence.

Thank you to all my friends in Physics and Astronomy Department, Zijian Long, Wuyang Zhang, Ting Lu, Taoran Lin, Scott Mallais, Zheng Ma, Chunrong Wang, Ting Luo. I also have enjoyed the friendship outside the physics circle, who have made life very interesting; especially thank you to Anzuo Liu for being my best friend ever since we were kids.

I would like to express my gratitude to my parents and my wife for all the support for all these years!

My special thanks go to my supervisor for my Master's Degree study, Prof. You-Nian Wang who guided me to the journey of physics when I was a fourth year undergraduate student.

Dedication

To my parents and my wife.

Table of Contents

List of Tables **xii**

List of Figures **xviii**

Acronyms **xix**

1 Introduction **1**

1.1 Applications of Optical Fiber Sensors 2

1.1.1 Civil Applications 2

1.1.2 Medical Applications 5

1.1.3 Military Applications 6

1.2 Advantages of Optical Fiber Sensors 7

1.2.1 Electromagnetic Interference Immunity 7

1.2.2 High Sensitivity 7

1.2.3 Lightweight, Small Size, Environmental Ruggedness 8

1.2.4 Multiplexing and Distributed Capacities 8

1.3 Classifications of Optical Fiber Sensors 8

1.3.1 According to Application 10

1.3.2 According to Measurable Spatial Scope 10

1.3.3 According to Modulation Process 11

1.3.4 According to Technology 11

1.4 Thesis Content Summary 12

2 Basic Optical Fiber Sensor Technologies: Fiber Grating Sensors, Fiber Interferometer Sensors, and Measurands Discrimination 14

2.1 Fiber Grating Sensors 14

2.1.1 Classifications of Fiber Gratings 14

2.1.2 Principle of Fiber Bragg Grating Sensor 18

2.1.3 Fiber Bragg Grating Sensor Interrogation 19

2.2 Fiber Interferometer Sensors 23

2.2.1 Fabry-Pérot Interferometer Sensors 23

2.2.2 Fiber Mach-Zehnder Interferometer Sensors 25

2.2.3 Multimode Fiber Interferometer Sensors 26

2.2.4 High-Birefringence Fiber Loop Mirror Interferometer Sensors 28

2.3 Measurands Discrimination 29

3 Simultaneous Measurement of Strain and Temperature with Fiber Bragg Grating and Multimode Fibers 33

3.1 Introduction 33

3.2 FBG Cascades with MMF 35

3.2.1 Experiment Setup 35

3.2.2 Experiment Results and Discussion 37

3.3 MMF Serves as an Edge Filter 45

3.3.1 Operation Principle and Experiment Setup 45

3.3.2 Experiment and Discussion 47

3.4 Conclusion 51

4 Simultaneous Measurement of Strain and Temperature with Fiber Bragg Grating and High-Birefringence Fiber Loop Mirrors 52

4.1 Introduction 52

4.2 An FBG Inserts inside an HBFLM 54

4.2.1 Operation Principle and Experiment Setup 55

4.2.2 Experiment and Discussion 57

4.3 Space Division Multiplex HBFLMs 61

4.3.1 Operation Principle 61
4.3.2 Experiment Results and Discussions 63
4.4 HBFLM Serves as an Edge Filter 67
4.4.1 Experiment Setup and Operation Principle 67
4.4.2 Experiment and Discussion 69
4.5 Conclusion 72

5 Small Core Diameter Multimode Fiber Based Intermodal Interferometer and Its Applications in Fiber Sensors 73
5.1 Introduction 73
5.2 Temperature- and Phase-Independent Lateral Force Sensor 76
5.2.1 Operation Principle 76
5.2.2 Experiment Results and Discussions 79
5.3 Simultaneous Measurement of Transverse and Longitudinal Strains 82
5.3.1 Principle 83
5.3.2 Experiment Validation and Discussion 85
5.4 Lateral Force Sensor with Intensity-Based Interrogation Technique 90
5.4.1 Experiment Setup and Operation Principle 90
5.4.2 Experiment and Discussion 92
5.5 High-Temperature Measurement 94
5.5.1 Experiment Setup and Principle 94
5.5.2 Experiment Results and Discussion 97
5.6 Conclusion 98

6 Temperature Insensitive All-Fiber Compact Polarization-Maintaining Photonic Crystal Fiber Based Interferometer and Its Application in Fiber Sensors 100
6.1 Introduction 100
6.2 Principle 102
6.2.1 Structure of the PMPCF Interferometer and the Coupling Between the PMPCF and SMF 102

6.2.2 Sensing Principle of Temperature and Strain . . . 102
6.3 Experiment results and discussions . . . 104
6.3.1 Interference Spectrum Response to Temperature . . . 104
6.3.2 Interference Spectrum Response to Strain . . . 105
6.3.3 Interference Spectrum Response to RI . . . 105
6.4 Conclusion . . . 107

7 Future Work: Pulsed Fiber Lasers and Fully Distributed Fiber Sensors Based on Brillouin Scattering 108

7.1 Tunable Passively Q-Switched Erbium-Doped Fiber Laser with Single-Walled Carbon Nanotubes as a Saturable Absorber . . . 111
7.1.1 Introduction . . . 111
7.1.2 Experiment Setup . . . 112
7.1.3 Experimental Results and Discussion . . . 113
7.1.4 Conclusion . . . 116
7.2 Passively Mode-Locked Erbium-Doped Fiber Laser with Single-Walled Carbon Nanotubes as a Saturable Absorber . . . 116
7.2.1 Introduction . . . 116
7.2.2 Experiment and Discussion for Anomalous Dispersion Cavity . . . 117
7.2.3 Simulation and Experiment for Normal Dispersion Cavity . . . 120
7.3 Summary of Future Work . . . 123

APPENDICES 126

A Bragg Wavelength Shifts with Strain and Temperature 127

B Power Ratio Expression for Edge Filter Interrogation Technique of a Fiber Bragg Grating Sensor 129

C Properties of a Fabry-Pérot Interferometer 131

D Resonance Wavelength Shift of Multimode Fiber Interferometer with Temperature and Strain 133

E Transmission of a High-Birefringence Fiber Loop Mirror **135**

F Permissions **138**

References **139**

References for Chapter 1 139

References for Chapter 2 143

References for Chapter 3 149

References for Chapter 4 151

References for Chapter 5 154

References for Chapter 6 157

References for Chapter 7 158

List of Tables

3.1 Typical parameters and segment lengths of MMFs used in the experiment and wavelength spacing of the resultant interference spectrum 38

3.2 Center wavelength, reflectivity and optical bandwidth of the FBGs used in the experiment 38

3.3 Coefficient matrices, matrix condition number, and corresponding resolutions of strain and temperature for the combination of FBG_i + MMF_i . . . 44

4.1 The coefficient matrices and the corresponding resolutions of strain and temperature for the combination of FBG+HBFLM and of LPG+HBFLM in Ref. [4] 60

List of Figures

1.1 Oil and gas reservoirs are drained using several wells from one topside facility. The well heads can be located several kilometers from the platform below the sea. Based on data provided by distributed flow sensors and pT gauges, the production from each well and each zone within a well is controlled using downhole control valves. Reprinted by permission from Macmillan Publishers Ltd: Nature Photonics, 2:147-149, copyright 2008. . 2

1.2 The Airbus A380, the largest passenger aircraft in the world, uses composites extensively. Airbus is actively investigating the use of fibre-optic sensors on the A380. Reprinted by permission from Macmillan Publishers Ltd: Nature Photonics, 2:153-154, copyright 2008. 3

1.3 Optical sensors are being used to monitor the structural health of large composite structures such as turbine blades. Reprinted by permission from Macmillan Publishers Ltd: Nature Photonics, 2:143, copyright 2008. 4

1.4 Thanks to their miniature size, optical-fibre sensors have real potential in many medical applications, especially in the development of minimally invasive surgical tools. Reprinted by permission from Macmillan Publishers Ltd: Nature Photonics, 2:150-152, copyright 2008. 5

1.5 Basic optical fiber sensor configuration consisting of optical source, optical fiber, sensing head, and detector. 9

1.6 Extrinsic optical fiber sensors consisting of optical fiber that leads up to and out of a "black box" that modulated the light beam passing through it under environment change. 9

1.7 Intrinsic optical fiber sensors rely on the light beam propagating through the optical fiber modulated by the environmental effect directly. 10

2.1 Fiber Bragg grating: the variation of the refractive index in the fiber core is uniform along the axis; the modulation depth of the refractive index is constant. 15

2.2 Long-period fiber grating: the variation of the refractive index in the fiber core is uniform and along the axis; the modulation depth of the refractive index is constant; the periodicity is much longer than that of an FBG. . . . 15

2.3 Tilted fiber Bragg grating: the variation direction of the refractive index has an angel to the axis of the fiber core. 16

2.4 Chirped fiber Bragg grating: the variation of the refractive index in the fiber core is nonuniform and has a linear decreasing variation of the grating period. 17

2.5 Transmission of a linearly wavelength-dependent optical filter (edge filter) interrogator. FBG refers to the spectrum of the light reflected by a sensor FBG. 20

2.6 FBG sensor configuration with an edge filter as an interogator. 21

2.7 Fabry-Pérot interferometer, with P_i, P_r, and P_t the incident, reflected, and transmitted optical power, respectively. 24

2.8 Typical Fabry-Pérot interferometer reflection spectrum. 24

2.9 Configuration of a basic Mach-Zehnder interferometer, which consists of two 3-dB couplers, two arms with different length. 25

2.10 Typical transmission spectrum of an Mach-Zehnder interferometer. 26

2.11 Schematic of all-fiber multimode fiber interferometer. SMF: single-mode fiber; MMF: multimode fiber; OSA: optical spectrum analyzer. 27

2.12 Typical transmission spectrum of a multimode fiber interferometer. 27

2.13 Schematic of a high-birefringence fiber loop mirror; PC: polarization controller; OSA: optical spectrum analyzer; OC: optical coupler; HBF: high-birefringence fiber. 29

2.14 Typical transmission spectrum of a high-birefringence fiber loop mirror. . . 30

3.1 Experiment setup: an FBG cascaded with a section of MMF for strain and temperature discrimination. 35

3.2 Transmission spectrum shows that the FBG_1 spectrum is superimposed on that of the MMF_1. 39

3.3 Transmission spectrum shows that the FBG_2 spectrum is superimposed on that of the MMF_2. 39

3.4 Transmission spectrum shows that the FBG_1 spectrum is superimposed on that of the MMF_3. 40

3.5 Wavelength shifts as a function of applied strain for FBG_1 combined with MMF_1. . . . 40
3.6 Wavelength shifts as a function of applied strain for FBG_2 combined with MMF_2. . . . 41
3.7 Wavelength shifts as a function of applied strain for FBG_1 combined with MMF_3. . . . 41
3.8 Wavelength shifts as a function of ambient temperature for FBG_1 combined with MMF_1. . . . 42
3.9 Wavelength shifts as a function of ambient temperature for FBG_2 combined with MMF_2. . . . 43
3.10 Wavelength shifts as a function of ambient temperature for FBG_1 combined with MMF_3. . . . 43
3.11 3D plot illustrating simultaneous measurement of strain and temperature by measuring the wavelength shifts of the FBG_1 and MMF_3. . . . 44
3.12 Experiment setup using an intensity-based interrogation method. OC: optical coupler; MMF: multimode fiber; PM: power meter. . . . 45
3.13 Transmission spectra of MMF1 and MMF2. . . . 46
3.14 Transmission spectra of MMF2 with zero strain at different temperatures from 24 °C to 80 °C in the wavelength range of 1530-1590 nm. . . . 48
3.15 Transmission spectra of MMF2 with zero strain at different temperatures from 24 °C to 80 °C in the wavelength range of $1559 - 1562$ nm. . . . 49
3.16 The slopes of MMF2 spectrum at different temperatures. . . . 49
3.17 Power ratio changes, $\Delta(P_1/P_3)$ and $\Delta(P_2/P_3)$, as a function of applied strain. 50
3.18 Power ratio changes, $\Delta(P_1/P_3)$ and $\Delta(P_2/P_3)$, as a function of temperature change. . . . 50

4.1 Experiment setup: An FBG inserted inside a HBFLM. $\times$: the spliced point. 55
4.2 Transmission spectrum of the FBG and HBFLM at zero strain and room temperature (22.3 °C). . . . 57
4.3 Transmission spectrum of the FBG and HBFLM at zero strain and room temperature (40 °C) showing two minima. . . . 58
4.4 Wavelength shifts as a function of applied strain. . . . 59
4.5 Wavelength shifts as a function of ambient temperature. . . . 59

4.6 Sensor output obtained by Eq. (4.4) for the applied strain at a fixed temperature of 58 °C and temperature variations under a constant strain of 350 $\mu\varepsilon$, respectively. 60
4.7 SDM HBFLM sensing structure (inset shows the strain sensing structure). 61
4.8 Transmission spectra of the HBFLM1 at different temperatures under zero strain. 64
4.9 Transmission spectra of the HBFLM2 at different temperatures under zero strain. 64
4.10 Characteristics of HBFLM1 and HBFLM2 transmission spectra versus temperature. 65
4.11 Relationship between the strain and the wavelength of HBFLM1 at different temperatures. 66
4.12 Experiment setup using an intensity-based interrogation method with HBFLM as edge filters. 67
4.13 Transmission spectra of the HBFLMs. 68
4.14 Transmission spectra of HBFLM2 with different applied strains under 23 °C. 70
4.15 Transmission spectra of HBFLM2 under different temperatures with zero strain. 70
4.16 Power ratio change as a function of applied strain. 71
4.17 Power ratio change as a function of temperature change. 71

5.1 Schematic diagram of the experimental setup (Insets show the interferometer structure and the sensing structure, respectively). 77
5.2 Extinction ratio as a function of the intensity ratio I_2/I_1 of the two interference modes. 78
5.3 Transmission power spectra of the BBS and the MMF interferometer with core-offset d about 0, 4, 4.2, and 5 μm, respectively. 78
5.4 Transmission spectrum of the core-offset MMF interferometer sensror. . . . 80
5.5 Measured transmission spectra under different lateral forces. 80
5.6 Extinction ratio responses to different lateral forces. 81
5.7 Measured transmission power spectra under different temperatures at a fixed force of 2.94 N. 82
5.8 Experiment setup and transmission spectrum of the interferometer (Inset shows the transverse sensing structure). 83

5.9 Transmission spectral response to different longitudinal strains at a fixed transverse force of (a) 0 N and (b) 2.94 N. 85
5.10 Relationship between the wavelength and the longitudinal strain under fixed transverse force of (a) 0 N and (b) 2.94 N. 86
5.11 Transmission spectral response to different transverse forces at a fixed longitudinal strain of (a) 0 $\mu\varepsilon$ and (b) 432 $\mu\varepsilon$. 87
5.12 Relationship between the extinction ratio and the transverse strain at a fixed longitudinal strain of (a) 0 $\mu\varepsilon$ and (b) 432 $\mu\varepsilon$. 87
5.13 Transmission spectral response to temperature under transverse force of 2.94 N. 88
5.14 Relationship between the wavelength and temperature under transverse force of 2.94 N. 89
5.15 Measured extinction ratio response to temperature. 89
5.16 Experiment setup. PM: Power meter; OC: Optical coupler. 90
5.17 Spectra of the MMF interferometer and the laser source. 91
5.18 Transmission spectra under different lateral forces. 93
5.19 Power ratio change as a function of applied lateral force. 93
5.20 Schematic diagram of the experiment setup (Inset shows structure of the sensing head). 95
5.21 Interference spectrum of the MMF interferometer. 96
5.22 Wavelength shifts of the interference spectrum at different temperatures. . 97
5.23 Measured relationship between the wavelength and the temperature. 98

6.1 Schematic diagram of the experimental setup. 102
6.2 Coupling between the 7-mm PMPCF and the SMF under different core-offsets. 103
6.3 Coupling between the 11-mm PMPCF and the SMF under different core-offsets. 103
6.4 Measured transmission spectra under different temperatures. 105
6.5 Measured transmission spectra under different applied strains. 106
6.6 Wavelength shift of the transmission minimum at 1544.74 nm against the applied strain. 106
6.7 Measured transmission spectra under different refractive indices. 107

7.1 SEM images of the connector end deposited with SWNTs with different magnifications (a) ×60, (b) ×1 k, (c) ×10 k. (d) Photo of the SA constructed with the connectors. (e) EDFL configuration. 112

7.2 Laser output spectrum of (a) CW mode at a pump power of 9.43 mW and (b) Q-switch mode at a pump power of 11.1 mW. 113

7.3 Typical oscilloscope trace of the typical laser output at a pump power of 29.7 mW. Left inset: single pulse envelope recorded by 100-kHz PD (black line) and 2-GHz PD (red line). Right inset: single pulse envelope recorded by 2-GHz PD with an extra 1-m long unpumped EDF inserted in the laser cavity. 114

7.4 Average output power and pulse repetition rate as a function of pump power at a wavelength of 1554.98 nm. 115

7.5 Laser output spectra at different wavelengths at a pump power of 29.7 mW. 115

7.6 Mode-locked EDFL configuration. EDF: erbium-doped fiber laser; PC: polarization controller; SWNT: single-walled carbon nanotube; OC: optical coupler; ISO: isolator. 118

7.7 Pulse train of the mode-locked fiber laser with anomalous dispersion cavity. 118

7.8 Autocorrelator trace of the optical pulse. 119

7.9 Output spectrum of the mode-locked EDFL with a normal dispersion cavity; the spectral sidebands confirm that the laser is operating in soliton region. 119

7.10 Simulation procedure and schematic diagram of the main components of the laser. SA: saturable absorber. 120

7.11 Result of the simulation of the output temporal intensity profile. 121

7.12 Result of the simulation of the output power spectrum. Inset shows the spectrum in logarithm. 121

7.13 Experiment result of the pulse train with normal dispersion cavity. 122

7.14 Experiment result of the output power spectrum with normal dispersion cavity. 122

7.15 Single pulse envelope recorded by the wide-band oscilloscope. 123

C.1 Multiple beams interference in a Fabry-Pérot interferometer. 131

E.1 Schematic illustration of a high-birefringence fiber loop mirror. 135

Acronyms

ASE	Amplified spontaneous emission
BBS	Broadband source
BDG	Brillouin dynamic grating
BFS	Brillouin frequency shift
BOTDA	Brillouin optical time domain analysis
CCD	Charge-coupled device
CW	Continuous wave
DCF	Dispersion compensation fiber
DSTS	Distributed strain and temperature sensors
EDF	Erbium-doped fiber
EDFL	Erbium-doped fiber laser
ER	Extinction ratio
FBG	Fiber Bragg grating
FC/APC	Fixed connection/angled physical contact
FLM	Fiber loop mirror
FOG	Fiber optic gyroscope
FPI	Fabry-Pérot interferometer
FSR	Free spectral range
FWHM	Full-width at half-maximum
HBF	High-birefringence fiber
HBFLM	High-birefringence fiber loop mirror
ISO	Isolator
LPG	Long-period fiber grating
MMF	Multimode fiber
MZI	Mach-Zehnder interferometer
NA	Numerical aperture
NLSE	Nonlinear Schrödinger equation
OC	Optical coupler
OFSI	Optical fiber Sagnac interferometer
OS	Optical switch
OSA	Optical spectrum analyzer
PC	Polarization controller
PD	Photodector
PM	Power meter
PMF	Polarization-maintaining fiber
PMPCF	Polarization-maintaining photonic crystal fiber
P-OTDR	Polarization-optical time domain refrectometry
RI	Refractive index

SA	Saturable absorber
SBS	Stimulated Brillouin scattering
SCDCF	Small-core dispersion compensation fiber
SDM	Space division multiplexing
SEM	Scanning electron microscope
SMF	Single-mode fiber
SWNT	Single-walled carbon nanotube
TFBG	Tilted fiber Bragg grating
UCB	Uniform cantilever beam
WDM	Wavelength division multiplexing

Chapter 1

Introduction

Ever since ancient times, one of the most important needs of people has been to communicate, which created interest in designing and developing communication system for sending messages from one distant place to another. In 1966, Dr. K. C. Kao and his colleagues in Standard Telecommunication Laboratories Ltd. first introduced the concept of guiding light with optical fibers [1]. Later, since the inception of optical fiber communications, optical fibers, which are glass or plastic cylindrical waveguides that carry light along their length, are irreplaceable in any communication system all over the world. In addition, over the past 30 years, another industry, optoelectronics industry has led to the emergence of many new product areas, including compact disc players, personal copiers, and laser printers, etc., due to both the quality improvements and cost reductions in optoelectronic components [2].

In parallel with these developments, optical fiber sensors, which have been a major user of the technology associated with the optoelectronics and fiber optic communications industries, have fascinated the researchers and tantalized the application engineers for over forty years. There is no doubt that this technology can bring a wealth of applications, ranging from sensors in the medical industry for monitoring important biological functions, the aerospace and wind-energy industries for monitoring the health of the massive structures, through to vast distributed sensors in oil industry. Many components associated with optical fiber communications and optoelectronics industries are developed for optical fiber sensor applications nowadays. The capability of optical fiber sensors to displace traditional sensors for sensing applications has been enhanced, since component prices have fallen and the component quality has been improved greatly.

1.1 Applications of Optical Fiber Sensors

Following the fast development of the optical fiber sensor technology in recent years, many kinds of optical fiber sensors have been designed and developed to measure various parameters. To date, more than 70 different parameters could be measured or monitored by optical fiber sensors, such as rotation, acceleration, electric and magnetic fields, temperature, pressure, acoustics, vibration, strain, humidity, viscosity, refractive index, etc. Optical fiber sensors have become more and more important, and in many industries, they gradually become indispensable, such as in civil, medical and military applications.

1.1.1 Civil Applications

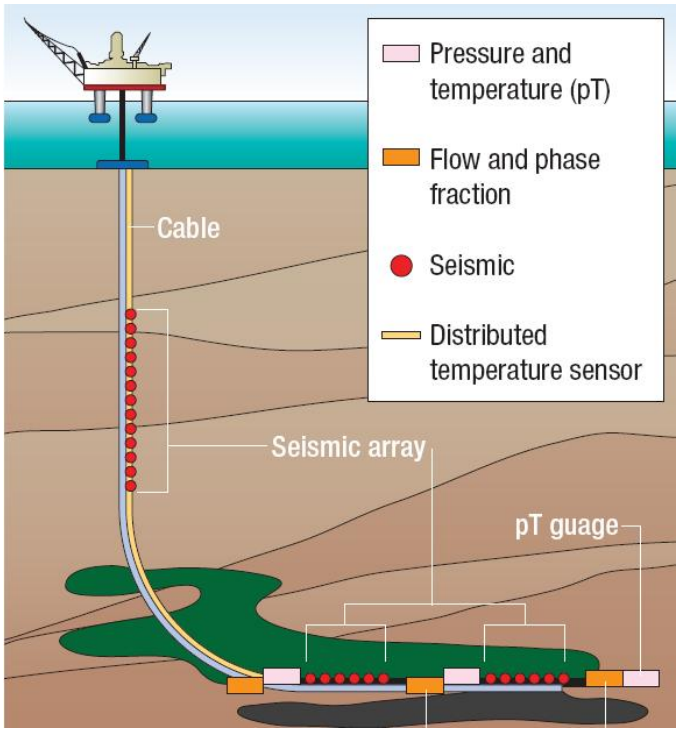

Figure 1.1: Oil and gas reservoirs are drained using several wells from one topside facility. The well heads can be located several kilometers from the platform below the sea. Based on data provided by distributed flow sensors and pT gauges, the production from each well and each zone within a well is controlled using downhole control valves. Reprinted by permission from Macmillan Publishers Ltd: Nature Photonics, 2:147-149, copyright 2008.

First of all, optical fiber sensors have become very important tools in the oil and gas industry, helping engineers not only locate and monitor the wells, but also extract

the largest possible percentage of oil and gas out of them. Within oil or gas wells, the environmental conditions are challenging with temperature over 100 °C and sometimes even as high as 200 °C. The reliability of conventional electrical sensors decreases under such harsh environment, and the electrical sensors may even increase the possibility of explosion inside the oil or gas wells. The reason that optical fiber sensors could offer high reliability for in-well applications is their passive nature. Today, most of the optical fiber sensors available to the oil and gas industry are intrinsic, that is, the sensing element is the fiber itself and the light does not have to exit and re-enter the fiber core. Hence, after the first optical fiber sensor based on fiber coupled micro-machined silicon resonators was installed in an oil well in 1993 for temperature and pressure measurement [3], many pressure, temperature, flow and seismic sensors have been installed in reservoirs permanently over the past 20 years. Such optical fiber sensors are widely used to map reservoirs, image and characterize the geophysical properties of rock formations, and to monitor the processes separating oil, gas and water.

Figure 1.2: The Airbus A380, the largest passenger aircraft in the world, uses composites extensively. Airbus is actively investigating the use of fibre-optic sensors on the A380. Reprinted by permission from Macmillan Publishers Ltd: Nature Photonics, 2:153-154, copyright 2008.

Secondly, optical fiber sensors could also find applications to check pipeline integrity, to detect pipeline buckling [4], to detect wall-thinning defects [5, 6, 7], or pipeline leaks [8]. Pipelines provide one of the safest and most reliable approaches for transportation of gases and liquids; however pipeline failures would cost millions dollars loss and may have a severe effect on surrounding environment. Hence, monitoring the integrity and health of the pipelines is very important for pipeline industries all over the world. For example, Italy researchers have shown that optical fiber sensors can be used to monitor the structural integrity of a pipeline, and the deformations of the rock or soil surrounding the pipeline [9]. They could measure the amount of pipeline dislocation and its direction by measuring normal strain using stimulated Brillouin scattering along three longitudinal

directions running down the pipeline. Another research group in Canada has used a distributed fiber sensor to detect localized pipe-wall buckling in an energy pipe by measuring the longitudinal and hoop strain distributions along the outer surface of the pipe [4]. They also have used the similar technique to identify several inner wall cutouts in an end-capped steel pipe by measuring the axial and hoop strain distributions along the outer surface of the pipe [5]. Since the spatial resolution has already been achieved in centimeter range along tens of kilometer measurement range [10, 11, 12, 13], these technologies have already penetrated into the market, and many distributed sensor systems have already been commercialized, such as OZ Optics Ltd.'s Foresight^{TM} series of fiber optic distributed strain and temperature sensors (DSTS). They are expected to play a very important role in the pipeline industries to save money for inspection and maintenance.

Figure 1.3: Optical sensors are being used to monitor the structural health of large composite structures such as turbine blades. Reprinted by permission from Macmillan Publishers Ltd: Nature Photonics, 2:143, copyright 2008.

Thirdly, the health of some massive structures, such as aircrafts, wind-turbine blades, bridges, dams, etc., needs to be monitored in a continuous manner to avoid some disaster accidents. For example, researchers in Germany have tested optical fiber sensors based on Bragg gratings in the tail of the new Airbus A340/600, and Airbus is actively investigating the use of optical fiber sensors on the A380 [14]. Embedded into the structure of the aircraft, optical fiber sensors which could measure strain offer the aerospace industry with the opportunity to schedule inspection, service and retirement of the aircraft based on the actual loads experienced by the structure. Another example where optical fiber sensors are playing a valuable role is wind-turbine blade, since the wind turbines become larger

and larger which might bring many new engineering challenges. Optical fiber sensors could provide an understanding of real-time loads and blade history that is very important to both the manufacturers and wind-farm owners.

Moreover, optical fiber sensors could also find many other civil applications, such as analyzing the impact of traffic on concrete slabs [15], detecting hydrogen leaks [16], intrusion [17, 18], vibration [19, 20, 21], etc.

1.1.2 Medical Applications

Optical fiber sensors have a potential that they could be made with a miniature size, which would help them be used in many medical applications, especially in the development of minimally invasive surgical tools. Although the penetration into the medical market is

Figure 1.4: Thanks to their miniature size, optical-fibre sensors have real potential in many medical applications, especially in the development of minimally invasive surgical tools. Reprinted by permission from Macmillan Publishers Ltd: Nature Photonics, 2:150-152, copyright 2008.

slow because of high cost, an increasing number of medical procedures are benefiting from the advantages that these tiny sensors can bring. An example of a medical application is a miniature pressure sensor, which can be used in neurology for intracranial pressure monitoring [22]. In addition, such optical fiber sensors which could measure strain and

temperature can be positioned at the tip of instrumented catheters to give useful feedback in surgical procedures.

Although most high-volume medical applications for optical fiber sensors involve measuring physical parameters, chemical sensing is also a growing market. For example, optical fiber sensors that could detect dissolved oxygen and carbon dioxide or pH are now commercially available. Moreover, since optical fiber sensors are immune to electromagnetic interference, they are perfectly suitable for applications involving high electromagnetic field, such as in magnetic resonance-imaging systems.

On the other hand, optical fiber biosensors are very attractive in medical applications, by measuring absorbance, reflectance, fluorescence, etc., to sense a biological species of interest [23]. For example, the simplest optical biosensors use absorbance measurements to determine any changes in the concentration of analytes that absorb a given wavelength of light. A fiber optic pH sensor [24] and a fiber optic oxygen sensor [25] have been developed for use in medical applications. In addition, Piunno *et al.* [26, 27] reported one of the first biosensors for direct analysis of DNA hybridization by use of an optical fiber, and researchers in Virginia Institute and State University developed a microgap fiber multicavity Fabry-Pérot sensor for biosensing [28].

1.1.3 Military Applications

Optical fiber sensors, which could provide rotational rate information precisely, have attracted intensive research interests over more than 30 years. This kind of sensor has been well-known as fiber optic gyroscope (FOG) [29]. The physical principle that explains the operation of an FOG is known as Sagnac effect [30]. The FOG has been used for automobile navigation as a heading sensor in Nissan's luxury sedans since 1995 [31]. Commercial aircraft attitude heading reference system is one of the earliest medium-performance FOGs [32, 33]. Nowadays, they provide the dominant solution in many applications, such as navigation, guidance, control, and stabilization of missiles, aircrafts, automobiles, attitude heading and reference systems, robotics, satellites, etc.

Optical fiber hydrophone, which is an acoustic sensor using optical fiber as the sensing element, is another kind of sensor which could be developed for military applications. The development of optical fiber hydrophone started in the late 1970s [34, 35]. The United States developed their fiber optic hydrophones used in the Navy ships for underwater exploration since 1990. The fiber optic hydrophones could also realize critical infrastructure protection and littoral security missions demand by providing solutions for shallow water antisubmarine warfare, harbor security and perimeter security applications. Besides the military applications, optical fiber hydrophones could also be used for geophysical applications, such as seismic exploration for oil reservoirs.

1.2 Advantages of Optical Fiber Sensors

The advantages of optical fiber sensors are well known and have been widely extolled in the research literature on the subject. The conventional electro-mechanical sensor systems have been well established for a long time, and they have been proven to have reliability records and reasonable manufacturing costs; therefore, fiber-based sensor systems have to exhibit superior advantages in order to penetrate into the market to replace the existing conventional sensors. The advantages which keep optical fiber sensors survival include electromagnetic interference immunity, high sensitivity, lightweight, small size, environmental ruggedness, multiplexing and distributed capacities, etc.

1.2.1 Electromagnetic Interference Immunity

The optical fiber itself is usually made of glass or plastic material. Since most of fiber sensing heads are the pure fiber with no electric circuits, the external electromagnetic disturbance would not influence the way the light propagating inside optical fibers. In other words, because the sensing information is carried by photons not electrons, optical fiber sensors are intrinsically insensitive to electromagnetic interference. This feature offers an superior advantage of the optical fiber sensors compared to their electronic counterparts. For example, electrical, radiofrequency or microwave instruments can generate electromagnetic interference in the medical operating environment. Optical fiber sensors working in this environment could be made much smaller than the electrical sensors, since they do not need to be shielded. The miniature size is probably one of the most important concerns in the space-constrained and instrument-crowded medical environment.

1.2.2 High Sensitivity

Another advantage of optical fiber sensors is that they have high sensitivity. Since by measuring the change of the light signal, such as the wavelength, phase, intensity, etc., it is easy to achieve high sensitivity with optical fiber sensors. Usually, a small perturbation of the surrounding environment would affect the physical properties of the optical fiber, such as its refractive index, length, configuration, etc., then, these changes in turn, would affect the condition under which the light propagates in fibers. Only a small variation of the surrounding environment would result in a large change of the light signal by properly designing the sensing head.

1.2.3 Lightweight, Small Size, Environmental Ruggedness

Optical fibers have the diameters on the order of millimeters, and are very lightweight. This offers optical fiber sensors an advantage that they could be easily embedded into the structures which need to be monitored. On the other hand, the glass is in general a very stable material, so that optical fiber sensors could survive for the applications in the harsh environment. For example, in oil well, the humility and high temperature condition would not allow the long-time operation of the electrical devices. In addition, the optical fiber sensor is passive in nature, which is much safer when long-time monitoring is needed in the oil well, where electrical devices might result in a disaster explosion. For under water application, optical fiber sensors are the best choices because of their stability in nature, and do not need other sophisticated water-proof systems to shield the sensing head.

1.2.4 Multiplexing and Distributed Capacities

Optical fiber sensors have already appeared to have a distinct edge over the competition with the conventional sensors, which attributes to their multiplexing and distributed capacities. An interesting application for health monitoring of the massive structures, such as the dams, wind turbines, bridges, pipelines, etc., needs the sensors to have the ability to continuously monitor the structures over long distance. In addition, the sensors need to tell the location over which a strain has been accumulated or the position that has been deformed. Optical fiber sensors are a good candidate for such applications. One solution is to cascade point sensors to form a mesh, and then embed this point sensor web to the structures to achieve the quasi-distributed sensing. An alternative solution is to use light scattering (e.g., Brillouin scattering, Rayleigh scattering, etc.) in an optical fiber to realize such applications. The main advantage of such distributed sensors is that they have simple sensing head (i.e., one long length fiber could act as the sensing head), and they could achieve fully distributed sensing for the case that the positions which need to be monitored are not known. To date, the spatial resolution of such sensors has been achieved down to centimeter range, and the measurement range could be achieved up to tens of kilometers which is sufficient for most of the applications.

1.3 Classifications of Optical Fiber Sensors

To date, a huge amount of optical fiber sensors have been successfully developed and find their way toward the "real-world" applications. Basically, optical fiber sensors consist of four major components: optical source, signal waveguide (e.g., optical fiber), sensing head, and detector (see Fig. 1.5). Light propagates along an optical fiber passing through the

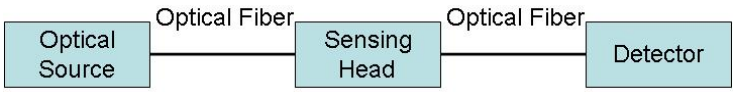

Figure 1.5: Basic optical fiber sensor configuration consisting of optical source, optical fiber, sensing head, and detector.

sensing head, where certain properties of the light wave would be modulated when the sensing head is influenced by the external variations which need to be monitored. The modulated light wave (containing the information) is then received by the detector, and after the demodulation, the external varying parameters which need to be measured could be obtained.

In general, optical fiber sensors are loosely grouped into two basic categories referred to as extrinsic and intrinsic sensors. For extrinsic sensors, sensing takes place in a region outside the fiber. Fig. 1.6 shows the case of an extrinsic optical fiber sensor. The optical fiber leads up to a so-called "black box" which impresses information which needs to be monitored onto the light beam in response to environmental effects. An optical fiber then

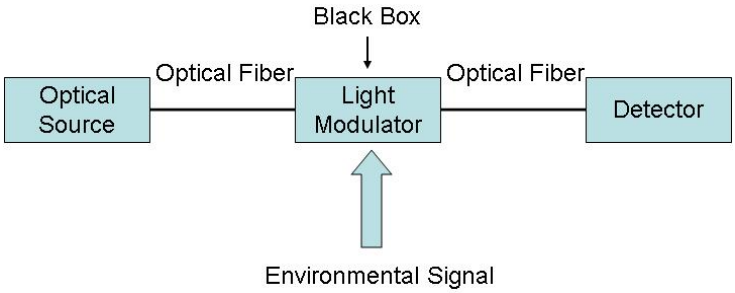

Figure 1.6: Extrinsic optical fiber sensors consisting of optical fiber that leads up to and out of a "black box" that modulated the light beam passing through it under environment change.

guides the light with the information impressed by the surrounding environment back to detector [2]. Note that the "black box" usually contains other electrical or optical devices; hence, the extrinsic sensors also refer to as hybrid optical fiber sensors.

For intrinsic sensors, one or more of the physical properties of the fiber undergo a change under environment variation. In other words, the intrinsic optical fiber sensor uses an optical fiber to carry the light beam, and the environmental effect impresses information onto the light beam while it is in the optical fiber. The illustration is shown in Fig. 1.7. The intrinsic optical fiber sensors could also refer to as all-fiber sensors.

However, there are many other classification methods for optical fiber sensors in order

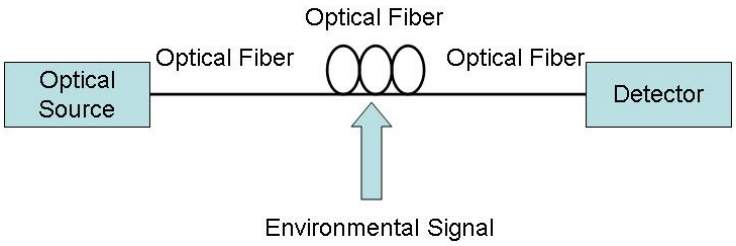

Figure 1.7: Intrinsic optical fiber sensors rely on the light beam propagating through the optical fiber modulated by the environmental effect directly.

to be convenient to users, researchers, or engineers. Since there are a variety of kinds of optical fiber sensors, it is hard to make a very comprehensive illustrations. The following subsections only introduce some basic categorizations.

1.3.1 According to Application

According to different parameters the sensor could measure, or according to different applications, optical fiber sensors could be categorized as temperature sensors, strain sensors, displacement sensors, current sensors, pressure sensors, vibration sensors, chemical sensors, etc. This is a straightforward method to categorize fiber sensors. The users could find the optical fiber sensors easily to meet their requirements. For most of the optical fiber sensor manufactures, they advertise their sensor products according to applications in order to become "user-friendly".

1.3.2 According to Measurable Spatial Scope

Optical fiber sensors could also be categorized as point sensors, quasi-distributed sensors, and fully distributed sensors. One advantage of optical fiber sensors is that they could be made with a small size, and these point sensors could be used to measure the parameters of certain points in the space. For example, in medical application, temperature and pressure inside certain tissues are important information which needs to be monitored during the surgery. Thanks to the miniature size of optical fiber sensors, they become more and more important in such applications. Many optical fiber components could serve as point sensing head, such as fiber Bragg gratings (FBGs) [36], optical fiber Fabry-Pérot interferometers [37], multimode fiber interferometers [38], etc.

Quasi-distributed sensors are able to measure the parameters of many separate points in the space simultaneously, by multiplexing the point sensors to form a sensing mesh. For instance, if people are interested in certain points on some massive structures, or only

some positions need to be monitored, by space division multiplexing FBGs, and placing the FBGs on these positions, all the changes on these points could be monitored simultaneously. This could be achieved because the sensing information is encoded directly into wavelength, which is an absolute parameter. Many quasi-distributed sensing applications with FBG arrays have already been reported, but with different demodulation technique, such as using Fabry-Pérot filters [39, 40], acousto-optic filters [41], and FBG-based filters [42], etc.

However, for monitoring the health of some massive structures, the locations which need to be monitored are usually not known. This requires the sensors to have the ability for fully distributed sensing, by embedding the sensing fiber into the structure. Although point sensors could realize quasi-distributed sensing, their localized nature only gives incomplete information about the structure health. Hence, there is a need for a technique that detects faults and assesses the severity of damage of the whole structure. Such a sensor must perform fully distributed temperature and strain measurements over several meters to tens of kilometers. Fully distributed fiber sensors, which are based on Rayleigh scattering [43], Raman scattering [44], and Brillouin scattering [45], could realize this purpose. For example, the technique based on Brillouin scattering called Brillouin Optical Time Domain Analysis (BOTDA) shows very good feature to realize health monitoring of the massive structures, and has already been commercialized.

1.3.3 According to Modulation Process

Light wave propagating along optical fiber could be characterized in terms of four factors, which are intensity, phase, state of polarization, and wavelength (frequency). When the surrounding environment has certain perturbation on the sensing head, at least one of the four factors change according to the influence. By measuring the light signal variation, one could obtain the useful information of the surrounding environment change. Therefore, optical fiber sensors could be categorized according to the modulation process as intensity modulation sensors, phase modulation sensors, polarization modulation sensors, as well as wavelength modulation sensors.

1.3.4 According to Technology

Another easy way to categorize optical fiber sensors is according to different technologies, such as fiber grating sensors, fiber Fabry-Pérot interferometer sensors [37], high-birefringence fiber loop mirror sensors [46], polarization-optical time domain refrectometry (P-OTDR) sensors [17, 18], BOTDA sensors [15, 45], etc. Since there are so many technologies nowadays which could find perfect applications as optical fiber sensors, it is hard to list them all. However, most of these technologies are well-known, so that only the technologies which are closely related to this thesis will be presented in the next chapter.

1.4 Thesis Content Summary

Chapter 1 is the introduction which gives an overview of the optical fiber sensors, including the applications, the advantages, and the classifications.

In Chapter 2, some basic optical fiber sensor technologies are reviewed. Only the technologies which are directly related the content of this thesis are discussed, such as fiber grating sensors, multimode fiber sensors, high-birefringence fiber loop mirror sensors, and the interrogation methods for FBG sensors. Since optical fiber sensors are usually sensitive to several parameters simultaneously (e.g., temperature and strain), it is necessary to develop method and scheme for multi-parameter discrimination. The method will be introduced at the end of this chapter.

Chapter 3 discusses the detail experiments based on FBGs and multimode fibers achieving temperature and strain discrimination. Two schemes are introduced. The first one is using an FBG cascaded with a section of multimode fiber. By measuring a pair of wavelength shifts from the FBG and the multimode fiber interferometer with an optical spectrum analyzer, simultaneous measurement of strain and temperature could be achieved. The performance is improved with an alternative scheme where multimode fiber interferometers are used as edge filters. By measuring a pair of power ratio changes instead of the wavelength shifts, optical spectrum analyzers are not needed; therefore, the sensing scheme is more cost-effective and has a higher operation speed.

Simultaneous measurement of strain and temperature with FBGs and high-birefringence fiber loop mirrors (HBFLMs) are illustrated in Chapter 4. Three configurations are presented. The first one is to insert an FBG into an HBFLM. The second scheme is to space division multiplex two HBFLMs as a sensing head. By measuring a pair of wavelength shifts from the FBG and the HBFLM (the first scheme), or sequentially from two HBFLMs (the second scheme) with an optical spectrum analyzer, simultaneous measurement of strain and temperature could be achieved. The performance is improved with the third scheme, where HBFLMs are used as edge filters. By measuring a pair of power ratio changes instead of the wavelength shifts, optical spectrum analyzers are not needed.

In Chapter 5, a small core diameter multimode fiber based interferometer is proposed, and its application in optical fiber sensors to measure temperature, lateral force (lateral strain), longitudinal strain is discussed in detail. Four configurations are introduced. A simple lateral force sensor is introduced first by measuring the extinction ratio change of the interference spectrum. Then, we extend this sensing head to the simultaneous measurement of lateral and longitudinal strain by monitoring the extinction ratio variation and the spectrum shifts at the same time. The third scheme is to adopt the intensity-based interrogation method for lateral force measurement without using an optical spectrum analyzer. Finally, a high-temperature sensor with only 4-mm long sensing head is presented. The measurement range could be achieved up to 600 °C with a high sensitivity.

Chapter 6 presents a compact fiber sensor using a polarization-maintaining photonic crystal fiber (PMPCF) to measure strain and refractive index. By slightly offsetting the single-mode fiber core with respect to that of the PMPCF, interference spectrum could be generated due to the coupling between the cladding and core modes. A 7-mm long sensing head could be achieved for strain and refractive index measurement. The most interesting feature of this kind of sensor is its temperature-insensitive property.

In the last chapter, Chapter 7, several schemes of passively Q-switched and mode-locked erbium doped fiber lasers using single-walled carbon nanotubes as saturable absorbers are presented. Although at a glance, the topic on optical fiber lasers is very different from that on the optical fiber sensors, fiber lasers have the potential to be used as the sources for the sensors. For instance, for distributed sensing, pulsed lasers are usually used as the source. Since optical fiber lasers are very compatible with the fiber sensors, pulsed fiber lasers would be a good choice. In addition, when study short pulse fiber lasers, many nonlinear effects need be considered, and these effects also exist in designing high-performance long distance distributed fiber sensor; therefore, this would, in turn, help to develop better sensor systems. Finally, some future topics on fully distributed fiber sensors will be discussed. All the work presented in Chapters 1-6 are focusing on point sensors. However, fully distributed fiber sensors is an important branch of optical fiber sensor family. A short review and the existing problems will be discussed; then the feasible solutions will be presented for the future work.

Chapter 2

Basic Optical Fiber Sensor Technologies: Fiber Grating Sensors, Fiber Interferometer Sensors, and Measurands Discrimination

2.1 Fiber Grating Sensors

Fiber gratings are simple, intrinsic sensing elements which can be photo-inscribed into a silica fiber. They have all the advantages normally attributed to optical fiber sensors. In more detail, a periodic structure is written into the core of an optical fiber and this periodic structure will reflect specific optical wavelength, which is dependent on the periodicity. Vary the periodicity, vary the wavelength. Since this period depends upon environmental temperature and externally applied strains and pressures, we have the basis for a simple sensor (e.g., a fiber grating) which could be easily interrogated. In this section, the detailed fabrication of the fiber grating will not be discussed, and interested readers could find more details about this topic in Ref. [1, 2, 3, 4, 5, 6, 7]. Instead, the classifications of the fiber gratings, the sensing principle as well as the interrogation methods will be introduced in detail.

2.1.1 Classifications of Fiber Gratings

There are many different kinds of fiber gratings nowadays, and in general they could be considered as two main categories, uniform and nonuniform gratings.

I. Uniform Gratings

Uniform gratings refer to the periodicity of the grating is uniform along the axis of the fiber core and the modulation depth of the refractive index is constant. Considering the length of the grating pitch and the direction of the refractive index variation, usually there are three kinds of uniform gratings: fiber Bragg gratings (FBGs), long-period fiber gratings (LPGs), and tilted fiber Bragg gratings (TFBGs).

a) Fiber Bragg Gratings

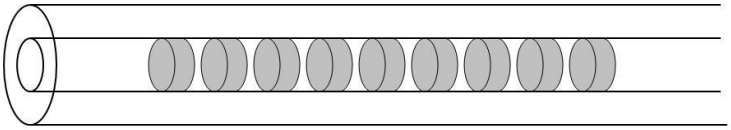

Figure 2.1: Fiber Bragg grating: the variation of the refractive index in the fiber core is uniform along the axis; the modulation depth of the refractive index is constant.

The periodicity of the FBG is usually on the order of 100 nm, and the modulation depth of the refractive index is about $10^{-5} - 10^{-3}$. The variation of the refractive index is along the direction of fiber core axis, shown in Fig. 2.1. The operation principle could be considered as a one-dimensional photonic crystal, which has a forbidden band where electromagnetic wave with certain wavelength cannot exist. The wavelength bandwidth depends on several parameters, particularly on the grating length, but typically is around 0.05 nm to 0.3 nm for most sensor applications. Besides serving as an optical fiber sensor element, FBGs could also find applications in optical communications, such as wavelength division multiplexing, add-drop multiplexers [8], etc. Detailed principles of FBGs are discussed in the next subsection.

b) Long-Period Fiber Gratings

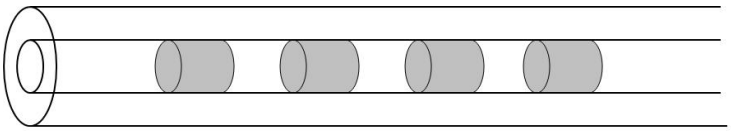

Figure 2.2: Long-period fiber grating: the variation of the refractive index in the fiber core is uniform and along the axis; the modulation depth of the refractive index is constant; the periodicity is much longer than that of an FBG.

LPGs, which were first introduced in 1995 by Vengsarkar *et al.* [9], are different from FBGs in terms of the length of the periodicity. A typical LPG has a period of about

hundreds of micrometers (see Fig. 2.2), a length of about $1-3$ cm, and index modulation depth of 10^{-4} or greater [10]. Since the period is much longer than the operation wavelength in the communication band, LPGs are not the reflection-type devices compared to FBGs. The principle could be understood as that the LPG couples light out of the core and into the cladding at specific wavelengths, depending on the grating pitch and refractive indices. The light in the cladding quickly decays due to losses at the cladding/air interface, leaving a series of loss bands or resonances in the guided mode; therefore, LPGs are transmission-type devices. LPGs were initially developed for the use as band-rejection filters [11], and have been used for gain-flattening of erbium-doped fiber amplifiers [12]. Moreover, LPGs also present unique opportunities as optical fiber sensors not long after their first development. The resonance wavelength of the LPG depends on the index difference between the core and the cladding, and hence any variation caused by strain, temperature, or changes in the external refractive index can cause large wavelength shifts in the resonances [13, 14, 15].

c) Tilted Fiber Bragg Gratings

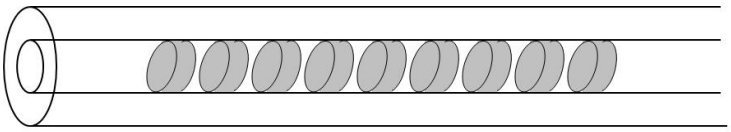

Figure 2.3: Tilted fiber Bragg grating: the variation direction of the refractive index has an angel to the axis of the fiber core.

TFBGs have similar period length as that of the FBGs. However, the main difference compared to LPGs and FBGs is that the variation direction of the refractive index has an angle to the axis of the fiber core, shown in Fig. 2.3. The typical transmission spectrum of the TFBG shows multiple resonances. The main dip corresponds to the so-called Bragg resonance which results from the coupling between the co- and counter-propagating core modes. The other resonances are due to the coupling between the core mode and counter-propagating cladding modes of the fiber, since the tilted grating results in part of the light reflected into the cladding. These cladding modes attenuate rapidly along the propagation due to the loss in the cladding. Therefore these peaks are observable in the transmission spectrum, but not in reflection. TFBGs could find applications in optical fiber sensors to measure temperature, strain, bending, refractive index, vibration, etc. [16, 17, 18, 19].

II. Nonuniform Gratings

Nonuniform gratings refer to the periodicity of the grating is nonuniform along the axis of the fiber core and the modulation depth of the refractive index does not need to be constant.

Usually there are many kinds of nonuniform gratings, such as chirped fiber Bragg gratings, superimposed multiple fiber Bragg gratings, and superstructure fiber Bragg gratings.

a) Chirped Fiber Bragg Gratings

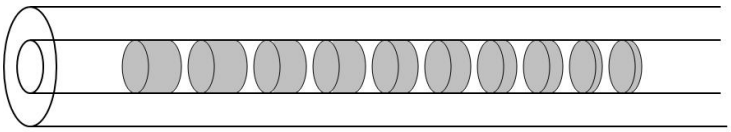

Figure 2.4: Chirped fiber Bragg grating: the variation of the refractive index in the fiber core is nonuniform and has a linear decreasing variation of the grating period.

Chirped fiber Bragg gratings were originally designed for dispersion compensation in high bit-rate telecommunication systems [20]. A chirp is achieved simply by varying the grating period, the average index, or both along the length of the grating (see Fig. 2.4 for example). One method for making chirped gratings is to taper a fiber in the region of the grating [21]. The decreasing core size decreases the effective refractive index along the length of the taper, resulting in a chirp. Another method involves bonding an unchirped grating to a substrate with a "soft glue" that allows a strain gradient to be formed along the grating length through the differential shear strength of the glue [22]. Chirped fiber Bragg gratings behave uniquely in the presence of strain and temperature fields. In principle, such devices could be used to measure strain and temperature simultaneously by carefully calibrating and measuring the grating spectrum shift and broadening simultaneously [23].

b) Superimposed Multiple Fiber Bragg Gratings

Superimposed multiple fiber Bragg gratings refer to several Bragg gratings inscribed at the same location on an optical fiber [24]. This is of interest as a device in fiber communications, lasers and sensor systems, because multiple Bragg gratings at the same location basically perform a comb function and this device is ideally suitable for multiplexing and demultiplexing signals. After superimposing several Bragg gratings on an optical fiber at the same location, the individual grating reflectivity would be reduced, and the Bragg wavelength changes as well due to the variation of the effective refractive index. Although the reflectivity of the individual grating is less that 70% after 7 gratings are superimposed [24], all the gratings at the same location offer new opportunities in optical integrated technology, where the issue of size is always a concern.

c) Superstructure Fiber Bragg Grainings

A superstructure fiber Bragg grating refers to a grating fiber structure fabricated with a modulated exposure over the length of the gratings [25]. Therefore, the Bragg grating superstructure has a periodically varying envelope of the refractive index modulation. The reflection spectrum of such superstructure gratings shows a series of regularly spaced peaks,

providing extra degrees of freedom which can be exploited in the design of grating based devices. These superstructure gratings can be used as comb filters for signal processing, and for increasing the tunability of the fiber laser-grating reflector.

For different applications, there are many other kinds of gratings, such as writing gratings in multimode fibers, birefringent fibers [26], in the splice point of two different fibers [27, 28], etc. It is hard to list all the fiber gratings; however, the principles of different kinds of gratings are similar. In Section 2.1.2, the basic principle of the FBG is introduced, so that the principles of other different kinds of fiber gratings could be understood.

2.1.2 Principle of Fiber Bragg Grating Sensor

In this thesis, only FBGs are used in the experiments. The principle of the FBG and its applications in optical fiber sensors are introduced. Other kinds of the fiber gratings have similar principles, which could be easily understood based on the context of this section.

The basic operation principle of an FBG sensor system is to monitor the shift in wavelength of the reflected Bragg signal with the changes in the measurand. The Bragg wavelength λ_B, or resonance condition of a grating, is expressed as:

$$\lambda_B = 2n_{eff}\Lambda, \tag{2.1}$$

where Λ is the grating periodicity and n_{eff} is the effective refractive index of the fiber core. When such a device is illuminated by a broadband light source, a narrowband spectral component at the Bragg wavelength is reflected by the grating. This spectral component is missing in the transmitted light. The bandwidth of the reflected signal depends on several parameters, particularly on the grating length, but typically is around $0.05 - 0.3$ nm in most sensor applications. Perturbation (e.g., external strain or temperature variation) of the grating results in a shift in the Bragg wavelength of the grating which can be detected in either the reflected or transmitted spectrum.

Most of the work on FBG sensors has been focusing on the use of these devices for providing point sensing of strain or temperature. The temperature response arises due to the inherent thermal expansion of the fiber material and the temperature dependence of the refractive index. The strain response arises due to both the elongation of the sensor (or corresponding fractional change in grating periodicity), and the change in the refractive index of the fiber due to photoelastic effects. The shift of the Bragg wavelength with strain and temperature can be expressed as (Appendix A)

$$\frac{\Delta\lambda_B}{\lambda_B} = \left\{1 - (\frac{n_{eff}^2}{2})\left[p_{12} - \nu(p_{11} + p_{12})\right]\right\}\varepsilon + (\alpha + \frac{1}{n_{eff}}\frac{\partial n_{eff}}{\partial T})\Delta T, \tag{2.2}$$

where ε is the applied strain; ΔT is the temperature change; the coefficients, p_{ij}, are the Pockel's coefficients of the strain-optic tensor; ν is Poisson's ratio; and α is the coefficient of thermal expansion of the fiber material (e.g., silica). The factor $(n_{eff}^2/2)[p_{12} - \nu(p_{11} + p_{12})]$ has a numerical value of around 0.22. The measured strain response at constant temperature is found to be [10]

$$\frac{1}{\lambda_B}\frac{\delta\lambda_B}{\delta\varepsilon} = 0.78 \times 10^{-6}\mu\varepsilon^{-1}. \tag{2.3}$$

As a rule of thumb, this responsivity gives the measurement of the Bragg wavelength shift with strain of 1 nm per 1000 $\mu\varepsilon$ (micro-strain) at 1300 nm (e.g., one micro-strain equals to one meter long fiber elongated by one micrometer). In silica fibers, the temperature response is dominated by the term of $\partial n_{eff}/\partial T$, which accounts for almost 95% of the observed wavelength shift. The normalized thermal responsivity at constant strain is

$$\frac{1}{\lambda_B}\frac{\delta\lambda_B}{\delta T} = 6.67 \times 10^{-6\text{o}}\text{C}^{-1}. \tag{2.4}$$

A wavelength resolution of ~ 1 pm is required to resolve a temperature change of ~ 0.1 $^{\text{o}}$C, or a strain change of 1 $\mu\varepsilon$ [10]. Although this wavelength resolution could be achieved using laboratory instrumentation such as optical spectrum analyzers and tunable lasers, the capability to resolve changes on this order using compact, packaged electro-optics devices is not easy. This has been the focus of a large amount of research work in the grating sensor field for demodulation of wavelength signal. There are many interrogation methods developed, which will be introduced in Section 2.1.3.

Since the sensing information of the FBG is encoded directly into the wavelength, which is an absolute parameter, the output does not depend directly on the total light intensities, powers, losses in the connecting fibers and couplers, or source power. This is widely acknowledged as one of key advantages of FBG sensors. The wavelength encoded nature of the output also enables wavelength division multiplexing by allowing each FBG sensor to be assigned to a different slice of the available source spectrum.

2.1.3 Fiber Bragg Grating Sensor Interrogation

Interrogators or demodulators in fiber grating sensor systems are the measurand-reading units that extract measurand information from the light signals coming from the sensing heads. As mentioned, the measurand is encoded spectrally for FBG sensors, and hence the interrogators are usually meant to measure the Bragg wavelength shifts and convert the results to measurand data. In the laboratory, when one is designing and developing fiber grating sensors, optical spectrum analyzers are usually used in monitoring grating

reflection or transmission spectra. However, optical spectrum analyzers are not practical for "real-world" applications in the sensor systems, not only because of their high prices but also due to their slow scanning speed which limits dynamic sensing.

To date, many interrogators have already been developed with both passive and active detection schemes. In this section, several interrogation methods are reviewed.

I. Passive Detection Schemes

Passive detection scheme interrogators refer to those that do not use any electrical, mechanical, or optical active devices. The simplest way to think about measuring the wavelength shift of light reflected from an FBG without monitoring the spectrum is to use a linearly wavelength-dependent optical filter. By monitoring the reflected light power change instead of monitoring the spectrum shift, optical spectrum analyzers would be replaced in the sensor system. Indeed, this method was one of the first proposed methods for the practical wavelength change interrogation system of FBG sensors. Fig. 2.5 shows the concept

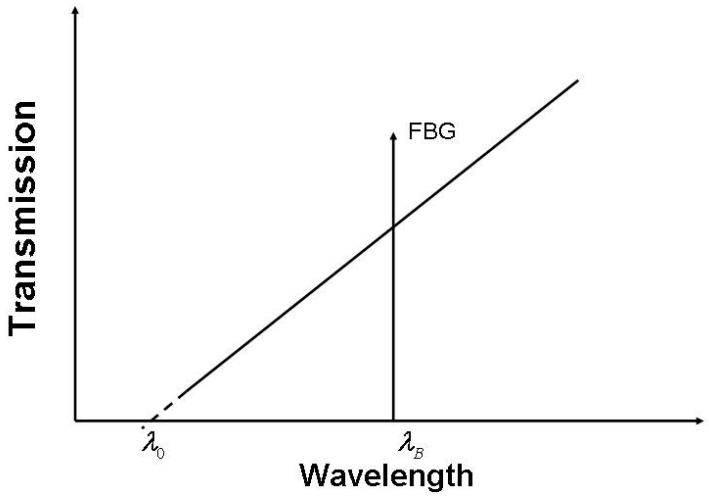

Figure 2.5: Transmission of a linearly wavelength-dependent optical filter (edge filter) interrogator. FBG refers to the spectrum of the light reflected by a sensor FBG.

of this wavelength interrogator for an FBG sensor. The light transmittance of the filter is linearly dependent on wavelength. According to the linear response range, this type of filter is sometimes called an edge filter (which has a narrow linear range with a sharp slope, as a sharp edge of a bandpass filter) or a broadband filter (which has a wide range with a less sharp slope, as a boundary of a broadband filter). There is a tradeoff between the measurable range and the sensitivity.

This wavelength-change interrogator is based on intensity measurement. Information associated to wavelength variation is obtained by monitoring the intensity of the light beam after passing the filter at the detector. Many interrogators discussed in this subsection are based on the intensity measurement. For the intensity-based demodulators, the use of intensity referencing is necessary because the light intensity might be changed not only due to the reflection wavelength variation but also due to the power fluctuation of the light source, the disturbance in the light-guiding path, or the intensity dependence of light source on the wavelength. In other words, although the intensity-based measurement has the advantage of having a simple and compact structure, it does not use the key advantage of an FBG sensor: the fact that the information of the measurand is encoded spectrally, but not in its intensity. Fig. 2.6 shows the schematic diagram of the FBG sensor

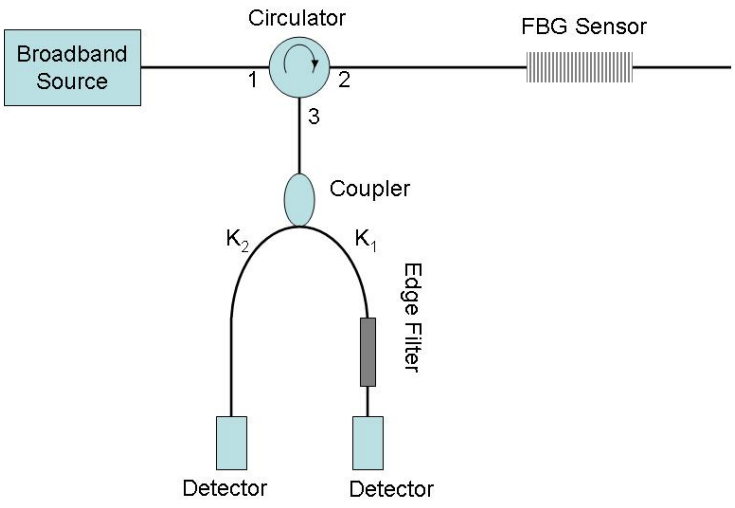

Figure 2.6: FBG sensor configuration with an edge filter as an interogator.

system adopting the wavelength dependent optical filter demodulator with the intensity referencing. The light reflected from the FBG is split into two paths; one of them passes through the wavelength-dependent filter, while the other one is used as a reference. The coupler has a K_1/K_2 splitting ratio, and the light split with a coupling ratio of $K_1/(K_1+K_2)$ is filtered. The linearized model of the filter function $F(\lambda)$ (see Fig. 2.5) can be expressed as

$$F(\lambda) = S(\lambda - \lambda_0), \tag{2.5}$$

where S is a constant determined by the slope of the filter and $F(\lambda)$ is equal to zero at λ_0. If we assume the narrow band reflected Bragg peak of the FBG has a Gaussian function of spectral width $\Delta\lambda$ (at $1/e$-intensity point) and the Bragg wavelength is λ_B, the output

intensity of the filtered I_S and reference I_R beams could be expressed as (Appendix B)

$$I_S = I_0 R S \frac{K_1}{K_1 + K_2} \frac{\sqrt{\pi}}{4} (\lambda_B - \lambda_0 + \frac{\Delta\lambda}{2\sqrt{\pi}}) \Delta\lambda, \tag{2.6}$$

and

$$I_R = I_0 R \frac{K_2}{K_1 + K_2} \frac{\sqrt{\pi}}{4} \Delta\lambda, \tag{2.7}$$

respectively, where I_0 is the intensity of the light incident on the FBG and R is the reflectivity of the FBG at Bragg wavelength. The intensity ratio at the two detectors is then given by [29]

$$\frac{I_S}{I_R} = S \frac{K_1}{K_2} (\lambda_B - \lambda_0 + \frac{\Delta\lambda}{2\sqrt{\pi}}). \tag{2.8}$$

Equation (2.8) is linearly dependent on the Bragg wavelength change but independent of light intensity variation due to the source fluctuations, etc. That is because the intensity variations are cancelled out by comparing the signal I_S with the reference I_R. Therefore, by measuring the power ratio change instead of the wavelength change, FBG spectral signal could be interrogated without using optical spectrum analyzers.

There are many kinds of edge filters that could be used for this intensity-based interrogation method. From the previous discussion, it is obvious that as long as the transmission spectrum of the filter has a linear region, it could be used as an edge filter for FBG sensor interrogation. Such filters could be wavelength division multiplexing couplers [30], biconical fiber filters [31], polarization-maintaining fiber loop mirror filters [32], etc., all of which have been developed for interrogating the FBG sensor systems.

Besides the edge filter based interrogation technique, many other passive detection schemes have already been reported. For example, Fallon *et al.* used an identical chirped grating pair with a quasi-square reflection spectrum to measure strain applied on one of the chirped grating (the sensing grating) [33]. When a strain is applied to the sensing grating, the received power increases due to the mismatch of the reflection spectra of the two gratings. This scheme can be extended to a multiplexing scheme [34], where multiple sensors are arranged in a serial or parallel or a combination of both. Another example is to use charge-coupled devices (CCDs) as interrogators. This technique is very suitable for multi-point fiber grating sensors. Light from FBGs incidents on a fixed diffractive element such as a finely ruled diffraction grating and then is focussed to a CCD. For a light incident to the diffraction grating, the diffraction angle is dependent on the light wavelength; therefore, lights with different wavelengths would illuminate different areas of pixels of the CCD [10, 35, 36].

II. Active Detection Schemes

Active detection scheme interrogators usually require more complex systems compared to the passive ones involving tracking, scanning, or modulating mechanisms to monitor Bragg wavelength shifts from single or multiple FBGs; however, the active schemes show better resolution, such as a Fourier transform spectrometer interrogator with a wavelength shift resolution of 15 pm [37] or even 5 pm [38], tunable Fabry-Pérot filter interrogator with a resolution of 1 pm [39], acousto-optic tunable filter interrogator [40], matched fiber Bragg grating pair interrogator [41], Mach-Zehnder interferometer interrogator [42], etc. Many other schemes have also been reported; however, since active demodulation technique is rather complex and only passive schemes would be used in this thesis, details of the active schemes will not be discussed. The theories and the applications for active detection schemes could be found in Ref. [43].

2.2 Fiber Interferometer Sensors

There are many kinds of fiber interferometers nowadays, such as Fabry-Pérot interferometers, Mach-Zehndner interferometers, etc., and many of them have already found applications in optical fiber sensors. Since the interfering spectra are usually directly related to the length of the optical path, these sensors have high sensitivity to many external perturbations, such as temperature, strain, pressure, etc. which could vary the optical path. In this section, several simple and basic interferometer sensors are introduced.

2.2.1 Fabry-Pérot Interferometer Sensors

The Fabry-Pérot interferometer (FPI), sometimes also called the Fabry-Pérot etalon, consists of two mirrors of reflectance R_1 and R_2 separated by a cavity of length L containing a medium of refractive index n. After its invention in the late 19th century [44], the bulk-optics version of the FPI has been widely used for high-resolution spectroscopy. In the early 1980s, the first results on fiber-optic versions of the FPI were reported. In the late 1980s, fiber FPIs began to be applied to sense temperature, strain, and ultrasonic pressure in composite materials. Fiber FPIs are extremely sensitive to perturbations that affect the optical path length between the two mirrors. The sensing region can be very compact. Mathematical analysis developed decades ago for the bulk FPI also applies to the fiber-optic versions of interest here. The individual mirrors in the FPI can be characterized by transmissions T_i and reflectivities R_i, such that $T_i + R_i = 1$ $(i = 1, 2)$. The excess loss, which corresponds to the portion of the incident power absorbed or scattered out of the

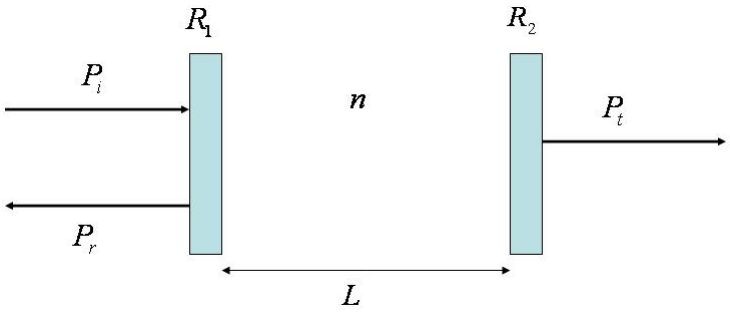

Figure 2.7: Fabry-Pérot interferometer, with P_i, P_r, and P_t the incident, reflected, and transmitted optical power, respectively.

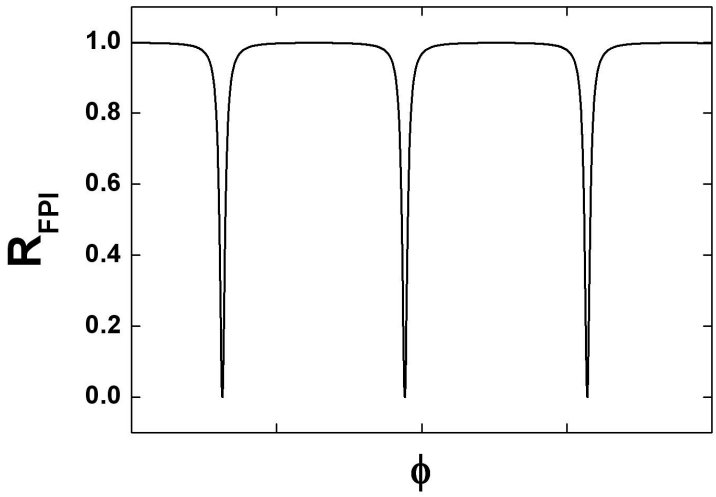

Figure 2.8: Typical Fabry-Pérot interferometer reflection spectrum.

beam by the mirror is neglected. The FPI reflectivity R_{FPI} and transmission T_{FPI} are found to be [45] (Appendix C)

$$R_{FPI} = \frac{R_1 + R_2 - 2\sqrt{R_1 R_2}\cos(2\phi)}{1 + R_1 R_2 - 2\sqrt{R_1 R_2}\cos(2\phi)}, \tag{2.9}$$

and

$$T_{FPI} = \frac{T_1 T_2}{1 + R_1 R_2 - 2\sqrt{R_1 R_2}\cos(2\phi)}, \tag{2.10}$$

where R_{FPI} represents the ratio of the power reflected by the FPI to the incident power; T_{FPI} is the ratio of the transmitted power to the incident power; and 2ϕ, the round-trip

propagation phase shift in the interferometer, is given by

$$2\phi = \frac{4\pi nL}{\lambda}, \tag{2.11}$$

with n the refractive index in the region between the mirrors and λ the free-space optical wavelength.

The typical reflection spectrum of the FPI is shown in Fig. 2.8. From Eq. (2.11), the phase is directly related to the refractive index n and length L. When the surrounding environment varies, the refractive index and the length changes, the phase will change, and the spectrum will shift. By monitoring the shift of the spectrum, fiber FPI could be used as an optical fiber sensor.

2.2.2 Fiber Mach-Zehnder Interferometer Sensors

The Mach-Zehnder interferometer (MZI) is a device used to determine the relative phase shift between two collimated beams from a coherent light source. The interferometer has been used, among other things, to measure small phase shifts in one of the two beams caused by a small sample or the change in length of one of the paths. They could be used as wavelength-dependent multiplexers [46] as well as optical fiber sensors. For the fiber

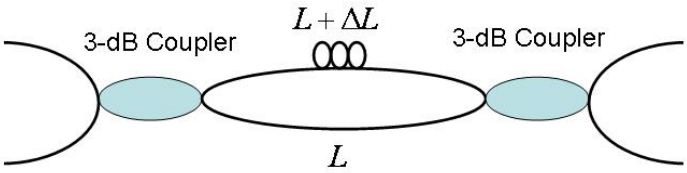

Figure 2.9: Configuration of a basic Mach-Zehnder interferometer, which consists of two 3-dB couplers, two arms with different length.

MZI, the principle is the same as bulk-optics based MZI. Fig. 2.9 illustrates an individual fiber MZI. This MZI consists of three stages, an initial 3-dB directional coupler which splits the input signals, a central section where one of the fiber lengths is longer by ΔL than the other to give a wavelength dependent phase shift between the two arms, and another 3-dB coupler which recombines the signals at the output. In the central region, when the signals in the two arms come from the same light source, the outputs from these two guides have a phase difference $\Delta\phi$ given by

$$\Delta\phi = \frac{2\pi n_1}{\lambda}(L + \Delta L) - \frac{2\pi n_2}{\lambda}L. \tag{2.12}$$

Note that this phase difference can arise either from a different path length (given by ΔL) or through a refractive index difference if $n_1 \neq n_2$. Here, we take both arms to have the same index and let $n_1 = n_2 = n$ (e.g., the same optical fiber for the two paths). Then we can write Eq. (2.12) as

$$\Delta\phi = \frac{2\pi n}{\lambda}\Delta L. \tag{2.13}$$

The typical transmission spectrum of an MZI is shown in Fig. 2.10. From Eq. (2.13), we

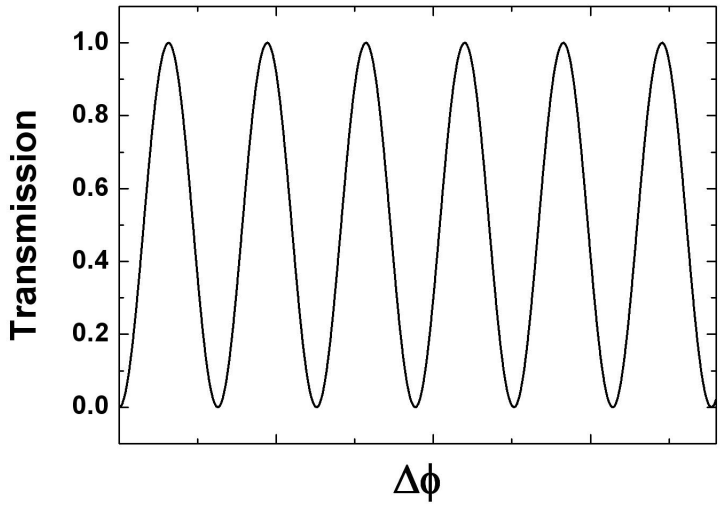

Figure 2.10: Typical transmission spectrum of an Mach-Zehnder interferometer.

see that it is very similar to the case of the fiber FPI for sensing application. As long as the environment change modifies the refractive index or the length of the fiber, the phase will change, so does the spectrum. By monitoring the spectrum shift, it is feasible to obtain the environmental change information.

2.2.3 Multimode Fiber Interferometer Sensors

Recently, all-fiber MZI sensors based on mode interference have increasingly aroused research interests because they are compact and easy to fabricate [47, 48, 49, 50, 51, 52, 53]. Multimode fiber (MMF) interferometer is one kind of fiber MZI. The sensor configuration is shown in Fig. 2.11: a section of MMF is sandwiched between two single-mode fibers (SMFs). The fundamental mode that propagates along the SMF will couple into the MMF. When the light couples into the MMF, many modes are excited, each of which has a different propagation constant. When they recouple back into the SMF after passing through a section of MMF, the modes interfere, since each mode has experienced a different phase

Figure 2.11: Schematic of all-fiber multimode fiber interferometer. SMF: single-mode fiber; MMF: multimode fiber; OSA: optical spectrum analyzer.

shift (This could be considered as the case of MZI because different modes have passed different lengths of optical path due to the different propagation constants). If only two dominant modes (LP_{01} and LP_{02}) are excited, the resultant interference fringe pattern is approximately sinusoidal with a uniform extinction ratio determined by the ratio of the intensities in the two modes (e.g., the best mode operation is to launch equal power in the two modes). If other higher-order modes are excited, the interference fringe pattern will be modulated by their presence, shown in Fig. 2.12. In MMFs, most of the power

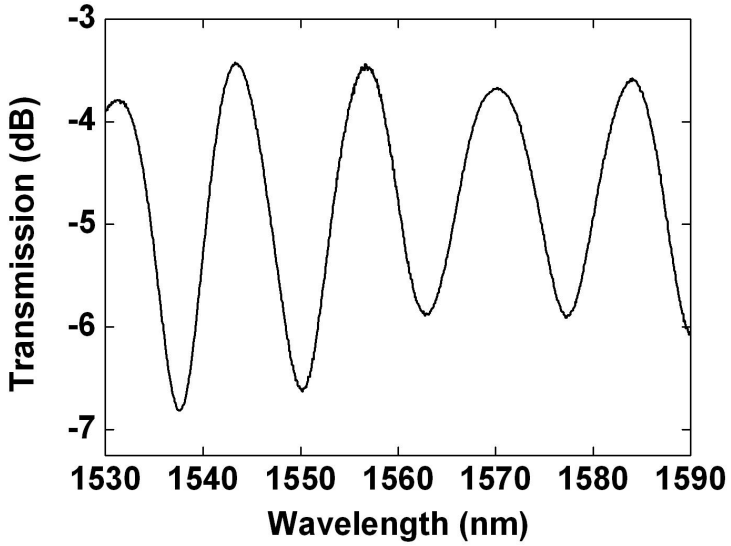

Figure 2.12: Typical transmission spectrum of a multimode fiber interferometer.

will be dominantly distributed in the lowest-order mode while only a small portion power propagates in the higher-order modes. Therefore, it is reasonable to consider only two lowest-order modes; then, the measured intensity of the MMF interferometer is given by

$$I = I_1 + I_2 + 2\sqrt{I_1 I_2}\cos(\frac{2\pi\Delta nL}{\lambda}), \tag{2.14}$$

where I_1 and I_2 are the intensities distributed in the first and the second-order modes, respectively; I is the measured intensity; L is the length of the MMF; λ is the light

wavelength in vacuum; $\Delta n = n_2 - n_1$, and n_1 and n_2 are the mode indices. Therefore, a section of MMF sandwiched between two SMFs serves as an MZI and can be used as a sensor. The free spectral range (FSR) of the interfering spectrum is given by Eq. (2.14) as $FSR \approx \lambda^2/(\Delta n L)$.

When a strain is applied to the MMFs or ambient temperature changes, the mode indices and the fiber length will change, and thus the transmission peaks will shift. When the phase in Eq. (2.14) equals $2N\pi, (N = 1, 2, 3, ...)$ for a wavelength, the transmission reaches its peak value at this wavelength as

$$\lambda = \Delta n L/N. \tag{2.15}$$

By differentiating Eq. (2.15), we have (Appendix D)

$$\frac{\Delta\lambda}{\lambda} \approx \left[\frac{1}{\Delta n}\frac{\partial(\Delta n)}{\partial T} + \frac{1}{L}\frac{\partial L}{\partial T}\right]\Delta T + \left[1 + \frac{1}{\Delta n}\frac{\partial(\Delta n)}{\partial \varepsilon}\right]\varepsilon, \tag{2.16}$$

where, $\varepsilon = \Delta L/L$ indicates the applied strain. Eq. (2.16) is very similar to the expression that describes the Bragg wavelength shift of an FBG with respect to the temperature and applied strain. Both the changes of the strain and temperature contribute to the wavelength shifts. By monitoring the wavelength shifts of the spectrum, it is feasible to use the MMF based interferometer as an optical fiber sensor.

2.2.4 High-Birefringence Fiber Loop Mirror Interferometer Sensors

Fiber loop mirror (FLM) is a very attractive device for use in optical fiber communications or for use as an optical fiber sensor [54]. A high-birefringence fiber loop mirror (HBFLM) is a specific fiber loop mirror which is usually formed by a 3-dB optical coupler, a polarization controller, and a section of high-birefringence fiber (HBF), as shown in Fig. 2.13. The HBFLM acts like a bandpass filter for the input signal. The input light is split into two beams propagating clockwisely and counterclockwisely by means of the 3-dB coupler. Each of the resultant beams is decomposed into two beams after it travels through the HBF. The polarization controller changes the polarization states of both the clockwise and counterclockwise beams. The counterpropagating beams recombine at the coupler and exhibit interference due to the phase difference experienced in the HBF for different polarization components. The transmission spectrum of the HBFLM is approximately a periodic function of the inverse wavelength as follows (Appendix E)

$$T(\lambda) = [\sin(\theta_1 + \theta_2)\cos\left(\frac{\pi B L}{\lambda}\right)]^2, \tag{2.17}$$

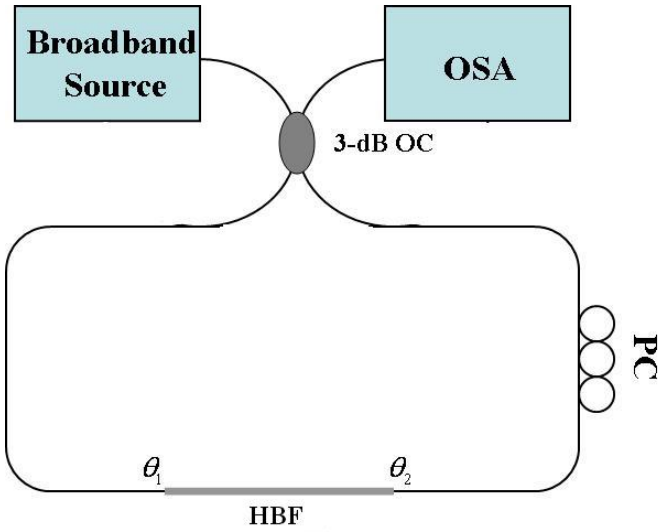

Figure 2.13: Schematic of a high-birefringence fiber loop mirror; PC: polarization controller; OSA: optical spectrum analyzer; OC: optical coupler; HBF: high-birefringence fiber.

where θ_1 and θ_2 are the angles between the light at both ends of the HBF and the fast or slow axis of the HBF, respectively; and B, L and λ are the birefringence, the length of HBF and the operation wavelength, respectively. Thus, the HBFLM characteristic is similar to an MZI and can be used as a sensor. The FSR of the HBFLM filter interference spectrum can be given by Eq. (2.17) as:

$$FSR \approx \frac{\lambda^2}{BL}. \tag{2.18}$$

The transmission spectrum of the HBFLM is shown in Fig. 2.14. When a strain applied on the HBF or there is a temperature change, the spectrum of the HBFLM would shift. Hence, the HBFLM could be used as an optical fiber sensor.

2.3 Measurands Discrimination

In general, optical fiber sensing elements are sensitive to two or many parameters simultaneously, which could be confirmed by the discussion in the last two sections. Two-parameter or multi-parameter measurement is an important topic in optical fiber sensing field, not only because it could in general minimize the complexity, size, and cost of the sensing systems, but also because it could perform multi-parameter discrimination in situations where cross-sensitivity is a crucial issue. For example, the measurement of slowly varying strain

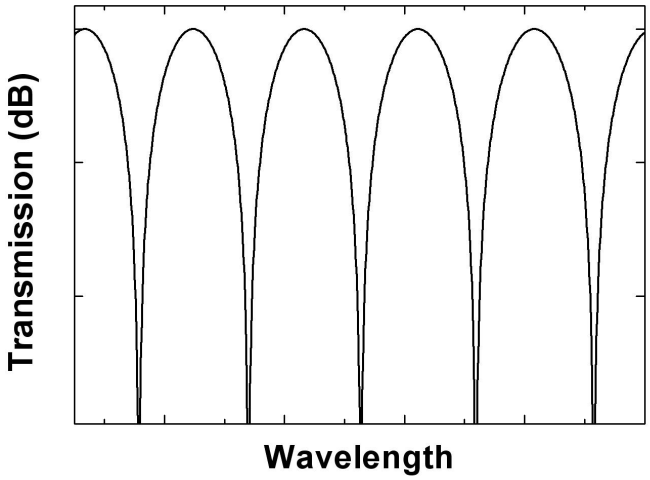

Figure 2.14: Typical transmission spectrum of a high-birefringence fiber loop mirror.

is an important application of optical fiber sensors, but such measurement is very often severely influenced by the surrounding temperature variation. Hence, measuring these two parameters simultaneously ia very necessary. The simplest way of discriminating strain and temperature is to use two separated sensing elements. The first element is isolated from strain. Provided the two sensing elements are under the same temperature, the output from the first sensor can be used to obtain an actual strain value which excludes the temperature influence from the second one. However, when sensors must be embedded with minimum intrusion on the measurement structure, the use of a second sensing element is not a good choice. In these cases, strain and temperature discrimination (or sets of other measurands) must be realized by a single sensing element with a compact configuration.

The reason of measurands cross-sensitivity could be understood easily. As examples, from the discussion in the last two sections, all the equations indicating the spectrum or phase shift is related to both the temperature and strain variation simultaneously. Similarly, other environment perturbations would also result in the spectrum change. To date, many sensor configurations have already been developed for different parameter discrimination. The first sensing head reported for the simultaneous measurement of strain and temperature was demonstrated by Xu *et al.* in 1994 [55, 56]. They used two superimposed FBGs operating at two different wavelengths for temperature and strain discrimination, since the two Bragg wavelengths have slightly different sensitivities with respect to temperature and strain respectively. Later on, similar idea has been adopted by many other groups around the world, and a large mount of work has been reported on this topic. For example, different schemes have been developed for temperature and strain discrimination [27, 28, 57, 58, 59, 60], displacement and temperature discrimination [61, 62, 63, 64, 65, 66], pressure and temperature discrimination [67, 68, 69], strain and curvature discrimination

[70], etc.

The principle of this idea that allows simultaneous measurement of two parameters is that the two characteristics of the sensing head structure that change differently under the action of the measurands. If this is the case, it is always possible to write down two independent equations that permit explicit solutions of the actual value of each measurands. This idea could be easily applied to the case that more than two parameters need to be measured. In the following text, the detailed theoretical analysis for the recovery of strain and temperature is given. The applications for other cases could be easily extended from the discussion below.

To recover temperature and strain variations from a single sensing fiber, measurements are made on two parameters at the same time. The parameters that can be measured, θ_1 and θ_2, usually assumed to be related to the desired measurands (e.g., temperature and strain) through a linear transform represented in matrix format as:

$$\Theta = K\Psi, \tag{2.19}$$

where

$$\Theta = \begin{bmatrix} \theta_1 \\ \theta_2 \end{bmatrix}, \tag{2.20}$$

and

$$\Psi = \begin{bmatrix} \Delta T \\ \varepsilon \end{bmatrix}, \tag{2.21}$$

and

$$K = \begin{bmatrix} K_{T1} & K_{\varepsilon 1} \\ K_{T2} & K_{\varepsilon 2} \end{bmatrix}. \tag{2.22}$$

K is usually referred to as the transfer matrix from Ψ to Θ or the characteristic matrix of the sensor. If the determinant of K, D

$$D = K_{T1}K_{\varepsilon 2} - K_{T2}K_{\varepsilon 1}, \tag{2.23}$$

is not equal to zero, Eq. (2.19) could be inverted and ΔT and ε could be calculated as

$$\Psi = K^{-1}\Theta. \tag{2.24}$$

In the above equation, K^{-1} represents the inverse of matrix K and can be written as

$$K^{-1} = \frac{1}{D}\begin{bmatrix} K_{\varepsilon 2} & -K_{\varepsilon 1} \\ -K_{T2} & K_{T1} \end{bmatrix}. \tag{2.25}$$

The recovery of temperature and strain is influenced by a range of errors that include the precision with which Θ can be determined and any errors presented in the estimation of the elements of the matrix K (usually determined from calibration experiments).

For given measurement errors,$\delta(\theta_1)$ and $\delta(\theta_2)$, the tolerance of the measured strain and temperature change are given by:

$$\begin{bmatrix} \delta(\Delta T) \\ \delta(\varepsilon) \end{bmatrix} = abs\left(K^{-1}\right) \begin{bmatrix} \delta(\theta_1) \\ \delta(\theta_2) \end{bmatrix} \tag{2.26}$$

The measurement errors of θ's are determined by the resolution of equipment and the measurement bandwidth, which is true for all optical sensing applications. Large absolute value of the coefficient matrix determinant D is usually desirable for high-resolution measurement. By properly designing the sensing head, it is feasible to achieve temperature and strain discrimination with high resolution. With this basic principle, the next problem is to design the sensing head with two characteristics that change differently under the action of the measurands. The next two chapters will present several novel configurations which could realize temperature and strain discrimination with this idea.

Chapter 3

Simultaneous Measurement of Strain and Temperature with Fiber Bragg Grating and Multimode Fibers

3.1 Introduction

There has been considerable interest in developing methods which enable optical fibers to measure strain and temperature simultaneously [1, 2, 3, 4, 5, 6, 7, 8, 9, 10, 11, 12, 13]. These optical fiber sensors are usually made by detecting two physical parameters which have different sensitivities to temperature and strain. Fiber Bragg gratings (FBGs) have been of great interest in optical sensing technology in recent years because they are small, cost-effective, easy to manufacture, and their optical spectra have good linear responses with respect to variations of temperature and strain. Many techniques based on FBGs have been reported for simultaneous strain and temperature discrimination, such as using two superimposed FBGs [3, 4], two resolvable wavelengths in a tilted FBG [5], two FBGs written in fibers of different diameters [6] or compositions [7], and a single FBG written across a splice point between fibers of different refractive index [8] or between fibers with different levels of doping elements [9]. Alternatively, the measurement from an FBG may be combined with that of a different sensing technique, such as using hybrid FBG/long-period fiber grating (LPG) [10], superstructure FBG [11], a sampled FBG combined with an LPG [12], and an FBG combined with a polarization-maintaining fiber loop mirror [13]. Many other techniques can also be found in the review article [14] on this topic.

On the other hand, all fiber Mach-Zehnder interferometer (MZI) sensors based on mode interference have increasingly aroused research interests in the past several years, because they are compact and easy to fabricate. For example, Wang and Farrell proposed an all-

fiber multi-mode-interference-based refractometer for chemical sensing [15], Mehta *et al.* investigated multi-mode interference-based MZIs for displacement sensors [16], and Frazão *et al.* demonstrated a curvature sensor based on multimode interference combined with an LPG [17]. Temperature and strain sensors were also widely studied based on all-fiber MZIs, but employing different multi-mode fibers (MMFs) [18, 19, 20, 21]. Since MMF has different strain and temperature sensitivity responses from those of the FBG, it is feasible to realize simultaneous measurement of the strain and temperature variations based on their combination.

In the second section of this chapter, an all-fiber sensor is presented for simultaneous strain and temperature discrimination using an FBG combined with a section of MMF as a sensing head. The MMF acts as an MZI and the interference fringes are sensitive to the applied strain and ambient temperature. By measuring the resonance wavelength shifts of the MMF and the FBG, the applied strain and temperature changes can be determined simultaneously. The sensor resolution depends not only on the sensitivities of the individual sensing heads but also on their combination. Three kinds of MMFs and two FBGs are used in the experiment, and the sensitivity performances of three combinations are investigated. The experimental results show that the strain and temperature coefficients of the MMF are very different for different fiber core sizes and materials, and high resolution could be achieved by selecting a suitable combination of the MMF and FBG. This feature may provide a new approach to optimize the sensor resolution.

However, the scheme that an FBG is cascaded with a section of MMF has to use an optical spectrum analyzer (OSA) [22] to monitor the spectrum shift. Since OSAs are very expensive and have slow scanning speed, there is considerable interest in developing interrogation methods for FBG sensors, whose measurand information is encoded spectrally, by monitoring the change of parameters other than the resonance wavelength shifts. Many passive detection interrogators involving no tracking, scanning, or modulating mechanisms have been reported, such as using linearly wavelength-dependent devices [23, 24, 25, 26], identical chirped grating pairs [27], and charge-coupled device (CCD) spectrometers [28]. For active detection schemes which require more complex systems compared to the passive ones, Fabry-Pérot filter interrogators [29], fiber Fourier transform spectrometer interrogators [30], and many other techniques have also been demonstrated. The most cost-effective method among both the passive and active schemes is to develop an intensity-based interrogation system using a linearly wavelength-dependent optical filter. Sensor systems that adopt this type of demodulator have been commercialized.

In the third section of this chapter, an improved configuration suitable for simultaneous strain and temperature measurement using an FBG combined with two sections of MMFs based on this intensity-based interrogation technique is demonstrated. The two sections of MMFs act as edge filters with one of them dependent on temperature change. By measuring power changes instead of spectrum shifts, simultaneous temperature and strain

measurement can be achieved at a lower cost and higher speed compared to the scheme in Section 3.2. In addition, compared to Refs. [23, 24, 25, 26] where an infrared high-pass filter, a wavelength-division-multiplexing coupler, a biconical fiber filter, and a polarization-maintaining fiber loop mirror filter are used, the MMF filter is easier to make and more cost-effective.

3.2 FBG Cascades with MMF

An all-fiber sensor capable of simultaneous measurement of temperature and strain is presented. The sensing head is formed by an FBG combined with a section of MMF that acts as an MZI for temperature and strain discrimination. The strain and temperature coefficients of the MMFs vary with the core sizes and materials. This feature can be used to improve the strain and temperature resolution by suitably choosing the MMF. However, in order to extract the information from the sensing head, an optical spectrum analyzer has to be used, which makes the system expensive and have a slow scanning speed. In Section 3.3, an improved design will eliminate these drawbacks by measuring the optical power changes instead of monitoring the spectrum shifts.

3.2.1 Experiment Setup

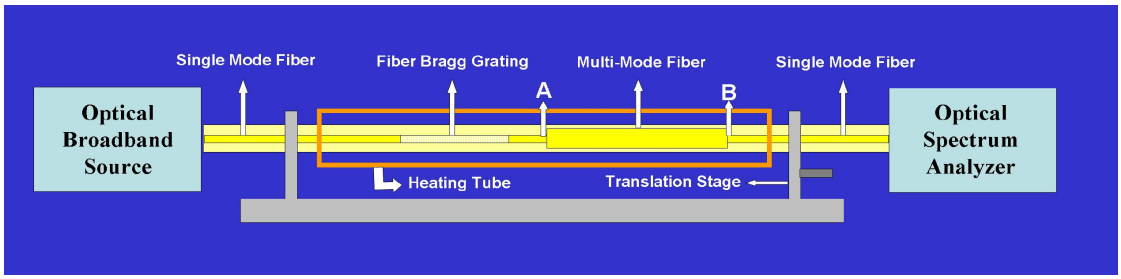

Figure 3.1: Experiment setup: an FBG cascaded with a section of MMF for strain and temperature discrimination.

As shown in Fig. 3.1, the FBG and MMF are spliced to form an all-fiber transmission-type sensor. The FBG is written in SMF-28. The section of MMF acts as an MZI. The proposed scheme is actually a special filter with an FBG followed by an all-fiber MZI. The fundamental mode that propagates along the single-mode fiber (SMF) will couple into the MMF at splice point A, and the power will be dominantly distributed in the lowest-order mode, while only a small portion of power propagates in the higher-order modes. The

different modes will interfere and recouple into the SMF at splice point B. When only the first two lowest-order modes are considered, the measured intensity is given by

$$I = I_1 + I_2 + 2\sqrt{I_1 I_2}\cos(\frac{2\pi\Delta nL}{\lambda}), \tag{3.1}$$

where I_1 and I_2 are the intensities distributed in the first and the second-order modes, respectively; I is the measured intensity; L is the length of the MMF; λ is the light wavelength in vacuum; $\Delta n = n_2 - n_1$, and n_1 and n_2 are the mode indices. The free spectral range (FSR) of the interfering spectrum is given by Eq. (3.1) as $FSR \approx \lambda^2/(\Delta nL)$.

When a strain is applied to the MMF or ambient temperature changes, the mode indices and the fiber length will change, and thus the transmission peaks will shift. When the phase in Eq. (3.1) equals $2N\pi, (N = 1, 2, 3, ...)$ for a wavelength, the transmission reaches its peak value at this wavelength as

$$\lambda = \Delta nL/N. \tag{3.2}$$

By differentiating Eq. (3.2), we have

$$\frac{\Delta\lambda}{\lambda} \approx \left[\frac{1}{\Delta n}\frac{\partial(\Delta n)}{\partial T} + \frac{1}{L}\frac{\partial L}{\partial T}\right]\Delta T + \left[1 + \frac{1}{\Delta n}\frac{\partial(\Delta n)}{\partial \varepsilon}\right]\varepsilon, \tag{3.3}$$

where, $\varepsilon = \Delta L/L$ indicates the applied strain. Eq. (3.3) is very similar to the expression that describes the resonance shift of FBGs with respect to the temperature and applied strain [11]. Both the changes of the strain and temperature contribute to the wavelength shifts. If the sensitivities of the temperature and strain of the MMF are different from those of the FBG, simultaneous measurement of temperature and strain can be achieved using this simple scheme.

Next, we consider the case that a strain is applied to both the MMF and FBG or an ambient temperature of both the MMF and FBG changes. Then, the mode indices, the fiber length and the grating pitch will change; therefore, the resonance wavelengths will shift. The shifts of the resonance wavelengths for the FBG and MMF can be expressed as:

$$\begin{bmatrix} \Delta\lambda_{FBG} \\ \Delta\lambda_{MMF} \end{bmatrix} = \begin{bmatrix} \alpha_{FBG} & \zeta_{FBG} \\ \alpha_{MMF} & \zeta_{MMF} \end{bmatrix} \begin{bmatrix} \varepsilon \\ \Delta T \end{bmatrix}, \tag{3.4}$$

where $\Delta\lambda_{FBG}$ and $\Delta\lambda_{MMF}$ are FBG and MMF wavelength shifts; ε and ΔT are applied strain and ambient temperature change, respectively; and α_{FBG}, ζ_{FBG}, α_{MMF}, and ζ_{MMF} are the corresponding strain and temperature coefficients that can be determined by experiment. The applied strain and the temperature changes can then be simultaneously obtained from Eq. (3.4):

$$\begin{bmatrix} \varepsilon \\ \Delta T \end{bmatrix} = M^{-1} \begin{bmatrix} \Delta\lambda_{FBG} \\ \Delta\lambda_{MMF} \end{bmatrix}, \tag{3.5}$$

where

$$M^{-1} = \frac{1}{D} \begin{bmatrix} \zeta_{MMF} & -\zeta_{FBG} \\ -\alpha_{MMF} & \alpha_{FBG} \end{bmatrix}, \tag{3.6}$$

with $D = \alpha_{FBG}\zeta_{MMF} - \alpha_{MMF}\zeta_{FBG}$, the determinant of the coefficient matrix. For given wavelength measurement errors, $\delta(\Delta\lambda_{FBG})$ and $\delta(\Delta\lambda_{MMF})$, the tolerance of the measured strain and temperature are given by:

$$\begin{bmatrix} \delta(\varepsilon) \\ \delta(\Delta T) \end{bmatrix} = abs\left(M^{-1}\right) \begin{bmatrix} \delta(\Delta\lambda_{FBG}) \\ \delta(\Delta\lambda_{MMF}) \end{bmatrix}. \tag{3.7}$$

The wavelength measurement errors are determined by the resolution of the OSA and the bandwidth of the FBG and MMF resonance, which is true for all optical sensing applications. A large absolute value of the coefficient matrix determinant is usually desirable for high-resolution measurement. Fortunately, we found that the strain and temperature coefficients of the MMFs could vary over a large range with the core sizes and materials. This may provide us a very easy and cost-effective approach to improve the sensing resolutions for simultaneous strain and temperature measurements by choosing the MMF with proper strain and temperature coefficients.

3.2.2 Experiment Results and Discussion

As shown in Fig. 3.1, the experiment setup consists of an optical broadband source, an FBG, a section of MMF and SMF, and an OSA with a resolution of 0.06 nm. The sensing head is placed in a copper tube with a diameter of 1.5 cm, which is wrapped by a heating tape to control the ambient temperature change surrounding the sensing head. A digital thermometer is inserted inside the heating tube (through a very small aperature) to monitor the temperature. One side of the fiber is attached to a translation stage with a resolution of 10 μm to control the applied strain. Three different kinds of MMFs, $\text{MMF}_i (i = 1, 2, 3)$ and two FBGs, $\text{FBG}_j (j = 1, 2)$ are used in our experiment. All three of these MMFs and the two FBGs are commercially available. Table 3.1 lists the standard parameters and lengths of the MMFs used in our experiment as well as the wavelength spacing of the resultant interference spectrum. Note that MMF_3 is originally designed for dispersion compensation applications, with a large dispersion parameter of -270 ps/nm/km at 1550 nm and a cutoff wavelength of 1663 nm. Table 3.2 lists the center wavelengths, reflectivity, and optical bandwidths of the FBGs.

Table 3.1: Typical parameters and segment lengths of MMFs used in the experiment and wavelength spacing of the resultant interference spectrum

Fiber Type	Numerical Aperature	Core/Cladding Diameter (μm)	Length (m)	Wavelength Spacing (nm)	Company
MMF_1	0.29	100/140	1.4	6.4	POFC
MMF_2	0.275	62.5/125	1.4	6.8	POFC
MMF_3	0.342	1.9/115.7	0.24	0.5	Sumitomo Electric

Table 3.2: Center wavelength, reflectivity and optical bandwidth of the FBGs used in the experiment

FBG	Center wavelength (nm)	Reflectivity	Optical bandwidth (nm)
FBG_1	1560.05	84.5%	0.21
FBG_2	1560.03	63.1%	0.17

Three different combinations, $Scheme_1$ (FBG_1 combined with MMF_1), $Scheme_2$ (FBG_2 combined with MMF_2), and $Scheme_3$ (FBG_1 combined with MMF_3) are studied. Figs. 3.2-3.4 show the transmission spectra of $Scheme_1$, $Scheme_2$ and $Scheme_3$, respectively, carrying the spectral responses from both the FBG and MMF, which together can be used as sensing head for temperature and strain discrimination. The length of each MMF, MMF_1, MMF_2 and MMF_3, is approximately 1.4 m, 1.4 m and 24 cm, resulting in the wavelength spacing 6.4 nm, 6.8 nm and 0.5 nm, respectively. The interfering visibility is determined by the ratio of the intensities of the two interfering modes; when $I_2/(I_1 + I_2) = 1\%$, 7% and 15.2%, the extinction ratio is approximately 2 dB, 5 dB and 8 dB, respectively. In Fig. 3.4, we optimize the extinction ratio from 2 dB to 8 dB, by slightly offsetting the center of the core of SMF with respect to that of the MMF_3 at point A, but without offsetting at point B, in order to obtain two modes with similar amounts of power to interfere with each other [9]. However, this introduces significant loss to the transmission about 6 dB. Further improvement of the extinction ratio may be obtained by offsetting both ends, but with the compromise of the insertion loss.

The applied strain and ambient temperature changes can be determined by measuring the resonance wavelength shifts of the FBG and MMF. To determine the strain and temperature coefficients, strain and temperature changes are applied to the fiber separately. We first measure the strain responses of the FBG and MMF by measuring the wavelength shifts as a function of the applied strain under the room temperature of 22 °C, as shown in Figs. 3.5-3.7. Figs. 3.8-3.10 show the wavelength shifts of the FBG and MMF with respect to temperature changes when the tube is heated from 22 °C to 90 °C under zero strain.

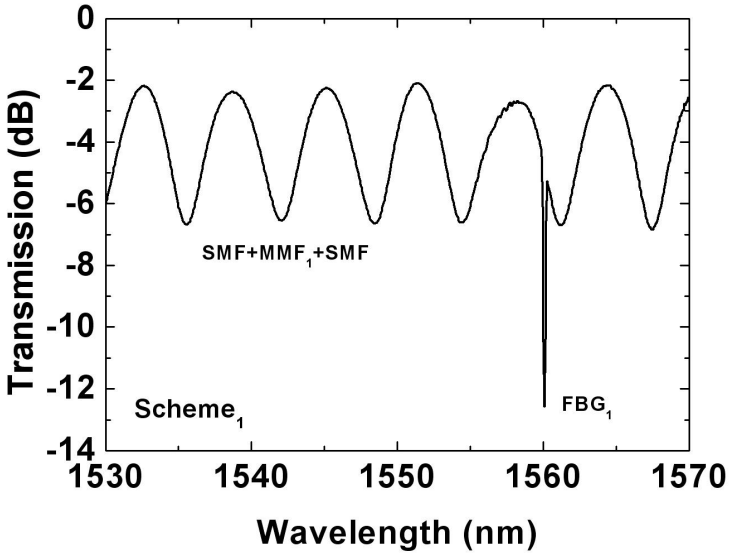

Figure 3.2: Transmission spectrum shows that the FBG_1 spectrum is superimposed on that of the MMF_1.

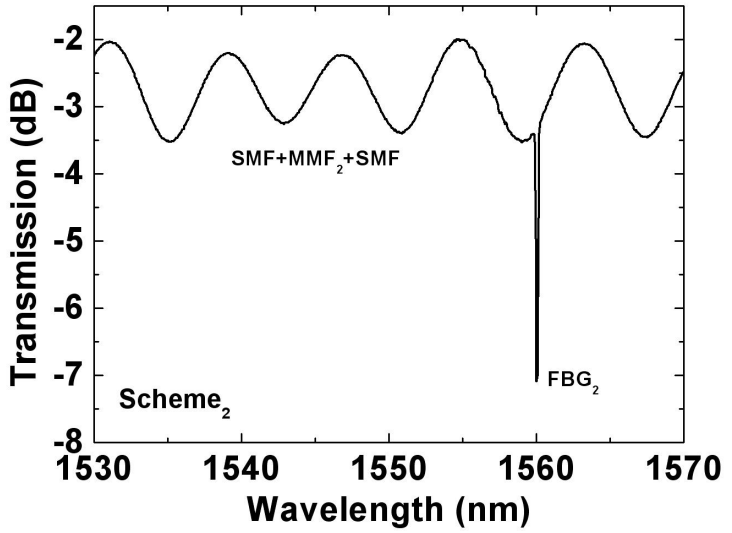

Figure 3.3: Transmission spectrum shows that the FBG_2 spectrum is superimposed on that of the MMF_2.

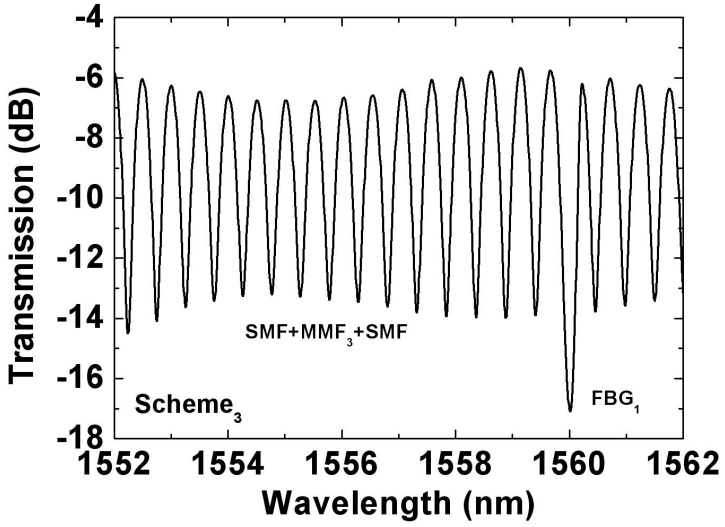

Figure 3.4: Transmission spectrum shows that the FBG_1 spectrum is superimposed on that of the MMF_3.

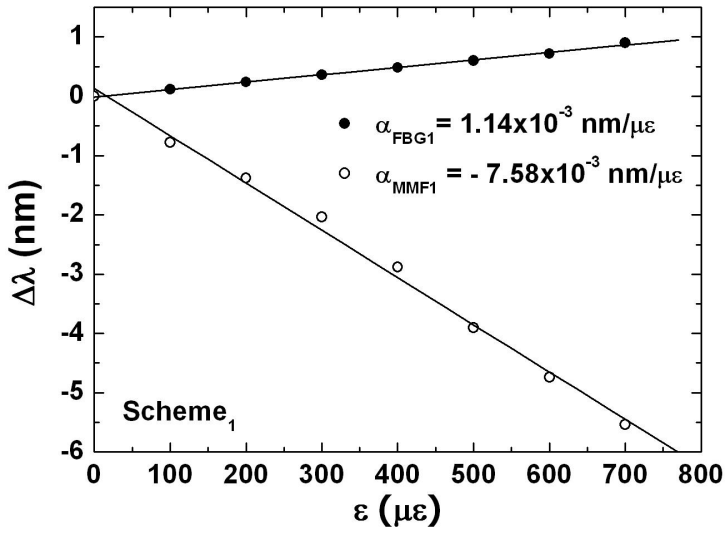

Figure 3.5: Wavelength shifts as a function of applied strain for FBG_1 combined with MMF_1.

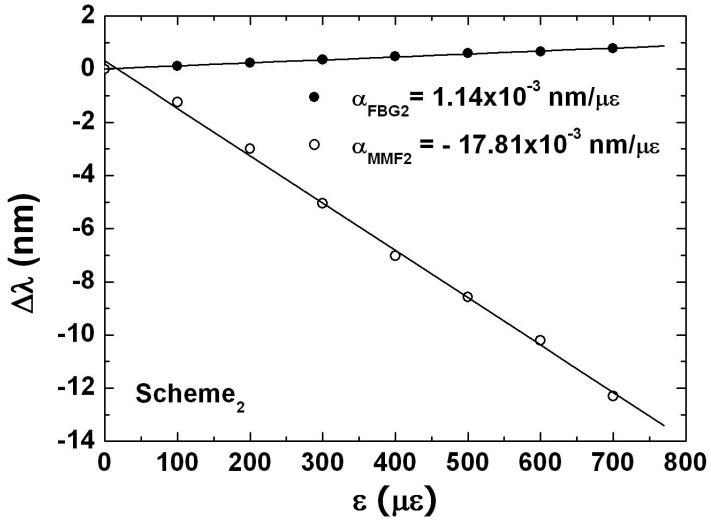

Figure 3.6: Wavelength shifts as a function of applied strain for FBG_2 combined with MMF_2.

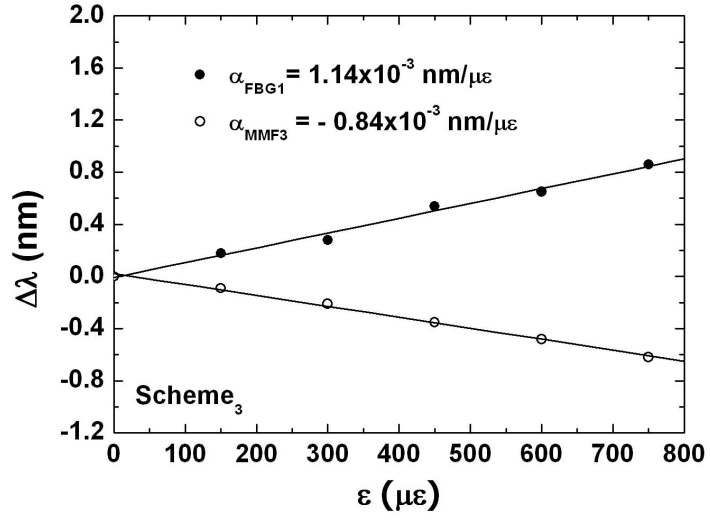

Figure 3.7: Wavelength shifts as a function of applied strain for FBG_1 combined with MMF_3.

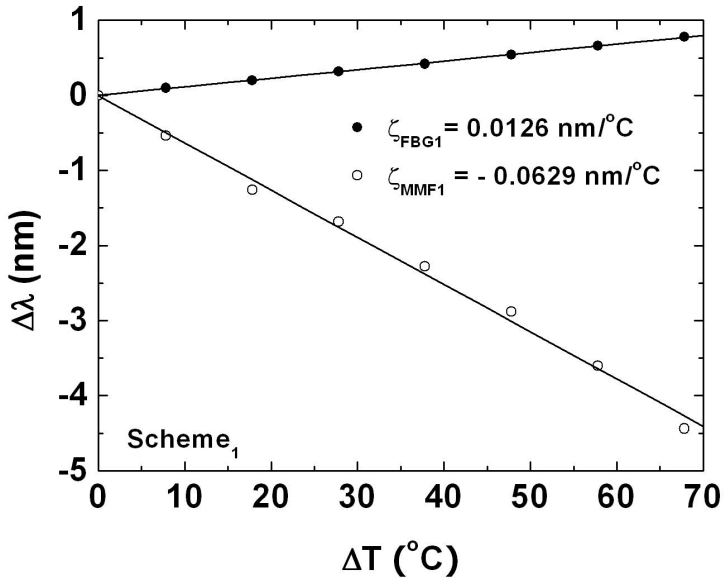

Figure 3.8: Wavelength shifts as a function of ambient temperature for FBG_1 combined with MMF_1.

The slopes of the curves in each of Figs. 3.5-3.10 are used to extract the values of the α's and ζ's shown inside the figure frames. It can be seen that the measured wavelength shifts have a good linear behavior with variations in strain and temperature. Note that the strain and temperature coefficients of the MMFs are very different: there are all blue shifts for the strain responses (i.e. negative slopes), while there are one redshift and two blueshifts for the temprature responses. Both the spectra of FBGs and MMFs are almost linearly shifted with temperature and strain, respectively, over the measurement ranges, which makes it reasonable to omit the contribution of the cross-sensitivity.

For given measurement errors of wavelength shifts, the strain and temperature errors are given in Eq. (3.7). Assuming a wavelength resolution of 10 pm for the FBG and MMF, the measurement errors of the strain and temperature for the three combinations are listed in Table 3.3. The condition number [31] of the coefficient matrix for each combination is also list in Table 3.3, which provides a common method of assessing the performance of a temperature-strain discrimination system. A smaller condition number is preferred. It is very clear that the combination of FBG_1+MMF_3 (with the smallest condition number) results in good strain and temperature resolutions of 9.21 $\mu\varepsilon$ in strain and 0.26 °C in temperature, whereas $3-10$ times resolution degradation are obtained for the other two combinations (with much greater condition numbers). Note that for the combination of FBG_1+MMF_3, the strain responses are in opposite directions (i.e., one has a blueshift and the other has a redshift), and the temperature responses are in the same direction (i.e.,

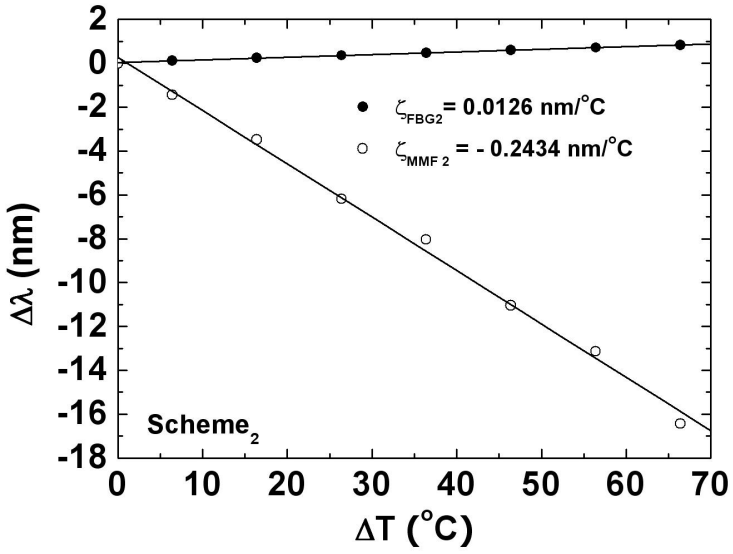

Figure 3.9: Wavelength shifts as a function of ambient temperature for FBG_2 combined with MMF_2.

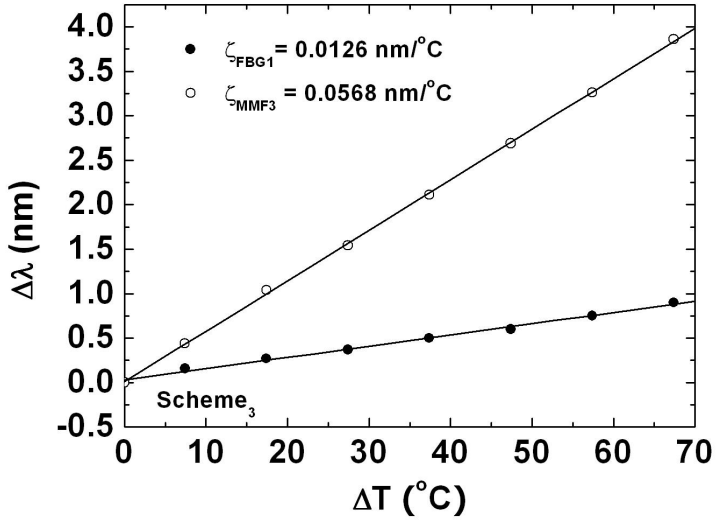

Figure 3.10: Wavelength shifts as a function of ambient temperature for FBG_1 combined with MMF_3.

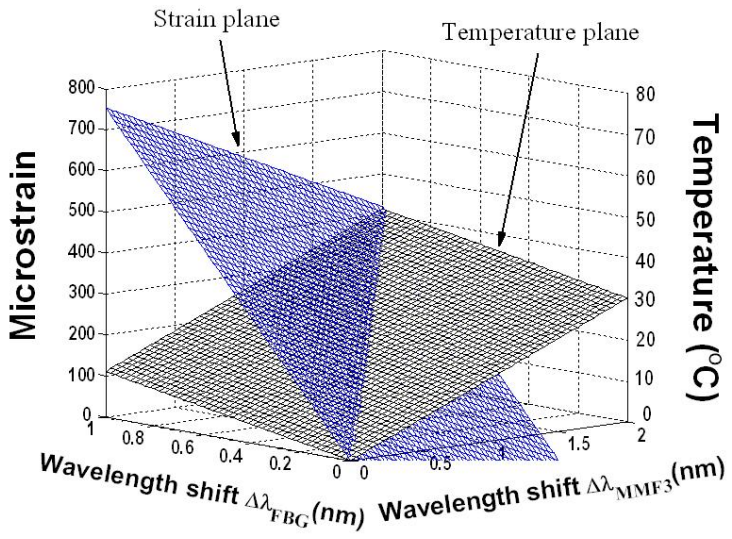

Figure 3.11: 3D plot illustrating simultaneous measurement of strain and temperature by measuring the wavelength shifts of the FBG_1 and MMF_3.

both have a redshift). This suggests that when using the combination of two types of fiber-based elements with similar sensitivities as a sensing head for simultaneous measurement of temperature and strain, it is desirable to choose the two elements with opposing trends in one type of measurement (e.g., strain) and similar but distinct trends in the other type of measurement (e.g., temperature). For the proposed structure based on MMF and FBG, by properly selecting the MMF, one may obtain a high sensing resolution for simultaneous strain and temperature measurement.

Table 3.3: Coefficient matrices, matrix condition number, and corresponding resolutions of strain and temperature for the combination of FBG_i + MMF_i

Combinations of Sensor Head	Coefficient Matrix (M)	Inversed Coefficient Matrix (M^{-1})	Matrix Condition No.	Resolution $\begin{bmatrix} strain(\mu\varepsilon) \\ temperature(^oC) \end{bmatrix}$
FBG_1+MMF_1	$\begin{bmatrix} 1.14\times10^{-3} & 0.0126 \\ -7.58\times10^{-3} & -0.0629 \end{bmatrix}$	$\begin{bmatrix} -2.6426 & -0.5294 \\ 0.3185 & 0.0479 \end{bmatrix}\times10^3$	175.36	$\begin{bmatrix} 31.72 \\ 3.66 \end{bmatrix}$
FBG_2+MMF_2	$\begin{bmatrix} 1.14\times10^{-3} & 0.0126 \\ -17.81\times10^{-3} & -0.2434 \end{bmatrix}$	$\begin{bmatrix} 4.5864 & 0.2374 \\ -0.3356 & -0.0215 \end{bmatrix}\times10^3$	1125.32	$\begin{bmatrix} 48.24 \\ 3.57 \end{bmatrix}$
FBG_1+MMF_3	$\begin{bmatrix} 1.14\times10^{-3} & 0.0126 \\ -0.84\times10^{-3} & 0.0568 \end{bmatrix}$	$\begin{bmatrix} 0.7539 & -0.1673 \\ 0.0112 & 0.0151 \end{bmatrix}\times10^3$	44.96	$\begin{bmatrix} 9.21 \\ 0.26 \end{bmatrix}$

For the combination of FBG_1+MMF_3, the coefficient matrix is listed in Table 3.3. By using Eq. (3.5), the simultaneous measurement of strain and temperature is shown in Fig. 3.11. There are two planes, individually indicating the applied strain and temperature changes. For a given pair wavelength shifts $\Delta\lambda_{FBG}$ and $\Delta\lambda_{MMF}$, the strain and temperature can be determined simultaneously.

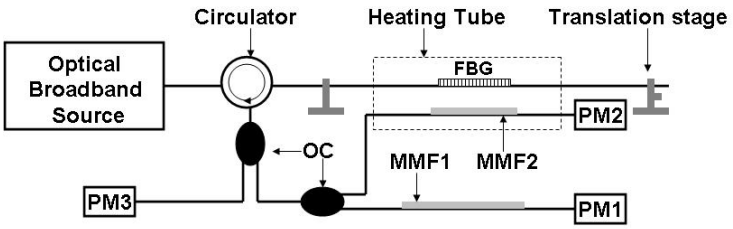

Figure 3.12: Experiment setup using an intensity-based interrogation method. OC: optical coupler; MMF: multimode fiber; PM: power meter.

3.3 MMF Serves as an Edge Filter

An improved all-fiber sensor capable of simultaneous measurement of strain and temperature is presented. The sensor system is formed by an FBG and two sections of MMFs. One section of the MMF is isolated from strain and acts as a temperature-dependent edge filter, while the other is isolated from both strain and temperature changes. By monitoring the optical power changes, it is feasible to obtain information that permits simultaneous measurement of strain and temperature with a low-cost and simple structure.

3.3.1 Operation Principle and Experiment Setup

Fig. 3.12 presents the experiment setup. A broadband source is used to illuminate an FBG via an optical circulator. The FBG is written in standard SMF. The reflected light from the FBG is split into two paths by a 3-dB optical coupler (OC) after passing through the circulator. In one path, the power P_3 is directly measured by a power meter, PM3, as a reference to eliminate any power fluctuation from the optical source and the dependency of the light source intensity on the wavelength [23, 25]; in the other path the light is split again by a second 3-dB OC. The resultant two beams pass through two sections of MMFs, MMF1 and MMF2, and their powers P_1 and P_2 are measured by the other two power meters, PM1 and PM2, respectively. Both the FBG and MMF2 are inserted loosely through a copper tube with a diameter of 1.5 cm, which is wrapped with heating tape. Outside the tube, one side of the fiber on which the FBG is inscribed is attached to a translation stage with a resolution of 10 μm, while MMF2 is isolated from strain. MMF1 is placed outside of the tube, isolated from both strain and temperature. Both of the MMFs, more strictly speaking the SMF-MMF-SMF structures, act as MZIs based on intermodal interference [22]. When the light is coupled into the MMF, many modes are excited, each of which has a different propagation constant. When they recouple back into the SMF after passing through a section of MMF, the modes interfere. Each mode has experienced a different phase shift. If only two dominant modes (LP_{01} and LP_{02}) are excited, the resultant interference fringe

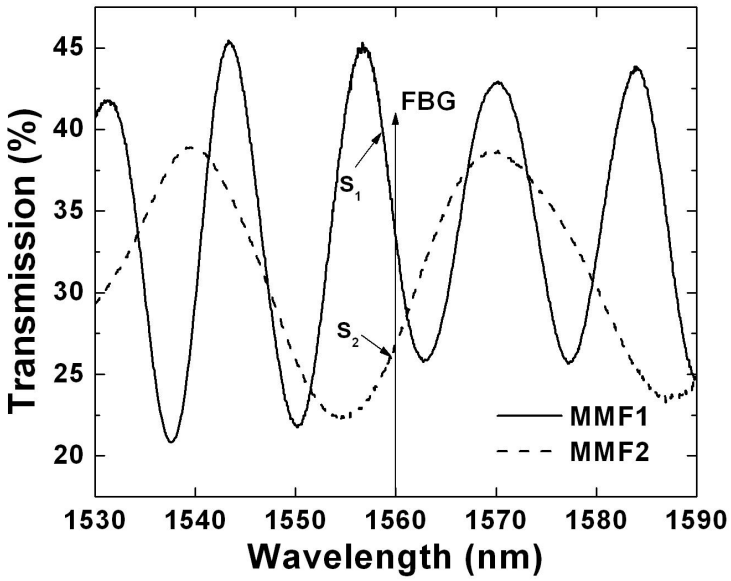

Figure 3.13: Transmission spectra of MMF1 and MMF2.

pattern is approximately sinusoidal with a uniform extinction ratio determined by the ratio of the intensities of the two modes (e.g., the best mode operation is to launch equal power of the two modes). If other higher-order modes are excited, the interference fringe pattern will be modulated by the influences of higher-order modes. The measured transmission spectra of the MMFs are shown in Fig. 3.13. The graded-index MMFs used in our experiment have a numerical aperture (NA) of 0.29 and core/cladding diameters of 100/140 μm. Since Fig. 3.13 shows that the interference fringe pattern is rather uniform, confirming that there are two modes interfering primarily in our case. This is reasonable because higher-order modes usually have less power compared to the lower-order modes. An extinction ratio of approximate 3 dB is achieved, indicating that the power of LP_{02} mode is very low (only 3% of the total power). The fringe contrast could be increased by slightly offsetting the center of core of the MMF with respect to that of the SMF [22]; however, high loss could be introduced. In the present work, a 3-dB extinction ratio is good enough for the sensor operation. The lengths of MMF1 and MMF2 are selected of 70 cm and 30 cm, respectively, so that for both MMFs the approximate middle of the fringe's slope falls on the FBG's central wavelength. All the MMFs and SMFs are fusion spliced directly to avoid drift in the interference spectra due to the possible long-term change in these connections. The FBG has a reflectivity of 84.5%, an optical bandwidth of 0.21 nm, and a center wavelength of 1560.05 nm, which is located in the linear region of the filter spectra of MMF1 and MMF2, with slopes S_1 and S_2, respectively. The slopes can be simply increased by using longer MMFs, but the measurement range would then be reduced, since there is a tradeoff between this range and the sensitivity.

When there is an ambient temperature change ΔT in °C at a fixed strain, the change in power ratio $\Delta(P_1/P_3)$ is given by $\Delta(P_1/P_3) = S_1 K_{T(FBG)} \Delta T$, where $K_{T(FBG)}$ refers to the wavelength shift of the FBG spectrum per °C. We use the ratio of P_1 to the reference power P_3 to eliminate optical source fluctuations. However, for the power ratio change $\Delta(P_2/P_3)$, one has to account for the temperature influence on the MMF2 spectrum, which also has a linear response with respect to temperature change [22]. Thus, the power ratio change can be expressed as $\Delta(P_2/P_3) = S_2[K_{T(FBG)} - K_{T(MMF2)}]\Delta T$, where $K_{T(MMF2)}$ refers to the wavelength shift of the MMF2 spectrum per °C, provided that the slope S_2 remains constant when the temperature changes (see Figs. 14-16 in Section 3.3.2). When the strain is applied to the FBG at constant temperature, the power ratio changes $\Delta(P_1/P_3)$ and $\Delta(P_2/P_3)$ can be simply obtained as $\Delta(P_1/P_3) = S_1 K_{\varepsilon(FBG)} \varepsilon$ and $\Delta(P_2/P_3) = S_2 K_{\varepsilon(FBG)} \varepsilon$, respectively, with ε being the applied strain in $\mu\varepsilon$ (microstrain) and $K_{\varepsilon(FBG)}$ referring to the wavelength shift of the FBG spectrum per $\mu\varepsilon$ of applied strain. The overall power ratio changes can be described as

$$\begin{bmatrix} \Delta(P_1/P_3) \\ \Delta(P_2/P_3) \end{bmatrix} = \begin{bmatrix} \alpha_1 & \beta_1 \\ \alpha_2 & \beta_2 \end{bmatrix} \begin{bmatrix} \varepsilon \\ \Delta T \end{bmatrix}, \tag{3.8}$$

where $\alpha_1 = S_1 K_{\varepsilon(FBG)}$ and $\alpha_2 = S_2 K_{\varepsilon(FBG)}$ are the strain coefficients for $\Delta(P_1/P_3)$ and $\Delta(P_2/P_3)$, respectively, and $\beta_1 = S_1 K_{T(FBG)}$ and $\beta_2 = S_2[K_{T(FBG)} - K_{T(MMF2)}]$ are the corresponding temperature coefficients, which can be determined experimentally. Note that the introduction of the temperature coefficient of MMF2, $K_{T(MMF2)}$, makes the determinant of the coefficient matrix non-zero so that one can invert Eq. (3.8) to discriminate strain and temperature simultaneously from a measurement of the pair of power ratio changes.

3.3.2 Experiment and Discussion

Before measuring the matrix coefficients in Eq. (3.8), it is important to test the operating range of the sensor system first. Generally, the Bragg wavelength shift is ~ 1.2 pm/$\mu\varepsilon$ with the applied strain and ~ 13 pm/°C with the temperature change near 1550 nm. With such a small amount of wavelength shift, the FBG resonance wavelength always falls within the linear region of the MMF1 spectrum for a large strain and temperature range (see Fig. 3.13). However, the MMF2 spectrum also shifts when the temperature changes with a relatively large sensitivity [22]. It is, therefore, necessary to know the operating temperature range within which the Bragg wavelength falls in the linear region of the MMF2 spectrum. Fig. 3.14 shows the shift of the MMF2 transmission spectrum as the temperature increases from room temperature of 24 °C to 80 °C. The sensitivity of the spectrum shift is about -55 pm/°C. In order to examine the slope variations in detail, the spectrum in $1559 - 1562$ nm is also shown in Fig. 3.15. This wavelength range is sufficient,

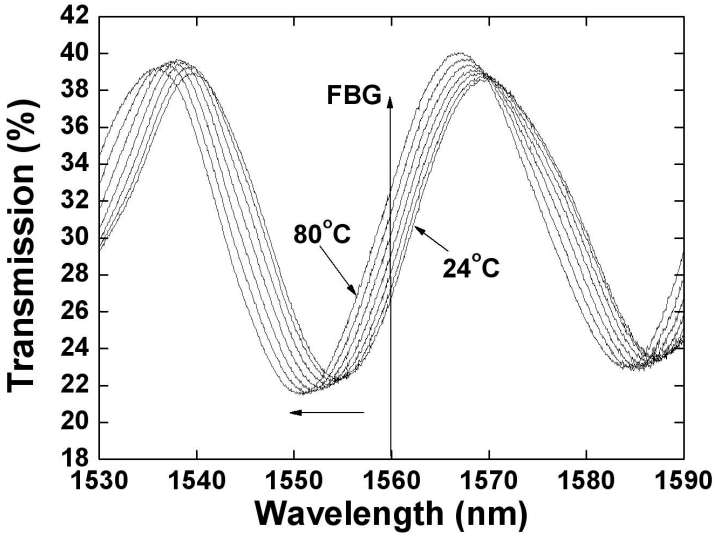

Figure 3.14: Transmission spectra of MMF2 with zero strain at different temperatures from 24 °C to 80 °C in the wavelength range of 1530-1590 nm.

because the Bragg wavelength shift is less than 2 nm in our experiment. Fig. 3.16 gives the slopes of the MMF2 spectrum at different temperatures, showing that the maximum fractional slope change from 24 °C to 80 °C is around 4%. Although this variation could influence the accuracy of our sensor system, it is acceptable according to our experiment results (see Fig. 3.18). In this temperature range, the resonance wavelength of the FBG always falls in the linear region; therefore, the proposed sensor system is expected to operate within a temperature range of about 60 °C. In order to obtain the matrix coefficients in Eq. (3.8), strain and temperature are applied on the sensing head separately within the operating range. We first measure the strain responses of the sensing head by obtaining the power ratio changes as a function of the applied strain at the room temperature of 24 °C, as shown in Fig. 3.17. Figure 3.18 shows the power ratio changes with respect to temperature changes by heating the tube from 24 °C to 80 °C under zero strain. The measured power ratio changes have good linear behavior with variations in strain and temperature. The slope of the two curves in each of Figs. 3.17 and 3.18 are used to extract the values of the two α's and β's shown inside the figure frames. By inverting Eq. (3.8), the strain and temperature can be obtained simultaneously from

$$\begin{bmatrix} \varepsilon \\ \Delta T \end{bmatrix} = \frac{10^3}{3.8} \begin{bmatrix} -108 & -51.26 \\ 2.285 & 4.5782 \end{bmatrix} \begin{bmatrix} \Delta(P_1/P_3) \\ \Delta(P_2/P_3) \end{bmatrix}, \tag{3.9}$$

after the pair of power ratio changes, $\Delta(P_1/P_3)$ and $\Delta(P_2/P_3)$, have been measured. For a given measurement error of the power ratio change of 1%, the estimated resolutions of

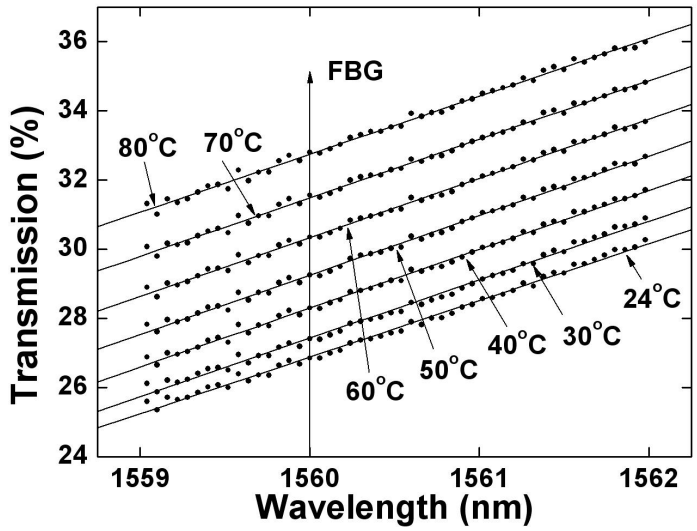

Figure 3.15: Transmission spectra of MMF2 with zero strain at different temperatures from 24 °C to 80 °C in the wavelength range of $1559 - 1562$ nm.

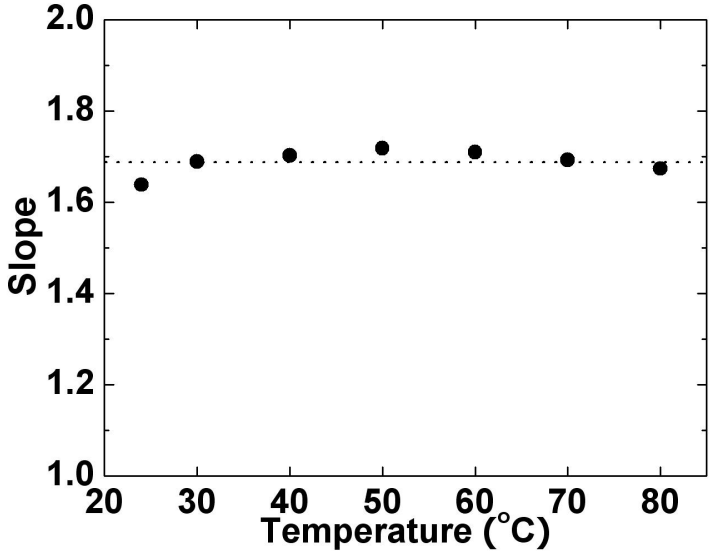

Figure 3.16: The slopes of MMF2 spectrum at different temperatures.

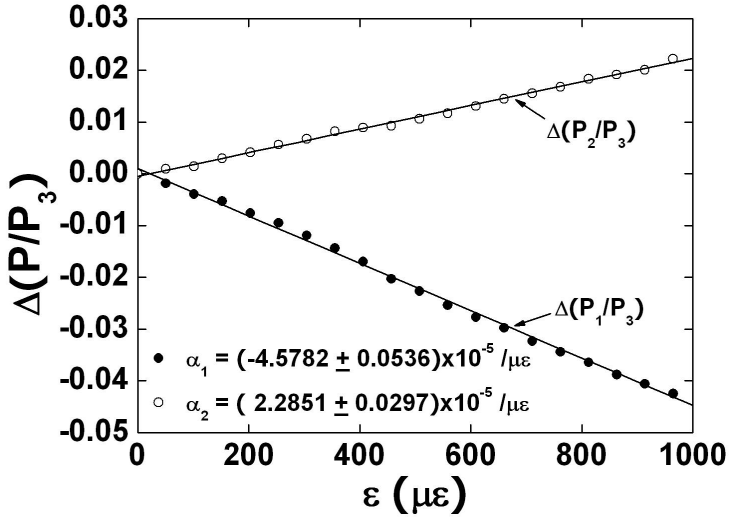

Figure 3.17: Power ratio changes, $\Delta(P_1/P_3)$ and $\Delta(P_2/P_3)$, as a function of applied strain.

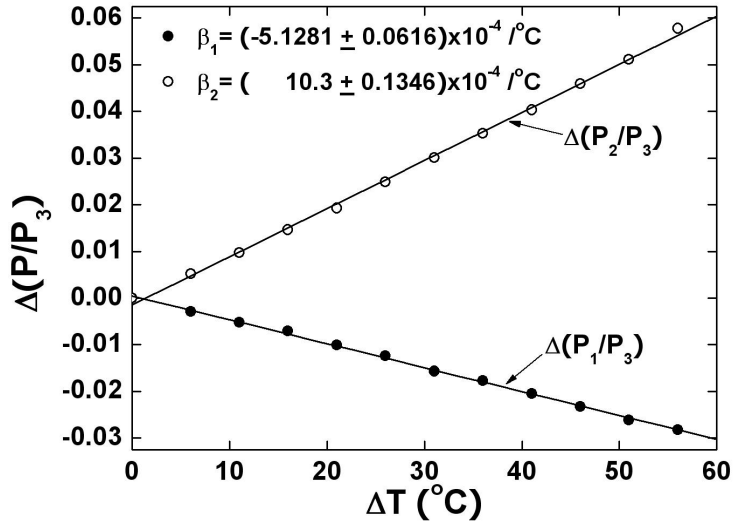

Figure 3.18: Power ratio changes, $\Delta(P_1/P_3)$ and $\Delta(P_2/P_3)$, as a function of temperature change.

the proposed sensor system are about ± 25.8 $\mu\varepsilon$ and ± 1.2 °C [22], over the measurement ranges of 1000 $\mu\varepsilon$ and 60 °C.

3.4 Conclusion

A transmission-type simultaneous strain and temperature sensing technique has been demonstrated based on a combination of an FBG and a section of MMF. The applied strain and ambient temperature changes can be obtained by measuring the wavelength shifts of the FBG and the MMF that acts as an MZI. The measurement resolution is very sensitive to the strain and temperature coefficients of the FBG and MMF and their combination. Since the strain and temperature coefficients of MMFs vary with the fiber core sizes and materials, we demonstrate a good combination of FBG_1+MMF_3 for simultaneous strain and temperature discrimination: 9.21 $\mu\varepsilon$ and 0.26 °C can be achieved for a 10 pm wavelength resolution. However, an OSA has to be used to measure wavelength shifts, which is not practical in "real-world" application.

In order to avoid using OSAs, a new temperature and strain sensor system based on an FBG and two sections of MMFs is described. Simultaneous measurement of strain and temperature can be achieved using an interrogation method based on edge filter techniques. Since the proposed sensor system does not require OSAs or any other sophisticated active demodulation schemes, its cost and complexity are significantly reduced. The resolutions of the proposed sensor system are estimated as ± 25.8 $\mu\varepsilon$ and ± 1.2 °C for an 1% error of the power ratio measurement, which can be attributed to the resolution of the power meters. These figures are comparable to the resolution of most of the grating sensors reported in the literature [14] for simultaneous measurement of strain and temperature. Although some configurations indeed have better performance than the proposed sensor, e.g., 0.7 °C and 15.6 $\mu\varepsilon$ [14], OSAs have to be used to monitor the spectrum shift. Compared to the interrogated grating sensors [23, 24, 25, 26, 27, 28, 29, 30], although very good resolutions of 1 $\mu\varepsilon$ [29]and 0.05 °C [30] can be achieved, the discrimination of these two measurands is not reported. In addition, an MMF filter is simpler, less expensive, and easier to fabricate than the interrogators demonstrated above.

Chapter 4

Simultaneous Measurement of Strain and Temperature with Fiber Bragg Grating and High-Birefringence Fiber Loop Mirrors

4.1 Introduction

Optical fiber sensors have aroused intensive research in recent years because they are compact, light weight, resistant to electromagnetic interference, and easy to be embedded into other structures. Fiber Bragg gratings (FBGs) are good candidates because they have the features of wavelength encoding and multiplexing capability. Since FBGs are sensitive to both temperature and strain, many configurations have been reported to discriminate these two measurands by detecting two physical parameters that have different sensitivities to temperature and strain, such as using two superimposed FBGs [1], two resolvable wavelengths in a tilted FBG [2], inserting an FBG [3] or a long-period fiber grating [4] into a high-birefringence fiber loop mirror (HBFLM). Many other techniques can be found in the review paper [5].

On the other hand, HBFLMs have increasingly aroused research interests in the past several years, because they are stable, flexible, and easy to manufacture. The method of operation of HBFLMs is based on optical multibeam interference between clockwise and counterclockwise beams in the fiber loop. They can be used in optical communications as gain flattening of erbium-doped fiber amplifiers [6], wavelength division multiplexing filters [7], and wavelength filters in multi-wavelength fiber lasers [8]. Recently, there has been considerable interest in developing HBFLM sensors to measure strain [9], temper-

ature [10], and other physical parameters [11, 12]. Special attention has been paid to simultaneous measurement of temperature and strain [4, 13, 14] by using HBFLMs. Different configurations based on HBFLM structure have been proposed and demonstrated for simultaneous strain and temperature discrimination. Sun *et al.* [13] used two different types of high-birefringence fiber (HBF) in series inserted in a fiber loop mirror as a sensing head to produce two wavelength dips with different sensitivities to temperature and strain. Frazão *et al.* [14] presented a configuration using two concatenated HBFLMs with one loop containing a section of photonic crystal fiber, which might increase the cost of the sensor system. In addition, the complexity of the sensing head could limit the applicability of the system. Frazão *et al.* [4] also reported another approach by using a long-period fiber grating (LPG) inserted in an HBFLM. However, it is difficult to accurately measure the center wavelength of the LPG due to its large bandwidth [15]. Additionally, the performance of this configuration may be limited by the poor property of the system's coefficient matrix, which maps the temperature and strain changes to the wavelength shifts of the LPG and HBFLM spectrum. More specifically, the absolute value of the determinant of this matrix is very small, which may introduce significant errors and give low accuracy [3, 5].

In the second section of this chapter, an alternative configuration suitable for strain and temperature discrimination based on an HBFLM combined with an FBG serving as a sensing head is presented. The bandwidth of the FBG is much narrower than that of the LPG. Since the HBFLM has different strain and temperature sensitivity responses from those of the FBG, it is feasible to realize simultaneous measurement of the strain and temperature variations based on their combination. By measuring the resonance wavelength shifts of the HBFLM and the FBG accurately, and constructing a well-conditioned coefficient matrix based on this configuration, the applied strain and temperature changes can be determined simultaneously with high resolution.

Considering that the HBFLMs usually have higher sensitivities of strain and temperature than those of the FBGs, a scheme which could measure strain and temperature simultaneously is introduced in Section 4.3 by space division multiplexing two HBFLMs. Temperature and strain can be discriminatively measured by sequentially monitoring the resonance wavelength shifts of two HBFLMs constructed with the same HBF. Theoretical results show that this scheme can provide high resolutions in temperature and strain. Experimental results show that the temperature and strain resolutions could reach ± 0.5 ^{o}C and ± 10 $\mu\varepsilon$, respectively. Moreover, it is expected to have applications in distributed HBFLM sensing.

Both the above configurations have to use optical spectrum analyzers (OSAs) to monitor the wavelength shifts of the spectrum. OSAs are usually used to obtain spectral information that reflects the responses of the sensing head to temperature and strain, but they are very expensive and have slow scanning speed. Thus, there is considerable interest in developing methods [16, 17, 18, 19, 20, 21, 22, 23] which monitor parameters other than

wavelength information provided by the sensing head. Many passive detection interrogators involving no tracking, scanning, or modulating mechanisms have been reported, such as using linearly wavelength-dependent devices [16, 17, 18, 19], identical chirped grating pairs [20], and charge-coupled device (CCD) spectrometers [21]. For active detection schemes which require more complex systems compared to the passive ones, Fabry-Pérot filter interrogators [22], fiber Fourier transform spectrometer interrogators [23], and many other techniques have also been demonstrated. The most cost-effective method among both the passive and active schemes is to develop an intensity-based interrogation system using a linearly wavelength-dependent optical filter. Sensor systems that adopt this type of demodulator have been commercialized. By adopting suitable interrogators, the optical fiber sensor systems become more compact, cost-effective and competitive. However, note that most reports on simultaneous measurement of temperature and strain have to use OSAs to monitor wavelength shifts which may limit their practical applications [5].

In Section 4.4, an all-fiber sensor configuration that is feasible to measure temperature and strain simultaneously using an FBG and two HBFLMs is demonstrated. For the configuration that an FBG is inserted into an HBFLM, an OSA has to be used to monitor the wavelength shift of both the FBG and HBFLM. In the present sensor system, the two HBFLMs act as two interrogators with one of them dependent on both temperature and strain. By monitoring power changes instead of wavelength shifts, simultaneous strain and temperature could be achieved with a low cost and high speed. Note that simultaneous measurement of these two measurands could also be achieved without an OSA by using two sections of multimode fibers as presented in Section 3.3, but the HBFLMs could be found to have higher sensitivities than those of the multimode fiber interferometers.

4.2 An FBG Inserts inside an HBFLM

An all-fiber sensor for simultaneous measurement of temperature and strain is presented. The sensing head is formed by introducing an FBG into an HBFLM that acts as a Mach-Zehnder interferometer (MZI) for temperature and strain discrimination. The sensing head is rather simple, which only consists two section of optical fibers, an FBG and a section of HBF. However, in order to extract the information from the sensing head, OSAs have to be used, which makes the system expensive and have a slow scanning speed. In Section 4.4, an improved design will eliminate these drawbacks by measuring the optical power changes instead of the wavelength shifts.

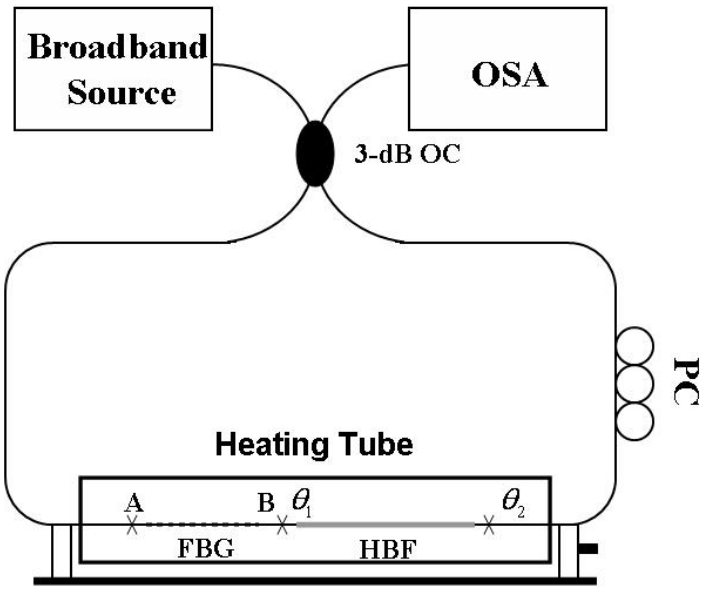

Figure 4.1: Experiment setup: An FBG inserted inside a HBFLM. ×: the spliced point.

4.2.1 Operation Principle and Experiment Setup

Our experiment setup is shown in Fig. 4.1. A fiber loop mirror is formed by a 3-dB optical coupler (OC), a polarization controller (PC), an FBG and a section of HBF. The FBG is written in SMF-28. The fiber loop mirror acts like a bandpass filter for the input signal. The input light is split into two beams propagating clockwisely and counterclockwisely by means of the 3-dB coupler. Each of the resultant beams is decomposed into two beams after it travels through the HBF. The PC changes the polarization states of both the clockwise and counterclockwise beams. The counterpropagating beams recombine at the coupler and exhibit interference due to the phase difference. The transmission spectrum of the HBFLM is approximately a periodic function of the inverse wavelength as follows:

$$T(\lambda) = [\sin(\theta_1 + \theta_2) \cos\left(\frac{\pi BL}{\lambda}\right)]^2, \tag{4.1}$$

where θ_1 and θ_2 are the angles between the light at both ends of the HBF and the fast or slow axis of the HBF, respectively; and B, L and λ are the birefringence, the length of HBF and the operation wavelength, respectively. Thus, the loop filter characteristic is similar to an MZI and can be used as a sensor. The free spectral range (FSR) of the HBFLM filter can be given by Eq. (4.1) as:

$$FSR \approx \frac{\lambda^2}{BL}. \tag{4.2}$$

For the light whose wavelength is falling inside the forbidden band of the FBG, the counterpropagating beams will both be reflected at points A and B back to the coupler by the FBG. By properly adjusting the PC, the resultant FBG spectrum can be superimposed on the HBFLM spectrum. When a strain is applied to the HBF and FBG or when there is an ambient temperature change, the birefringence, the fiber length and the grating pitch will change, and therefore the resonance wavelengths will shift. The shifts of the resonance wavelengths for the FBG and the HBFLM can be expressed as:

$$\begin{bmatrix} \Delta\lambda_{FBG} \\ \Delta\lambda_{HBFLM} \end{bmatrix} = \begin{bmatrix} K_{T(FBG)} & K_{\varepsilon(FBG)} \\ K_{T(HBFLM)} & K_{\varepsilon(HBFLM)} \end{bmatrix} \begin{bmatrix} \Delta T \\ \varepsilon \end{bmatrix}, \tag{4.3}$$

where $\Delta\lambda_{FBG}$ and $\Delta\lambda_{HBFLM}$ are FBG and HBFLM wavelength shifts in nanometers; ΔT and ε are ambient temperature change in ^{o}C and applied strain in $\mu\varepsilon$, respectively; and $K_{T(FBG)}$, $K_{\varepsilon(FBG)}$, $K_{T(HBFLM)}$ and $K_{\varepsilon(HBFLM)}$ are the corresponding temperature and strain coefficients which can be determined from the experiment. The temperature change and the applied strain can then be simultaneously obtained from Eq. (4.3):

$$\begin{bmatrix} \Delta T \\ \varepsilon \end{bmatrix} = \frac{1}{D} \begin{bmatrix} K_{\varepsilon(HBFLM)} & -K_{\varepsilon(FBG)} \\ -K_{T(HBFLM)} & K_{T(FBG)} \end{bmatrix} \begin{bmatrix} \Delta\lambda_{FBG} \\ \Delta\lambda_{HBFLM} \end{bmatrix}, \tag{4.4}$$

with

$$D = K_{T(FBG)}K_{\varepsilon(HBFLM)} - K_{T(HBFLM)}K_{\varepsilon(FBG)}, \tag{4.5}$$

being the determinant of the coefficient matrix. For optical sensing devices, the sensing resolution is one of the key performance parameters. The most obvious form of the errors is attributed to the inaccuracies in measuring the wavelength. For given wavelength measurement errors $\delta(\Delta\lambda_{FBG})$ and $\delta(\Delta\lambda_{HBFLM})$, the tolerances of the measured temperature $\delta(\Delta T)$ and strain $\delta(\varepsilon)$ are given by [24]:

$$\begin{bmatrix} \delta(\Delta T) \\ \delta(\varepsilon) \end{bmatrix} = \pm\frac{1}{|D|} \begin{bmatrix} \left|K_{\varepsilon(HBFLM)}\right| & \left|K_{\varepsilon(FBG)}\right| \\ \left|K_{T(HBFLM)}\right| & \left|K_{T(FBG)}\right| \end{bmatrix} \begin{bmatrix} |\delta(\Delta\lambda_{FBG})| \\ |\delta(\Delta\lambda_{HBFLM})| \end{bmatrix}. \tag{4.6}$$

The wavelength measurement errors are determined by the resolution of the OSA and the bandwidth of the FBG and HBFLM resonance. To obtain a high sensing resolution, it is preferable to have a large absolute value of the determinant of the coefficient matrix, $|D|$. Obviously, this could be achieved when the two terms in Eq. (4.5), $K_{T(FBG)}K_{\varepsilon(HBFLM)}$ and $K_{T(HBFLM)}K_{\varepsilon(FBG)}$, have different signs. This feature is extremely important if the absolute values of these two terms are very close to each other, as can be seen from the example listed in Table 4.1 (see Section 4.2.2). This suggests that when using the combination of two types of fiber-based elements with similar sensitivities as a sensing head for simultaneous measurement of temperature and strain, it is desirable to choose the two elements with opposing trends in one type of measurement (e.g. strain) and similar but distinct trends in the other type of the measurement (e.g. temperature) [3]. In addition, Eq. (4.6) also provides us an effective way to compare two different schemes which are performed under different experimental conditions.

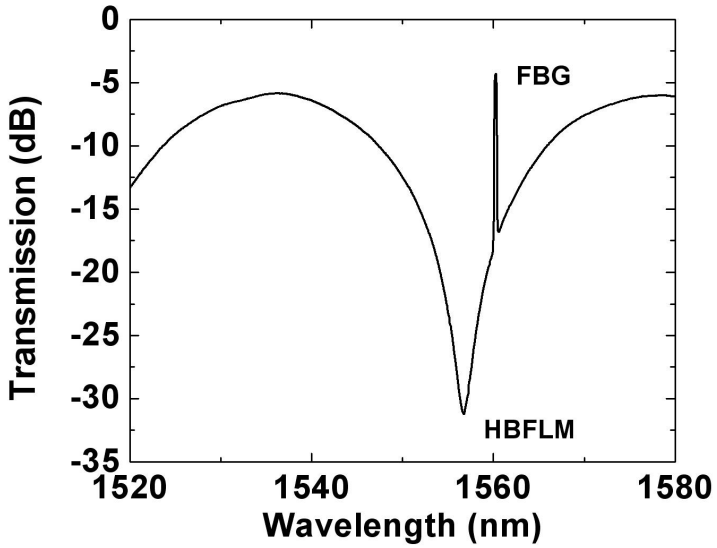

Figure 4.2: Transmission spectrum of the FBG and HBFLM at zero strain and room temperature (22.3 °C).

4.2.2 Experiment and Discussion

The experiment setup shown in Fig. 4.1 consists of an optical broadband source, an OSA with a resolution of 0.06 nm, and a fiber loop mirror formed by a 3-dB OC, a PC, an FBG and a section of HBF. The sensing head (FBG and HBF) is placed in a copper tube with a diameter of 1.5 cm, which is wrapped by a heating tape. One side of the fiber is attached to a translation stage with a resolution of 10 μm. The FBG has a center wavelength of 1560.05 nm with 84.5% reflectivity and optical bandwidth of 0.21 nm. The HBF (Bow-Tie style) is a polarization-maintaining single mode optical fiber for the wavelength of 1550 nm with a beat length of 2.0 mm at 633 nm and an attenuation of 2 dB/km. The transmission spectrum at room temperature (22.3 °C) with zero strain is shown in Fig. 4.2. The FBG spectrum is superimposed on the spectrum of the HBFLM. The ambient temperature change and the applied strain can be determined by measuring the resonance wavelength shifts of the FBG and HBFLM. To determine the temperature and strain coefficients of the FBG and HBFLM, temperature change and strain are applied to the fiber separately. The length of HBF is approximately 12 cm, resulting in a wavelength spacing of approximately 44 nm giving a birefringence of $\approx 4.55 \times 10^{-4}$ at 1550 nm by Eq. (4.2). This value is determined from requiring the HBFLM spectrum to produce two minima in order to have broader temperature and strain range. In Fig. 4.3, we indicate the transmission spectrum at 40 °C with zero strain, where the second minimum of the HBFLM spectrum has appeared on the right, while the minimum appeared at room temperature

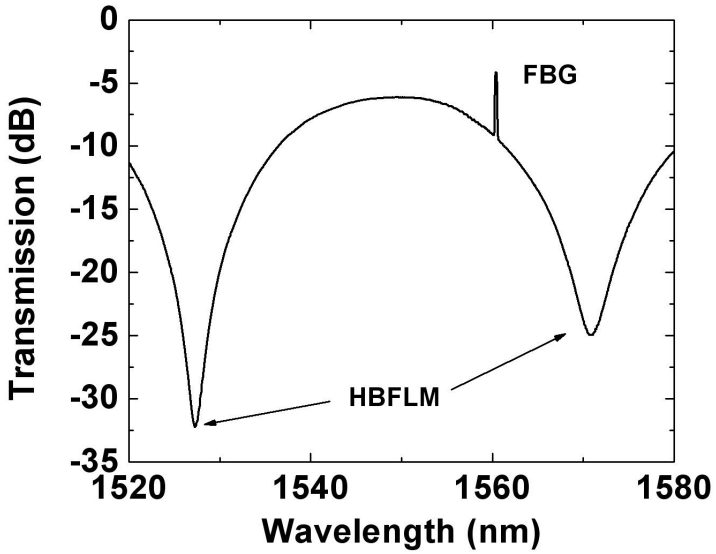

Figure 4.3: Transmission spectrum of the FBG and HBFLM at zero strain and room temperature (40 °C) showing two minima.

in Fig. 4.2 has moved to the left. As the temperature is increasing above 40 °C, we begin to use the second minimum as a reference, realizing a broader temperature testing range. From Eq. (4.1), the resonance wavelength must fulfill the relation $BL = g_r\lambda_r$ with g_r being a positive half-integer and λ_r being the corresponding resonance wavelength. The temperature or strain sensitivity of each resonance wavelength is proportional to $1/g_r$ [11], which is the only factor responsible for the sensitivity difference between different resonance wavelengths when the birefringence is assumed to be the same in the operation wavelength range. Since g_r has a value of about 35.5 evaluated at the 1550-nm wavelength band with the parameters of the HBF used in our experiment, it is acceptable to ignore the sensitivity difference between the first ($\propto 1/g_r$) and the second ($\propto 1/(g_r - 1)$) minimum in our case where the percent difference is less than 3%. We first obtain the strain responses of the FBG and HBFLM, shown in Fig. 4.4, by measuring the wavelength shifts as a function of the applied strain at room temperature of 22.3 °C. Fig. 4.5 shows the wavelength shifts of the FBG and HBFLM as a function of temperature when the tube is heated from 22.3 °C to 80 °C under zero strain. The measured wavelength shifts are observed to vary linearly with strain and temperature. The negative temperature response is due to the strong effect arising from the birefringence change, which decreases with the increase of the temperature. From these measurements, we obtain the coefficient matrix for the FBG+HBFLM set-up which is given in Table 4.1.

For given measurement errors of wavelength shifts, the errors in strain and temperature are given by Eq. (4.6). Since the performance comparison of different schemes should

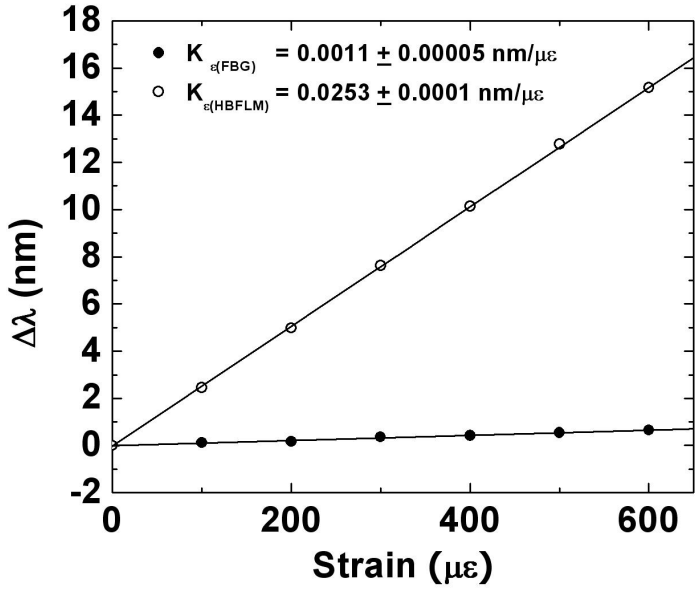

Figure 4.4: Wavelength shifts as a function of applied strain.

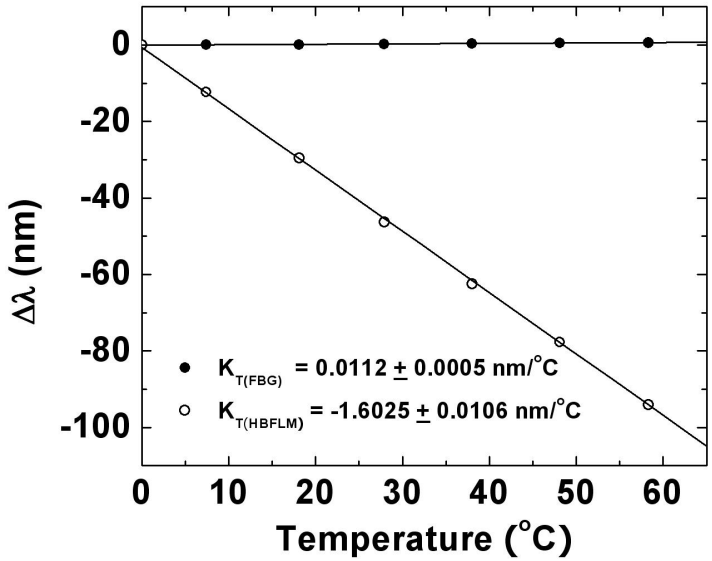

Figure 4.5: Wavelength shifts as a function of ambient temperature.

Table 4.1: The coefficient matrices and the corresponding resolutions of strain and temperature for the combination of FBG+HBFLM and of LPG+HBFLM in Ref. [4]

Combinations of sensor head	Coefficient matrix	Inversed coefficient matrix	Resolutions of $\begin{bmatrix} temperature(^oC) \\ strain(\mu\varepsilon) \end{bmatrix}$
FBG+HBFLM	$\begin{bmatrix} 0.0112 & 0.0011 \\ -1.6025 & 0.0253 \end{bmatrix}$	$\frac{1}{0.2046}\begin{bmatrix} 2.53 & -0.11 \\ 160.25 & 1.12 \end{bmatrix}$	$\begin{bmatrix} 0.77 \\ 47.32 \end{bmatrix}$
LPG+HBFLM	$\begin{bmatrix} 0.085 & -0.0043 \\ -0.55 & 0.0298 \end{bmatrix}$	$\frac{1}{0.0168}\begin{bmatrix} 2.98 & 0.43 \\ 55.0 & 8.5 \end{bmatrix}$	$\begin{bmatrix} 12.18 \\ 226.79 \end{bmatrix}$

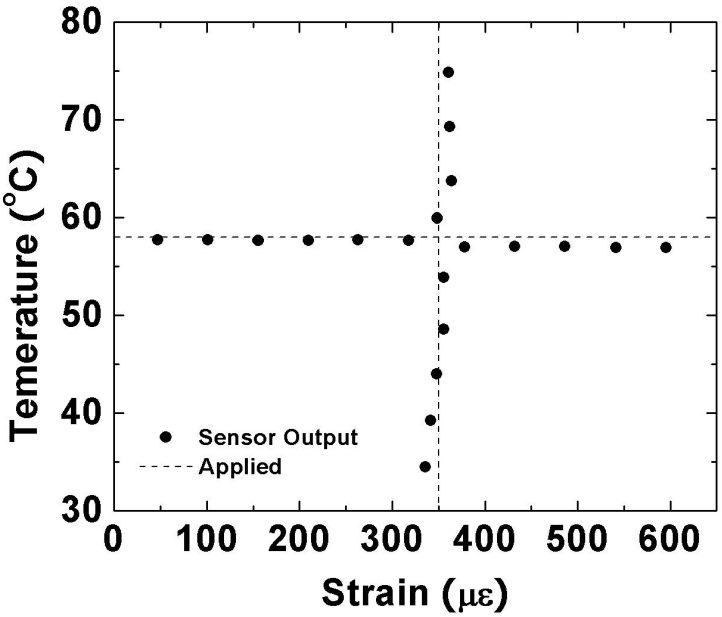

Figure 4.6: Sensor output obtained by Eq. (4.4) for the applied strain at a fixed temperature of 58 °C and temperature variations under a constant strain of 350 $\mu\varepsilon$, respectively.

be made under the same experiment conditions which cannot be guaranteed when the experiments are reported by different groups, these theoretical calculations provide us an effective way by assuming each configuration has the same measurement error. Assuming a wavelength shift measurement error of 0.06 nm for both the FBG and HBFLM and using Eq. (4.6), we calculate the corresponding resolutions of the proposed FBG+HBFLM configuration (see Table 4.1), which can be compared with those of the LPG+HBFLM configuration of Ref. [4]. Clearly, due to its smaller absolute value of the determinant $|D|$, the latter scheme results in a poorer performance. However, the performance of the system in Ref. [4] could be improved by choosing another kind of HBF, such as an elliptical core fiber; the HBFLM spectrum based on this type of HBF has a blue shift for both temperature and strain measurements.

For the proposed combination of FBG+HBFLM, we also investigate its performance experimentally by applying strain variations at a fixed temperature of 58 °C, and tem-

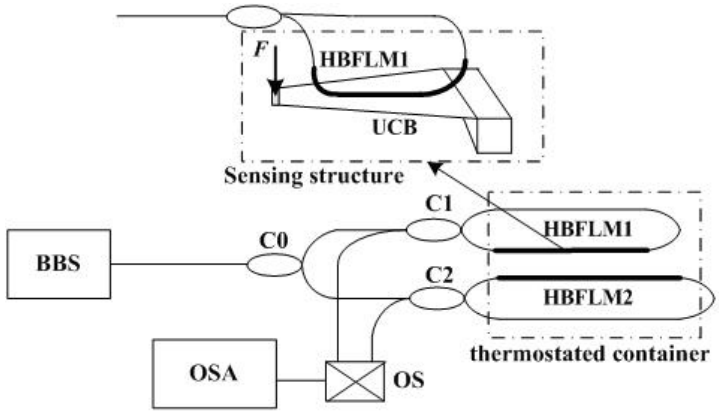

Figure 4.7: SDM HBFLM sensing structure (inset shows the strain sensing structure).

perature variations under a constant strain of 350 $\mu\varepsilon$, respectively. From the pairs of the measured FBG and HBFLM wavelength shifts and using Eq. (4.4), we obtained the corresponding sensor outputs shown in Fig. 4.6. Maximum errors are found to be around ± 1 ^{o}C in temperature and ± 21 $\mu\varepsilon$ in strain. This resolution is different from the calculated results of Table 4.1 due to the finite accuracy of the devices, such as the OSA, heating tube and the translation stage.

4.3 Space Division Multiplex HBFLMs

An alternative fiber sensor scheme for discriminative measurement of temperature and strain by space division multiplexing HBFLMs is presented. Discriminative measurement of strain and temperature can be realized by sequentially measuring the resonance wavelength shifts of two HBFLMs constructed with the same HBF. This scheme can provide not only high resolutions in temperature and strain but also has potential applications in distributed HBFLM sensing.

4.3.1 Operation Principle

Fig. 4.7 shows the space division multiplexing (SDM) HBFLM sensing structure. Two 3-dB couplers of C1 and C2 are used to construct HBFLM1 and HBFLM2, respectively. The emitted light of a broadband source (BBS) couples into HBFLM1 and HBFLM2 through another 3-dB coupler (C0), and the transmitted lights from HBFLM1 and HBFLM2 are monitored by an OSA through a 1×2 optical switch (OS). The switch time of the OS is only a few milliseconds. The HBFLM is formed by a fused coupler with one section of

HBF between its one-sided coupling arms and has similar filter characteristic to an MZI. The resonance condition can be given by

$$\frac{\pi l B}{\lambda} = \frac{N\pi}{2}, \tag{4.7}$$

where N is an integer, l is the length of the HBF, λ is the operation wavelength, and $B = n_0 - n_e$ is the birefringence with n_0 and n_e being the refractive indices of the ordinary (o) and extraordinary (e) light, respectively.

When ambient temperature change ΔT or axial strain ε is applied to the HBF, the birefringence and the fiber length will change accordingly. Thus, the interference spectrum will have a wavelength shift, which can be expressed as $\frac{\Delta\lambda}{\lambda} \approx (\alpha+\xi)\Delta T$ and $\frac{\Delta\lambda}{\lambda} \approx (1+p_e)\varepsilon$, where

$$\alpha = \frac{1}{l}\frac{\partial l}{\partial T}, \tag{4.8}$$

$$\xi = \frac{1}{B}\frac{\partial B}{\partial T}, \tag{4.9}$$

$$p_e = \frac{1}{B}\frac{\partial B}{\partial \varepsilon}, \tag{4.10}$$

are the thermal expansion, effective thermo-optic, and effective strain-optic coefficients of the HBF.

In our experiment, the strain ε is applied by bonding part of the HBF with a length of l_e in an HBFLM to a uniform cantilever beam (UCB). The corresponding strain induced by the force F applied to the end of the beam can be expressed as

$$\varepsilon = \frac{6Ll_e}{Ebh^2 l}F, \tag{4.11}$$

where L, h, b and E are the length, thickness, width at the fixed end, and Young's modulus of the beam, respectively. Both the HBFs are put into a thermostated container, with part of the HBF in HBFLM1 attaching to the UCB and the HBF in HBFLM2 isolating from strain. The measurement coefficient matrix of temperature and strain can be expressed as

$$\begin{pmatrix} \Delta\lambda_1 \\ \Delta\lambda_2 \end{pmatrix} = \begin{pmatrix} K_{T1} & K_{\varepsilon 1} \\ K_{T2} & 0 \end{pmatrix} \begin{pmatrix} \Delta T \\ \varepsilon \end{pmatrix}, \tag{4.12}$$

where

$$K_{T1} = (\alpha + \frac{kl_e}{l}\beta + \xi)\lambda_1, \tag{4.13}$$

$$K_{\varepsilon 1} = (1 + p_e)\lambda_1, \tag{4.14}$$

$$K_{T2} = (\alpha + \xi)\lambda_2, \tag{4.15}$$

are the corresponding temperature and strain coefficients. β is the thermal expansion coefficient induced by the beam material and bonding material, and k is a coefficient related to the bonding quality of the HBF; λ_1 and λ_2 are the measured wavelengths for HBFLM1 and HBFLM2; $\Delta\lambda_1$ and $\Delta\lambda_2$ are HBFLM1 and HBFLM2 wavelength shifts in nanometers; ΔT and ε are ambient temperature change in °C and applied strain in $\mu\varepsilon$, respectively.

The sensing resolution is one of the key performance parameters for the optical fiber sensors. For given wavelength measurement errors of $\delta(\Delta\lambda_1)$ and $\delta(\Delta\lambda_2)$, the tolerances of the measured temperature $\delta(\Delta T)$ and strain $\delta(\Delta\varepsilon)$ can be expressed as

$$\begin{pmatrix} \delta(\Delta T) \\ \delta(\varepsilon) \end{pmatrix} = \pm\frac{1}{|D|}\begin{pmatrix} 0 & |K_{\varepsilon 1}| \\ |K_{T2}| & |K_{T1}| \end{pmatrix}\begin{pmatrix} |\delta(\Delta\lambda_1)| \\ |\delta(\Delta\lambda_2)| \end{pmatrix}, \tag{4.16}$$

where

$$D = -K_{\varepsilon 1}K_{T2}. \tag{4.17}$$

The wavelength measurement errors are determined by the resolution of the OSA and the bandwidth of the HBFLM resonance. It can be seen that large absolute value of the determinant D of the coefficient matrix leads to high resolutions in temperature and strain.

4.3.2 Experiment Results and Discussions

The lengths of the HBF constructing the HBFLM1 and HBFLM2 are about 15.3 and 16.2 cm, respectively. The HBF is a PANDA polarization-maintaining fiber with a beat length of 3.1 mm at 1550 nm and the birefringence of about 6.69×10^{-4}. In order to obtain stable and compact sensing heads, the HBFs are spliced to single-mode fibers (SMFs) at a fixed polarization angle without PCs inserted in the HBFLMs. Part of the HBF (about 5.8 cm) in HBFLM1 is attached to the centric surface of a UCB made up of acrylic glass with Young's modulus of 2700 MPa. The length, thickness and width of the UCB are 12.7, 0.35, and 1.5 cm, respectively. The sensing heads are placed in a thermostated container which is used to control the temperature. With the increase of the temperature, both the transmission spectra of the HBFLM1 and HBFLM2 have blue shifts, as shown in Figs. 4.8 and 4.9.

To obtain the matrix coefficients in Eq. (4.12), we first measure the wavelength shifts of both HBFLM1 (under the strain of 0 and 114 $\mu\varepsilon$) and HBFLM2 (under the strain of 0) with respect to the temperature variation as shown in Fig. 4.10. Experimental results show that there is a good linear relationship between the temperature and the wavelength shift when the temperature varies from 40 °C to 80 °C. When the applied strains are 0 and 114 $\mu\varepsilon$ for HBFLM1, the temperature sensitivities are -0.7832 nm/°C and -0.7782 nm/°C, respectively. The temperature coefficient K_{T1} is about -0.78 nm/°C

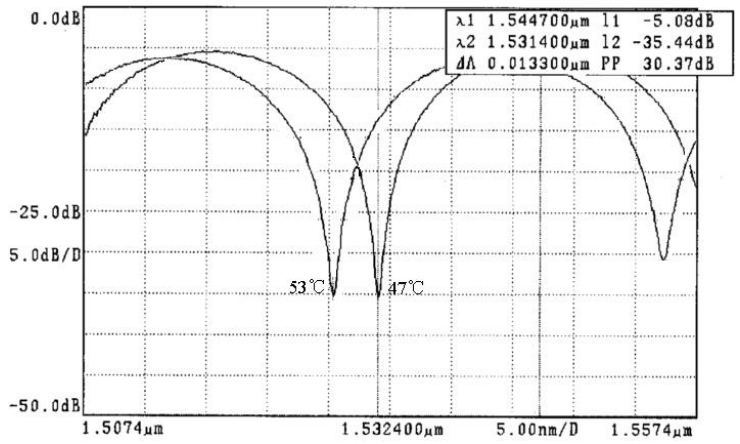

Figure 4.8: Transmission spectra of the HBFLM1 at different temperatures under zero strain.

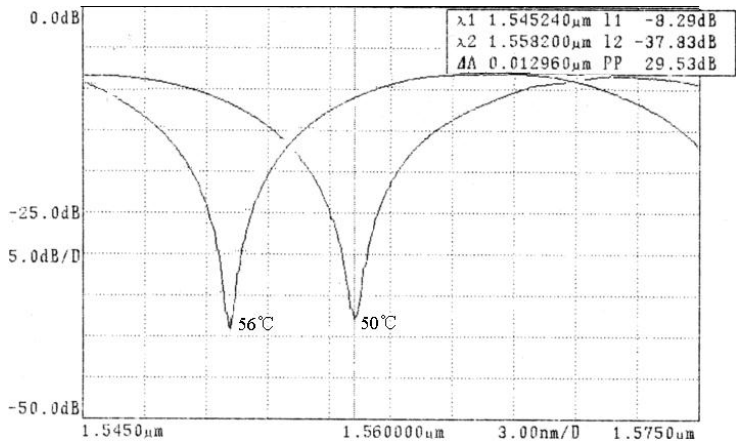

Figure 4.9: Transmission spectra of the HBFLM2 at different temperatures under zero strain.

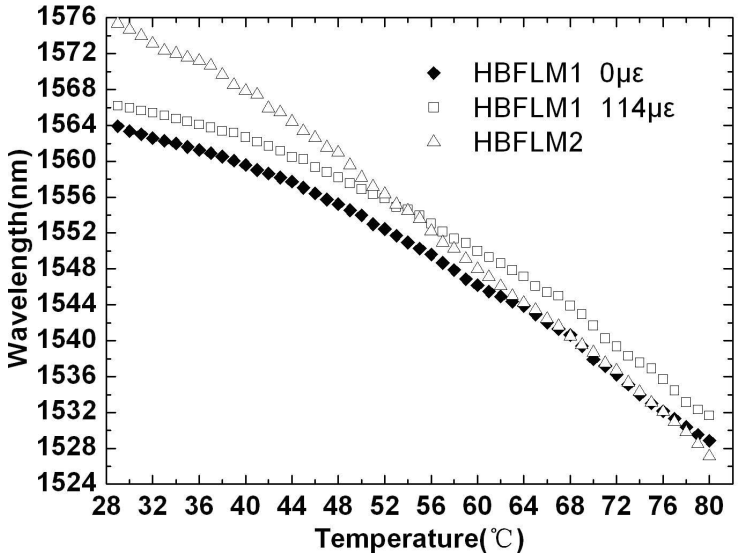

Figure 4.10: Characteristics of HBFLM1 and HBFLM2 transmission spectra versus temperature.

at different strains for HBFLM1 with a fluctuation of less than 2%. Within the temperature range of 40 °C to 80 °C, the temperature sensitivity of HBFLM2 is -1.01 nm/°C. The negative temperature response and high sensitivity are mainly related to the large negative thermo-optic coefficient of the HBF, since the thermal expansion coefficient is generally two orders of magnitude smaller than the thermo-optic coefficient for the optical fiber. If we ignore the thermal expansion coefficient, the thermo-optic coefficient of the HBF used in our experiment is about -6.4×10^{-4} which is much larger than that of the FBG of about 7.1×10^{-6} used in Ref. [15, 25]. It can be seen that the temperature sensitivity of HBFLM2 is larger than that of HBFLM1, which attributes to positive temperature compensation of the beam material and bonding material to the HBF in HBFLM1.

We next measure the wavelength shifts of HBFLM1 spectrum with respect to the applied strain at different temperatures. As shown in Fig. 4.11, the strain sensitivities are 0.01358 nm/$\mu\varepsilon$ and 0.01365 nm/$\mu\varepsilon$ under the temperatures of 27 °C and 50 °C, respectively. Within the strain range of $0-627$ $\mu\varepsilon$, the strain coefficient $K_{\varepsilon 1}$ is about 0.01362 nm/$\mu\varepsilon$ at different temperatures for HBFLM1 with a fluctuation of less than 1%. The fluctuation can be reduced by improving the bonding quality. According to the above experimental results, the measurement coefficient matrix can be achieved as

$$\begin{pmatrix} \Delta\lambda_1 \\ \Delta\lambda_2 \end{pmatrix} = \begin{pmatrix} -0.78 & 0.01362 \\ -1.01 & 0 \end{pmatrix} \begin{pmatrix} \Delta T \\ \varepsilon \end{pmatrix}. \tag{4.18}$$

To compare the performance of this sensing scheme with other schemes [4, 25], assuming

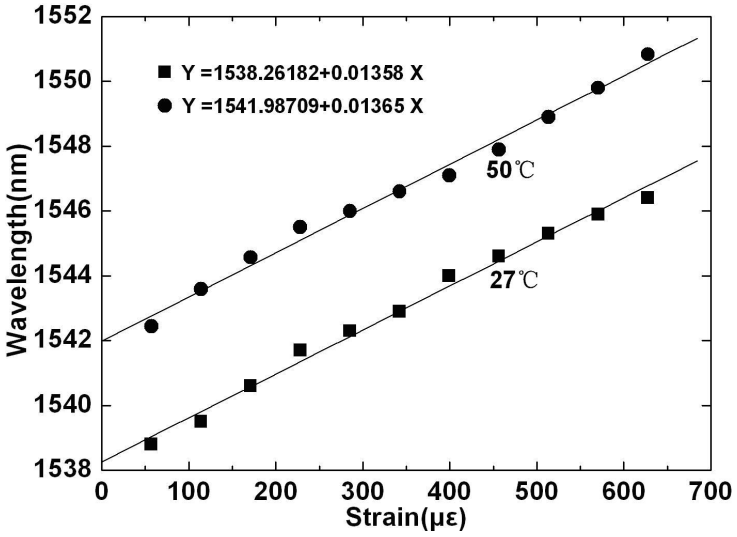

Figure 4.11: Relationship between the strain and the wavelength of HBFLM1 at different temperatures.

a wavelength shift measurement error of 0.06 nm for the HBFLMs, the calculated corresponding temperature and strain resolutions reaches 0.06 °C and 7.8 $\mu\varepsilon$ according to Eq. (4.16). It can be seen that these calculated resolutions are better than those presented in Ref. [4, 25] due to a relative large absolute value of the determinant D.

As the temperature increases from 40 °C to 50 °C, the measured resonance wavelength of HBFLM1 under the strain of 114 $\mu\varepsilon$ changes from 1562.7 nm to 1556.88 nm, while that of HBFLM2 changes from 1567.86 nm to 1558.2 nm, as shown in Fig. 4.10. According to Eq. (4.18), the calculated values of temperature variation and the applied strain are 9.56 °C and 122 $\mu\varepsilon$, respectively, which match the applied values of temperature variation of 10 °C and strain of 114 $\mu\varepsilon$ very well. Repeated experimental results show that the maximum errors are found to be around ± 0.5 °C in temperature and ± 10 $\mu\varepsilon$ in strain. The resolutions are different from the calculated results of 0.06 °C and 7.8 $\mu\varepsilon$ due to the finite accuracy of the experimental devices, such as the OSA, the UCB and the thermostated container.

When using HBFLM1 to measure strain on the cantilever beam, there is a cross sensitivity to temperature depending upon beam material, bonding material, bonding quality, etc. It can be seen that the wavelength shifts with respect to temperature change turn out to be slightly nonlinear as temperature increases from 27 °C to 40 °C shown in Fig. 4.10 due to the above cross effect. It should also be noted that when the temperature is over 80 °C, the wavelength changes abnormally, which is limited by the thermal property of the beam material and bonding material. Higher stable thermal materials can be used to reduce this limitation. The SDM number of the HBFLMs can be increased by employing

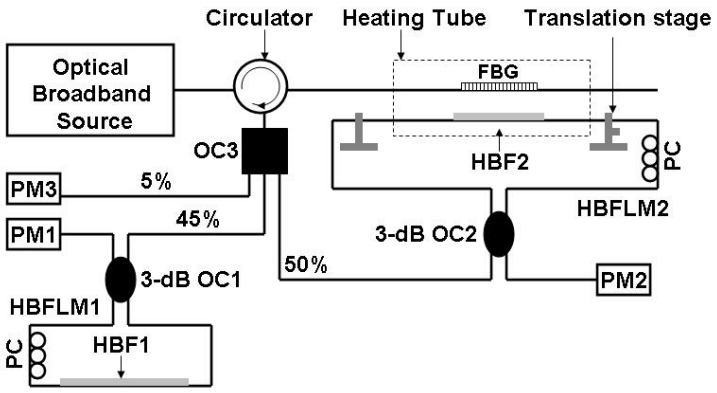

Figure 4.12: Experiment setup using an intensity-based interrogation method with HBFLM as edge filters.

multichannel coupler and OS. In order to reduce the cost of the SDM sensing system, optical intensity-referenced interrogation method can be applied.

4.4 HBFLM Serves as an Edge Filter

Similar to the case where Multimode fiber (MMF) serves as an edge filter, HBFLM could also be used as an edge filter to improve the sensing scheme. Although compared to MMF edge filter, HBFLM is more complicated and expensive, it has higher sensitivity. In this section, we will introduce the edge filter made from an HBFLM, and demonstrate its application for temperature and strain discrimination.

4.4.1 Experiment Setup and Operation Principle

Fig. 4.12 shows the experiment setup. An FBG is illuminated by an optical broadband source via an optical circulator. The FBG is written in standard SMF, with a center wavelength of 1555.7 nm, an optical bandwidth of about 0.2 nm, and a reflectivity of about 99%. The reflected light from the FBG is split into three passes by a 3×1 optical coupler (OC3) after passing through the circulator. In one path from the 5% OC3 port, the power P3 is measured by a power meter, PM3, as a reference to eliminate any power fluctuation from the optical source and the dependency of the light source intensity on the wavelength. In the other two paths, the two beams from the 45% and 50% OC3 ports, pass through HBFLM1 and HBFLM2, and their powers P1 and P2 are measured by the other two power meters, PM1 and PM2, respectively. Each HBFLM is formed by a 3-dB OC,

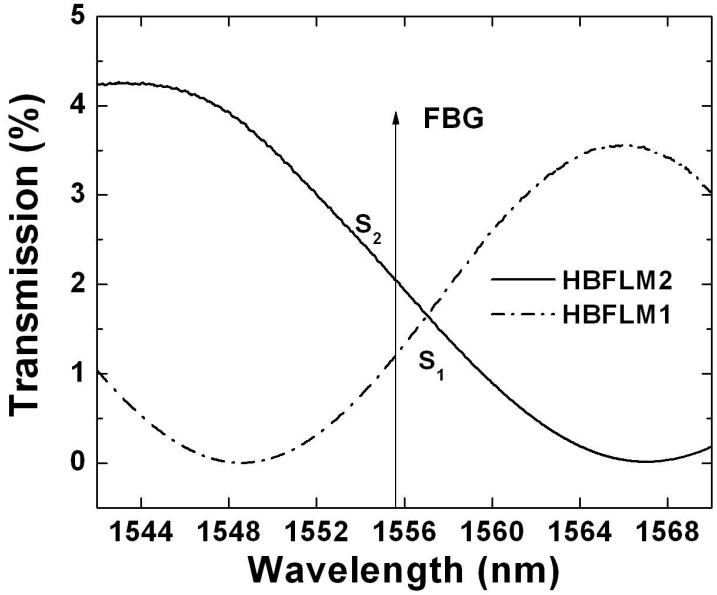

Figure 4.13: Transmission spectra of the HBFLMs.

a PC, and a section of HBF. Both the FBG and HBF2 are inserted loosely into a copper tube with a diameter of 1.5 cm which is wrapped by a heating tape. Outside the tube, one side of the fiber in HBFLM2 is attached to a translation stage with a resolution of 10 $\mu\varepsilon$, while FBG is isolated from strain. HBF1 is placed outside the tube, isolated from both strain and temperature.

Fig. 4.13 shows the transmission spectra of the two HBFLMs. The HBFs are an elliptical core polarization-maintaining single-mode optical fiber operating at 1550 nm with a birefringence of 1.5×10^{-4}. The lengths of HBF1 and HBF2 are 24 cm and 16 cm. By adjusting the PCs, the Bragg wavelength falls in the linear region of the HBFLMs' spectra with slopes of S_1 and S_2, respectively. When there is an ambient temperature change ΔT in degree Celsius at a fixed strain, the power ratio change $\Delta(P_1/P_3)$ can be given as $\Delta(P_1/P_3) = S_1 K_{T(FBG)} \Delta T$, where $K_{T(FBG)}$ refers to the wavelength shift of the FBG spectrum per degree Celsius. However, for the power ratio change $\Delta(P_2/P_3)$, one has to account the temperature influence on HBFLM2 spectrum, which also has a linear response with respect to temperature change [25]. Thus, the power ratio change can be expressed as $\Delta(P_1/P_3) = S_2[K_{T(FBG)} - K_{T(HBFLM2)}]\Delta T$ where $K_{T(HBFLM2)}$ refers to the wavelength shift of the HBFLM2 spectrum per degree Celsius, provided that the slope S_2 of the HBFLM2 spectrum remains constant when the temperature changes (see Fig. 4.15). When the strain ε in microstrain ($\mu\varepsilon$) is applied on the HBF2 with constant temperature, the power ratio change $\Delta(P_1/P_3)$ is expected to be zero since the Bragg wavelength of the FBG does not change; $\Delta(P_2/P_3)$ can be obtained as $\Delta(P_2/P_3) = S_2 K_{\varepsilon(HBFLM2)} \varepsilon$, where

$K_{\varepsilon(HBFLM2)}$ refers to the wavelength shift of the HBFLM2 spectrum per $\mu\varepsilon$ of applied strain. The overall power ratio changes can be described as

$$\begin{bmatrix} \Delta(P_1/P_3) \\ \Delta(P_2/P_3) \end{bmatrix} = \begin{bmatrix} \alpha_1 & \beta_1 \\ \alpha_2 & \beta_2 \end{bmatrix} \begin{bmatrix} \varepsilon \\ \Delta T \end{bmatrix}, \tag{4.19}$$

where $\alpha_1 = 0$ and $\alpha_2 = S_2 K_{\varepsilon(HBFLM2)}$ are the strain coefficients for $\Delta(P_1/P_3)$ and $\Delta(P_2/P_3)$ respectively, and $\beta_1 = S_1 K_{T(FBG)}$ and $\beta_2 = S_2[K_{T(FBG)} - K_{T(HBFLM2)}]$ are the corresponding temperature coefficients, which can be determined by the experiment. Note that strain could also be applied to the FBG as in Ref. [26] instead of the HBF2.

4.4.2 Experiment and Discussion

Before measuring the matrix coefficients in Eq. (4.19), it is important to test the operating range of the sensor system first, since the HBFLM2 spectrum shifts with both the temperature and strain variations. Fig. 4.14 shows the transmission spectra of HBFLM2 with different strains under the temperature of 23 °C, while HBFLM2 spectra under different temperatures with zero strain are shown in Fig. 4.15. Both figures indicate the working range within which the Bragg wavelength falls in the linear region of the HBFLM2 spectrum. The Bragg wavelength always falls in the linear region of the HBFLM1 spectrum for a large temperature range, because the temperature sensitivity of the FBG is about only $\sim$ 13 pm/°C near 1550 nm. It can be seen that the proposed sensor scheme is expected to work within a temperature range of about 10 °C. Although the working range is much smaller than that in Ref. [26], the sensor scheme has a much higher temperature sensitivity, because the HBFLM has a much higher sensitivity than the MMF filter. From Figs. 4.14 and 4.15, it can be seen that the slopes for different temperature and strain remains almost constant within the working range.

In order to obtain the matrix coefficients in Eq. (4.19), strain and temperature are applied on the sensing head separately in the operating range. We first measure the strain responses of the sensing head by measuring the power ratio changes as a function of the applied strain at a temperature of 23 °C, as shown in Fig. 4.16. Fig. 4.17 shows the power ratio changes with respect to temperature changes by heating the tube from 23 °C to 34 °C under zero strain. The measured power ratio changes have good linear behavior with variations in strain and temperature. By inverting Eq. (4.19), the strain and temperature can be obtained simultaneously from

$$\begin{bmatrix} \varepsilon \\ \Delta T \end{bmatrix} = \frac{10^3}{8.7} \begin{bmatrix} -251 & -5.77 \\ 1.51 & 0 \end{bmatrix} \begin{bmatrix} \Delta(P_1/P_3) \\ \Delta(P_2/P_3) \end{bmatrix}, \tag{4.20}$$

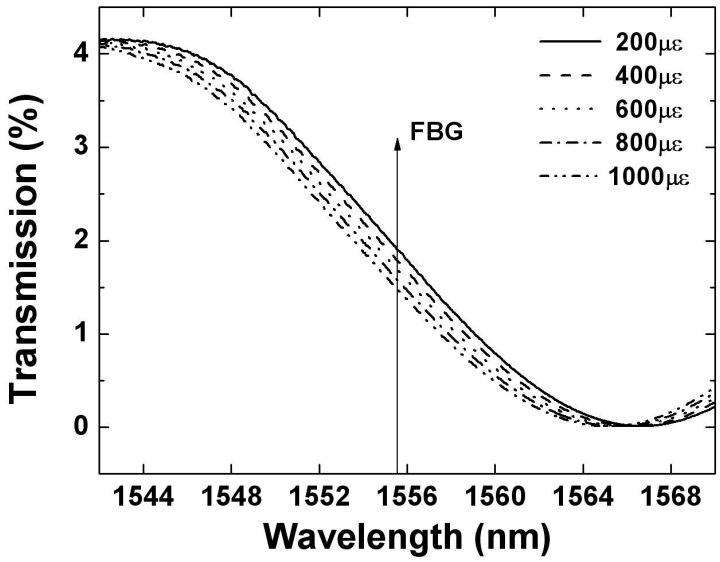

Figure 4.14: Transmission spectra of HBFLM2 with different applied strains under 23 °C.

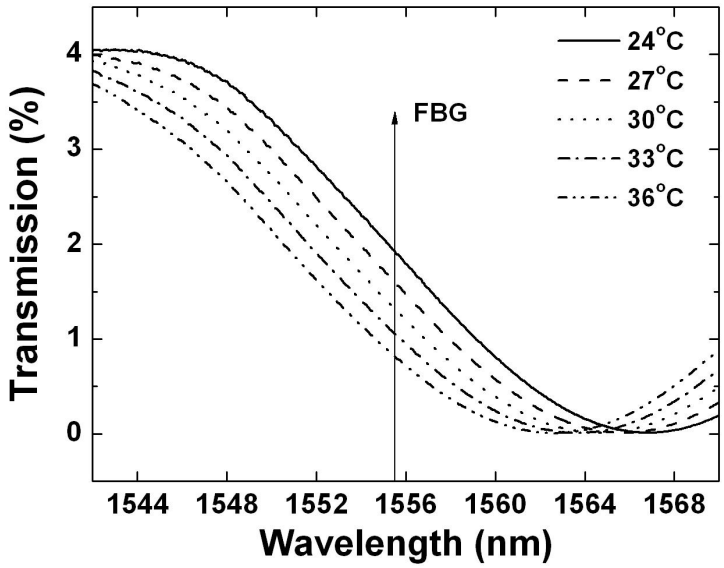

Figure 4.15: Transmission spectra of HBFLM2 under different temperatures with zero strain.

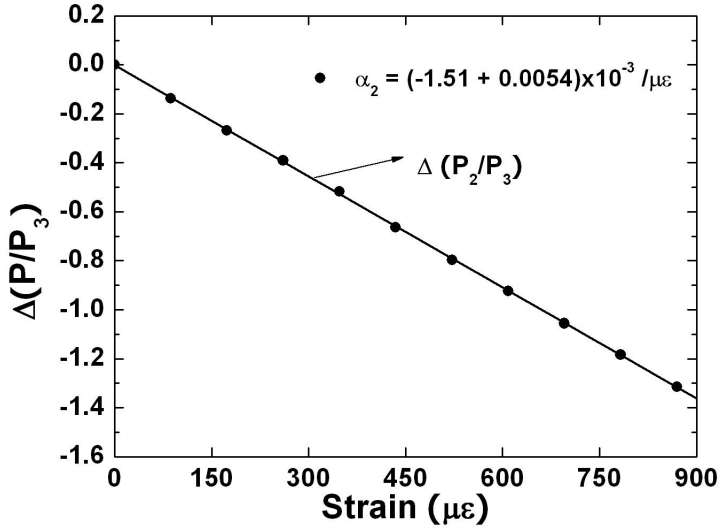

Figure 4.16: Power ratio change as a function of applied strain.

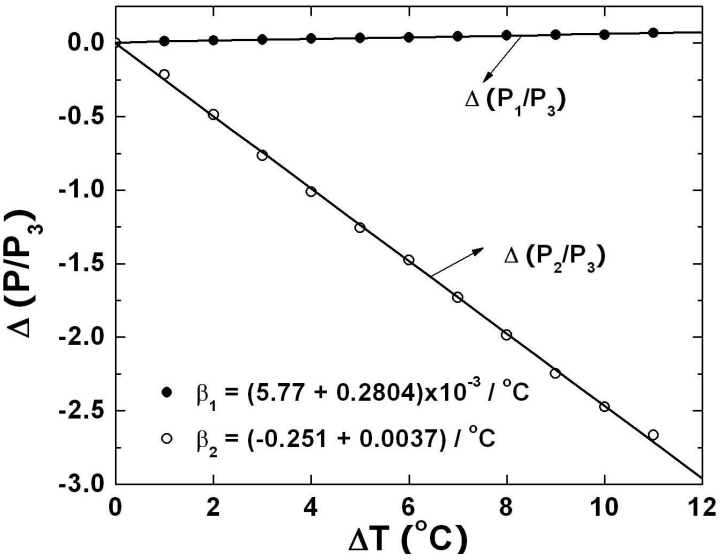

Figure 4.17: Power ratio change as a function of temperature change.

after the pair power ratio changes, $\Delta(P_1/P_3)$ and $\Delta(P_2/P_3)$), have been measured. The calculated resolutions of the proposed sensor system can reach about ± 0.2 °C in temperature and ± 29.5 $\mu\varepsilon$ in strain with the resolution of the power meter of 1 nW. However, it is hard to achieve these resolutions experimentally. All the devices need to be operated very accurately, and the power measured by the power meter must also be very accurate.

4.5 Conclusion

A sensing head based on a combination of an FBG and an HBFLM is described. The applied strain and ambient temperature change can be obtained by measuring the wavelength shifts of the FBG and the HBFLM filter that acts as an MZI. The experiment result shows that the proposed sensor can simultaneously measure strain and temperature with a resolution of ± 1 °C in temperature and ± 21 $\mu\varepsilon$ in strain.

An alternative all-fiber sensing scheme to realize discriminative measurement of temperature and strain by SDM two HBFLMs constructed with the same HBF is proposed and experimentally demonstrated. The advantage is that HBFLMs have higher sensitivities with respect to strain and temperature than those of the FBGs. With the SDM technique and sequential measurement of the resonance wavelength shifts of the HBFLMs, discriminative measurement of temperature and strain can be realized with high resolutions in temperature and strain. It is also expected to have applications in distributed HBFLM sensing.

In order to avoid using OSAs to monitor the wavelength shifts, an improved temperature and strain sensor system based on an FBG and two HBFLMs is presented. Simultaneous measurement of strain and temperature can be achieved using an intensity-based interrogation method with low cost and high speed. The resolutions of the sensor system were estimated as ± 0.2 °C in temperature and ± 29.5 $\mu\varepsilon$ in strain, which can be attributed to the resolutions of the power meters.

Chapter 5

Small Core Diameter Multimode Fiber Based Intermodal Interferometer and Its Applications in Fiber Sensors

5.1 Introduction

Different types of force sensors based on fiber Bragg gratings (FBGs), Mach-Zehnder interferometers (MZIs), high-birefringence fibers, etc. have been developed. Among them, the use of an FBG has to adopt a specially designed beam to realize the temperature and force discrimination [1, 2, 3], which leads to a complicated sensing structure. In addition, the force sensors with two FBGs [4, 5] to realize the temperature and force discrimination result not only in measurement errors due to the temperature-strain cross effect of the FBG sensor, but also a complicated structure and high price. The force sensor based on MZI [6] has to use a complicated sensing structure to tune the reference arm. Moreover, the fabrication of MZI is complicated. High-birefringence fiber-based sensor [7] could realize the distributed force measurement, but the temperature influence is not considered. Compared to the above fiber sensors, multimode fiber (MMF) interference sensors based on modal interference [8] have the advantages of low cost and simple structure, which have attracted much attention. Reported MMF interference sensors are focusing on the strain and temperature measurement [9, 10, 11, 12, 13, 14]. However, most of the MMF interference strain sensors do not consider the temperature influence [9, 13]. One method to overcome the temperature influence on the MMF interference sensor has been presented in Chapter 3. By cascading an FBG to the MMF interferometer, simultaneous measurement

of strain and temperature can be realized. However, the MMF interferometer has to be cascaded to an FBG.

In the second section of this chapter, a temperature- and phase-independent lateral force sensor based on a core-offset MMF interferometer is presented. The MMF used in this chapter is actually a small core-diameter dispersion compensation fiber (DCF). The DCF was originally designed for dispersion compensation applications, with a core/cladding diameter of 1.9/115.7 μm, a large dispersion parameter of -270 ps/nm/km at 1550 nm, and a cutoff wavelength of 1663 nm. It is claimed as an MMF because the fact of the cutoff wavelength at 1663 nm makes it naturally an MMF at wavelengths shorter than 1663 nm. By misaligning a fused cross section between the single-mode fiber (SMF) and MMF, a core-offset MMF interferometer with high optical intensity extinction ratio can be obtained. This extinction ratio will change with the variations of the lateral force applied to a short section of the MMF, while the interference phase will remain almost constant. Moreover, it is independent on the temperature variations. Experimental results show that the extinction ratio varies quadratically with the applied lateral force. This type of sensor has the advantages of temperature- and phase-independency, high sensitivity, low cost, and simple structure.

Since lateral force or lateral strain could be measured by considering the extinction ratio change of the interference spectrum, it is expected to apply this feature to measure more than one direction of strain simultaneously (longitudinal strain would result in spectrum shifts). Several multidirectional strain sensors [15, 16] have been reported, such as using a planar fiber optic sensor array [15], or forming an SMF MZI [16] where three sensing arms are needed. However, each of them has to use more than two sensing heads and has a very complex structure, which increases the cost of the system and limits its "real-world" application. Moreover, it is interesting to realize multiparameter measurement with a compact sensing head in today's industry, but most of the reported MMF sensors [9, 13, 17, 18] are focusing on one-parameter measurement. One simple and compact sensor with only one sensing head to realize multidirectional strain measurement and multiparameter measurement is very attractive.

In the third section of this chapter, we apply the core-offset MMF interferometer developed in Section 5.2 for this purpose. We found that this type of interferometer with only one sensing head can effectively realize simultaneous measurement of transverse and longitudinal strain or simultaneous measurement of transverse strain and temperature. The extinction ratio of the interference spectrum will change with the variations of the transverse force applied to a short section of the MMF, while the interference phase will remain almost constant. Moreover, it is almost independent of the longitudinal strain variation applied to the whole MMF or temperature variations, which can be applied to measure both the transverse and longitudinal strain, or both transverse strain and temperature simultaneously.

On the other hand, there is considerable interest in developing methods by monitoring other parameters other than wavelength information provided by the sensor head, because the spectrum information is usually obtained by optical spectrum analyzers (OSAs) which are expensive and have a slow scanning speed. Many passive detection interrogators involving no tracking, scanning, or modulating mechanisms have been reported, such as using linearly wavelength-dependent devices [19, 20, 21, 22], identical chirped grating pairs [23], and charge-coupled device (CCD) spectrometers [24]. For active detection schemes which require more complex systems compared to the passive ones, Fabry-Pérot filter interrogators [25], fiber Fourier transform spectrometer interrogators [26], and many other techniques have also been demonstrated. The most cost-effective method among both the passive and active schemes is to develop an intensity-based interrogation system using a linearly wavelength-dependent optical filter. Sensor systems that adopt this type of demodulator have been commercialized.

In the fourth section, we present an improved fiber sensor configuration that is feasible to measure lateral force using a core-offset MMF interferometer illustrated in Section 5.2. When a lateral force is applied to a short section of the MMF, the extinction ratio decreases accordingly. By measuring optical power variations instead of the spectrum change, lateral force measurement can be achieved with a low cost and high speed. In addition, the sensor head can be encapsulated into the temperature compensation material to meet practical application.

Moreover, to meet the increasing demands of modern industry, it is interesting to develop compact sensor for high temperature measurement. Miniature fiber sensors are desired in high-temperature sensing, since it is difficult to fabricate a bare fiber sensing head or to coat a special layer on the sensing head to avoid fiber coating burning if the sensing fiber is too long. In addition, long sensing head is usually easily influenced by other ambient disturbances besides temperature. Although miniature high-temperature fiber sensors based on Fabry-Pérot interferometer (FPI) [27, 28, 29] are demonstrated, they need complicated fabrication process such as etching [27] and laser micromachining [28] to form a single FPI cavity, or cascading three sections of fibers (a photonic crystal fiber, a hollow optical fiber and an SMF) to form a hybrid FPI cavity [29]. Moreover, the length of the fiber FPI sensors is generally more than 1 cm. On the other hand, a miniature high-temperature fiber sensor based on modal interference was fabricated with a 1.2 cm length by cascading two MMFs and three SMFs [10]; however, the structure of the sensing head is rather complex, and the fabrication process is not easy.

In Section 5.5, a miniature high-sensitivity, high-temperature fiber sensor with a small-core MMF interferometer is presented. The sensing head has an SMF-MMF configuration formed with a 4-mm long bare MMF with one end being spliced to a section of SMF and the other end being cleaved. Within the temperature measurement range of 25 °C to 600 °C, a high sensitivity of 68.6 pm/°C is obtained by monitoring the wavelength shift

of the interference spectrum. Moreover, our proposed sensor has been made 22 and 84 times smaller than the two sensor schemes in [9, 11], considering that all the sensors have the same free spectral range (FSR). This is because the small-core-diameter MMF has a much larger mode index difference between the two interference modes than that of the conventional step-index or graded-index MMF. Such a unique property allows us to make compact and miniaturized optical fiber sensor for high-temperature sensing.

5.2 Temperature- and Phase-Independent Lateral Force Sensor

A lateral force sensor based on a core-offset MMF interferometer is presented. High extinction ratio can be obtained by misaligning a fused cross section between the SMF and MMF. With the variation of the lateral force applied to a short section of the MMF, the extinction ratio changes while the interference phase remains almost constant. The change of the extinction ratio is independent of temperature variations as well. The proposed force sensor has the advantages of temperature- and phase-independency, high sensitivity, low cost, and simple structure.

5.2.1 Operation Principle

As shown in Fig. 5.1, the core-offset MMF interferometer has a three-segment fiber structure, where a section of MMF of length L is connected to two standard communication SMFs. The MMF was originally designed for dispersion compensation applications, with a large dispersion parameter of -270 ps/nm/km at 1550 nm and a cutoff wavelength of 1663 nm. The core/cladding diameter of the MMF is 1.9/115.7 μm. The SMF-MMF-SMF structure can act as an MZI, based on intermodal interference. Many modes with different propagation constants can be excited when the light is coupled into the MMF from SMF at Point 1. When these modes are re-coupled back into the SMF at Point 2, they will interfere with each other. If only considering two dominant modes, the transmission spectrum is approximately a periodic function, given by

$$I = I_1 + I_2 + 2\sqrt{I_1 I_2}\cos[\frac{2\pi(n_2 - n_1)L}{\lambda}], \tag{5.1}$$

where I_1 and I_2 are the intensities distributed in the lower-order and higher-order dominant modes, respectively, with $I_2 < I_1$; n_2 and n_1 are the effective refractive indices of the two modes respectively, and λ is the wavelength of light in vacuum. The extinction ratio ER

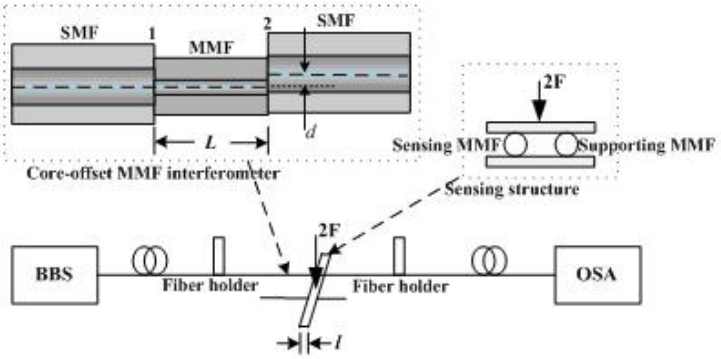

Figure 5.1: Schematic diagram of the experimental setup (Insets show the interferometer structure and the sensing structure, respectively).

of the interferometer can be given by

$$ER = 10\lg(\frac{1+\sqrt{I_2/I_1}}{1-\sqrt{I_2/I_1}})^2. \tag{5.2}$$

Fig. 5.2 shows the extinction ratio as a function of the intensity ratio I_2/I_1 of the two interfering modes. It can be seen that larger intensity ratio of I_2/I_1 gives rise to higher extinction ratio. The extinction ratio for the directly fused 1.9/115.7 μm MMF interferometer without core-offset is generally lower than 4 dB, corresponding to a intensity ratio of 0.01. In order to obtain a high extinction ratio, we have to increase the intensity ratio I_2/I_1, which can be realized by manually offsetting the cores between the SMF and MMF at splicing Point 2. The core-offset splicing is an effective method to control mode coupling [30]. The offset dependent loss characteristic is firstly studied with an MMF about 24 cm in length. The splicing Point 1 is fused directly without core-offset. Using a broadband source (BBS) with the transmission power spectrum shown as the dotted line in Fig. 5.3, the transmission power spectra of the interferometer are shown in Fig. 5.3 for different core-offset distances of d at splicing Point 2. It can be seen that there is a best offset position to obtain maximum extinction ratio. The rather uniform spectra in Fig. 5.3 confirm that the interference is mainly produced by two dominant modes. Because other higher-order modes are very weak, they have little influence on the interference.

When a lateral force is applied to a short section of the MMF, deformation is produced in the MMF, which will result in power loss of the two modes. For a given applied lateral force, the higher-order mode with intensity I_2 has more power loss than that of the lower-order mode. Moreover, the power of the higher-order mode decreases much faster than that of the lower-order mode when the force increases. Thus, the intensity ratio of the two interference modes I_2/I_1 decreases accordingly with the increase of the lateral force,

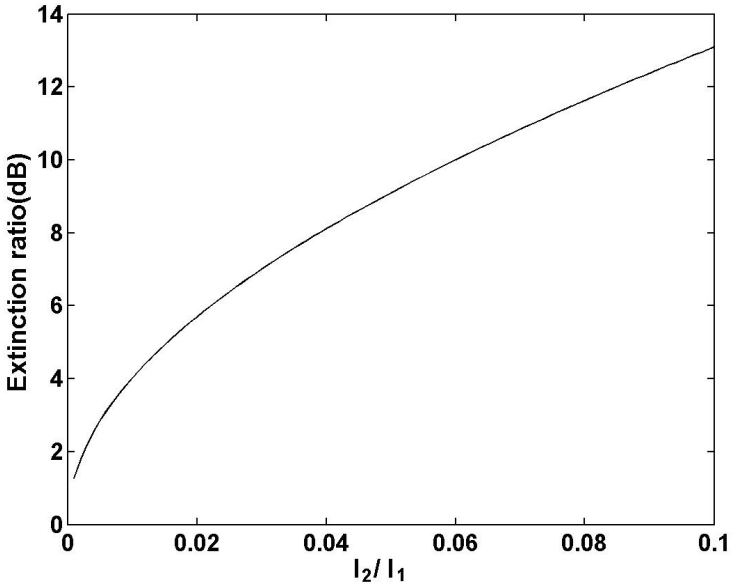

Figure 5.2: Extinction ratio as a function of the intensity ratio I_2/I_1 of the two interference modes.

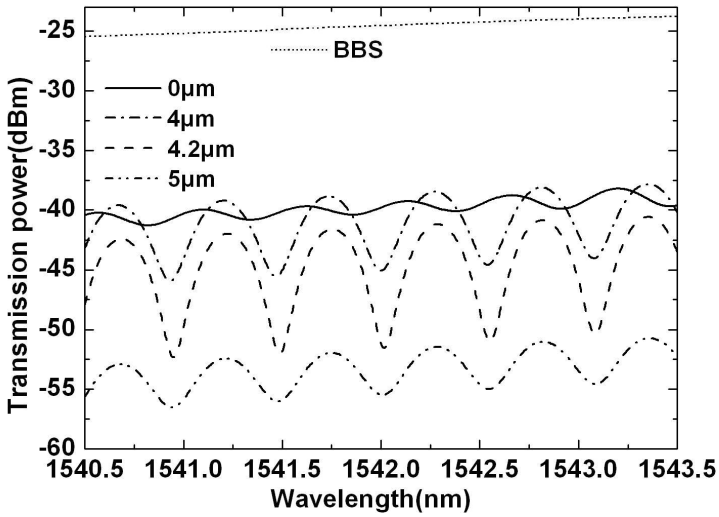

Figure 5.3: Transmission power spectra of the BBS and the MMF interferometer with core-offset d about 0, 4, 4.2, and 5 μm, respectively.

which will lead to a decrease of the extinction ratio (see Fig. 5.2). With the same lateral force applied to the MMF, the core-offset interferometer with higher extinction ratio will have a larger reduction in extinction ratio. The above phenomena can be applied to the measurement of the lateral force. When a lateral force is applied to a short section l of the MMF, the elongated length Δl of the section is far less than L, producing negligible longitudinal strain ($\Delta l/L \approx 0$). Thus the phase in Eq. (5.1) is only determined by the difference of the two effective mode indices at a given value of λ. The birefringence variation ΔB per unit length of the core refractive index under the lateral force can be expressed as [31]

$$\Delta B = \frac{4kF}{\pi r l E}, \tag{5.3}$$

where k is strain optical coefficient, F is the force acting on fiber of length l, and r, E are the outer radius and Young's Modulus of the fiber, respectively. Under the lateral force, the two interfering modes approximately experience the same amount of variation according to Eq. (5.3). Thus the difference between two effective mode indices of $n_2 - n_1$ almost remains constant. As a result, the interference phase is independent of the lateral force, which can be applied to phase-independent force measurement.

When the ambient temperature changes, the transmission spectrum of the MMF interferometer will shift, which is related to the thermal expansion and thermo-optic coefficients of the MMF material [9, 11]. Although the extinction ratio varies with the applied lateral force, it does not change with the temperature variation. This feature can be applied to temperature-independent force measurement.

5.2.2 Experiment Results and Discussions

The sensing structure is shown in Fig. 5.1. With the above fabrication method, a core-offset MMF interferometer sensor with the MMF length about 22 cm is fabricated. The extinction ratio reaches 8 dB, as shown in Fig. 5.4. A section of MMF identical to the sensing MMF is used as a supporting fiber. Rotation of the MMF will lead to nonuniform interference spectrum mainly because part of the power in the dominant interfering modes is coupled into other higher-order modes. In order to avoid the rotation of the MMF, the interferometer is supported by two fiber holders placed on an optical table, and the supporting MMF and sensing MMF are fixed between two aluminum flakes with smooth surfaces. The width of the aluminum flake is about 1 cm. The transmission spectrum of the sensor is monitored by an OSA. With different forces applied to the MMF, the extinction ratio changes accordingly, while the interference phase remains constant, as shown in Fig. 5.5.

Fig. 5.6 shows the responses of the extinction ratio (see the extinction ratio between the two arrow marks in Fig. 5.5) to different lateral forces. It can be seen that there is

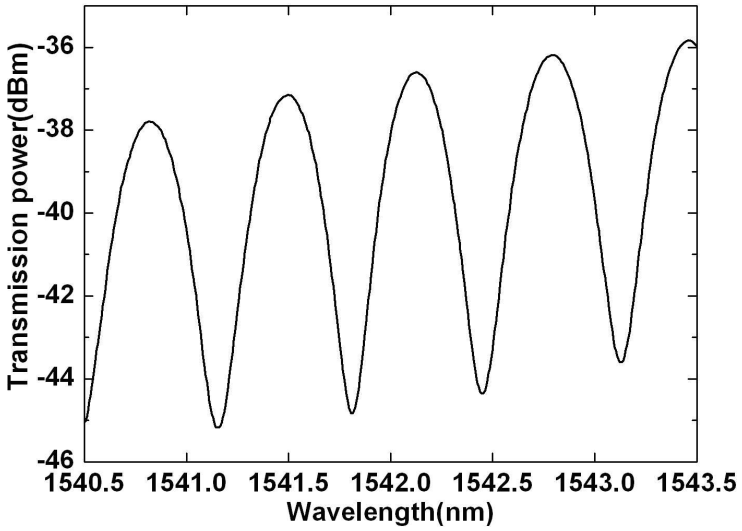

Figure 5.4: Transmission spectrum of the core-offset MMF interferometer sensror.

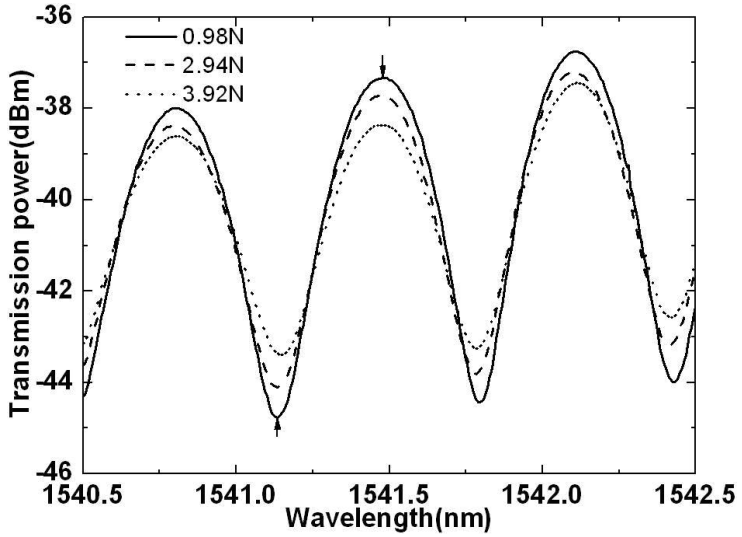

Figure 5.5: Measured transmission spectra under different lateral forces.

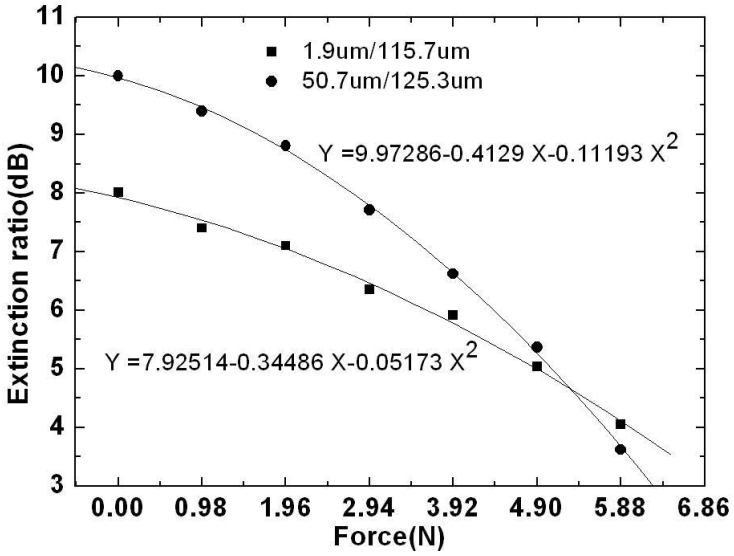

Figure 5.6: Extinction ratio responses to different lateral forces.

a good quadratic relationship between the extinction ratio and the force for the 1.9/115.7 μm MMF-based sensor. In addition, another gradient index MMF of length 150 cm and core/cladding diameter of 50.7/125.3 μm is used to measure the lateral force with the same sensing mechanism. Again, a good quadratic relationship between the extinction ratio and the applied force is found, as shown in Fig. 5.6. The extinction ratio of the 50.7/125.3 μm MMF-based sensor is more sensitive to the lateral force than that of the 1.9/115.7 μm MMF-based sensor. However, the interferometer based on the 50.7/125.3 μm MMF needs a longer fiber, which is vulnerable to the influence of the ambient disturbance and is not suitable for smart sensing in actual measurement environment. The interferometer based on the 1.9/115.7 μm MMF with shorter length is more suitable for practical applications.

Fig. 5.7 shows the transmission power spectra of the 1.9/115.7 μm MMF-based sensor under different temperatures at a fixed force of 2.94 N. When the temperature increases, the spectrum has a red shift; a wavelength shift of 1.516 nm is observed when the temperature varies from 23 °C to 50 °C. However, the extinction ratio is almost unaffected when ambient temperature changes. Additional experimental results show that in the temperature range of $23 - 60$ °C, the variation of the extinction ratio with the applied force can be well described by a quadratic relation. However, when the temperature is over 60 °C, the extinction ratio and phase responses to temperature start to change erratically, which is attributed to the limitation of the thermal property of the MMF and aluminum flake materials. The operational temperature range may be extended by encapsulating temperature compensation materials with negative temperature coefficient to the sensor. In order to avoid breaking the MMF, the force is controlled in the range of $0 - 5.88$ N. The

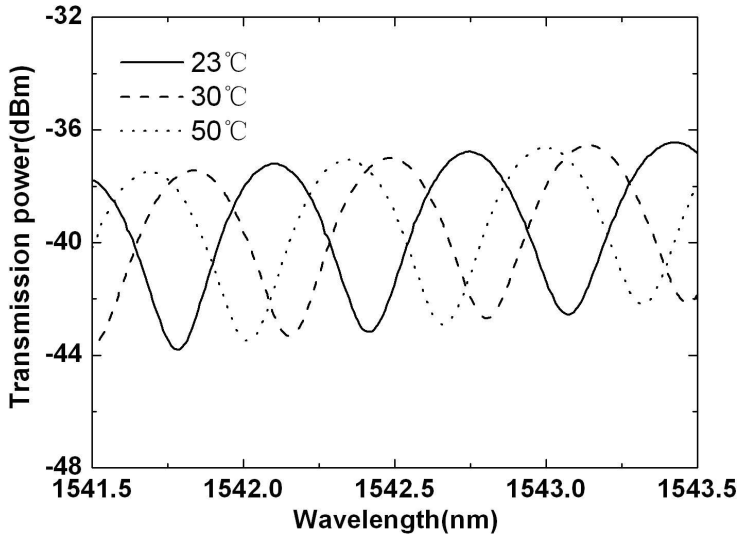

Figure 5.7: Measured transmission power spectra under different temperatures at a fixed force of 2.94 N.

operational force range of the sensor can be increased by encapsulating the MMF sensing head in materials with high Young's modulus for practical applications.

5.3 Simultaneous Measurement of Transverse and Longitudinal Strains

A scheme to realize simultaneous measurement of transverse and longitudinal strains with only a 22-cm MMF based on MZI principle is presented. With the transverse strain applied to a short section of the MMF and the longitudinal strain applied to the whole MMF, there is almost no cross-talk between the extinction ratio variation induced by the transverse strain and the wavelength shift induced by the longitudinal strain. By monitoring the extinction ratio and the wavelength variations of the interferometer, the transverse and longitudinal strains can be measured simultaneously. The longitudinal strain varies linearly with the wavelength shift of the interference spectrum, while the extinction ratio varies quadratically with the transverse strain. It has the advantages of low cost, simple and compact structure.

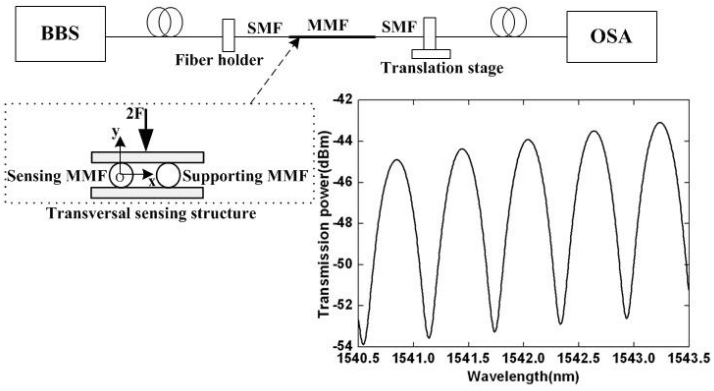

Figure 5.8: Experiment setup and transmission spectrum of the interferometer (Inset shows the transverse sensing structure).

5.3.1 Principle

A. Structure and Characteristics of the Interferometer

Fig. 5.8 shows the experimental setup. A C-band broadband source (BBS) is used as the light source. The transmission spectrum of the interferometer is measured by an OSA. The interferometer is formed by about a 22-cm MMF sandwiched between two SMFs (SMF-28 type), which serves as an MZI based on intermodal interference. The extinction ratio for the MMF interferometer without core offset is generally small. In order to obtain a high extinction ratio, we slightly offset a splice between the MMF and the SMF. The extinction ratio of the typical interference spectrum shown in Fig. 5.8 is more than 9 dB. It can be seen that the interference is mainly produced by two dominant interference modes, which indicates that other existing modes are carrying much less power compared to the two interference modes. In order to study the interference modes' type, several core-offset MMF interferometers are fabricated with the cladding layer of the MMF being stripped. After the bare MMFs are immersed in the index-match liquid, the transmission spectra remain unchanged, which confirms that the interfering modes are core modes. The extinction ratio, ER, of the interferometer can be approximately expressed as

$$ER = 10\lg(\frac{1+\sqrt{I_2/I_1}}{1-\sqrt{I_2/I_1}})^2, \tag{5.4}$$

where I_1 and I_2 are the intensity distributed in the lower-order and higher-order interfering modes, respectively, with $I_2 < I_1$. The extinction ratio is related to the intensity ratio I_2/I_1 of the two modes and decreases with the reduction of the intensity ratio [17]. Note that rotation or twist of the MMF will lead to the variation of the interference spectrum, which

is mainly because part of the power in the dominant interference modes is coupled into other weak modes. In order to avoid the influence of rotation or twist of the MMF on the measurement result, the MMF is supported on an optical table by a fiber holder and a translation stage, which provides the longitudinal strain to the sensor head; moreover, the sensing MMF and a supporting MMF (identical to the sensing MMF) are fixed between two aluminum flakes with smooth surfaces, which provide the transverse strain to the sensor head, as shown in Fig. 5.8. The width of the aluminum flake is about 1 cm.

B. Sensing Principle

When a transverse force applied to a short section of the MMF, the extinction ratio will decrease with the increase of the transverse force [17]. The transverse strain induced by the transverse force can be expressed as

$$[\varepsilon_x, \varepsilon_y] = [\frac{1+3\gamma+2\gamma^2}{\pi E b l} F, \frac{2\gamma^2-\gamma-3}{\pi E b l} F], \tag{5.5}$$

where ε_x and ε_y are the x and y components of the strain induced by the transverse force; F is the force acting on the short section of MMF l; and γ, b, and E are the Poisson's coefficient, outer radius, and Young's modulus of the fiber, respectively. It can be seen that the transverse strain is proportional to the transverse force directly.

When a longitudinal strain is applied to the MMF, the transmission spectrum of the MMF interferometer will shift, which is related to only the Poisson's ratio and effective strain-optic coefficient of the fiber. The transverse force is applied to only a short section of MMF, which is much shorter than the whole length of the MMF. As the elongation of the MMF induced by the transverse force is far less than the length of the MMF, the resultant longitudinal strain in the short section (where the transverse force is applied) is negligible; therefore, the interference spectrum produced by the whole MMF will not shift due to the applied transverse strain. Although the extinction ratio varies with the applied transverse force, it almost does not change with the variation of the longitudinal strain. This feature can be used to measure the transverse and longitudinal strain simultaneously.

Moreover, The response of the MMF interferometer to temperature is only related to the thermal expansion and thermo-optic coefficients of the fiber material. The extinction ratio only varies with the applied lateral force, while it does not change with the temperature variation [17]. This feature could be applied to realize simultaneous measurement of transverse strain and temperature.

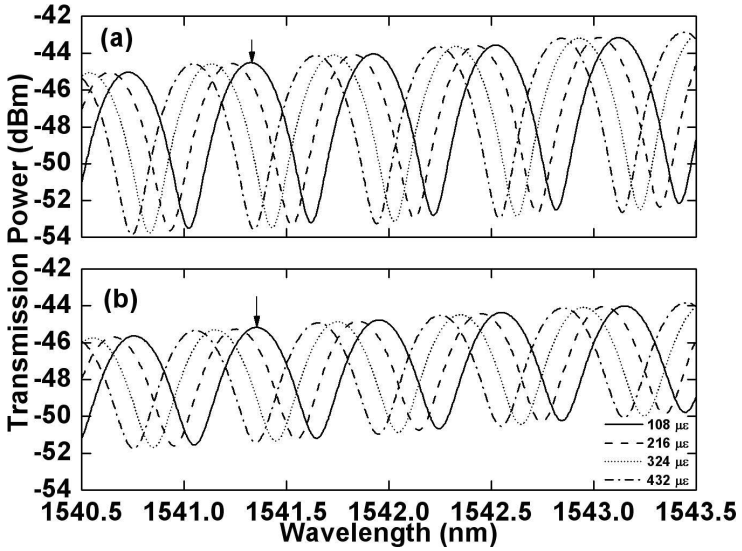

Figure 5.9: Transmission spectral response to different longitudinal strains at a fixed transverse force of (a) 0 N and (b) 2.94 N.

5.3.2 Experiment Validation and Discussion

A. Response to Transverse and Longitudinal Strain

Fig. 5.9 shows the transmission power spectra of the sensor under different longitudinal strain at fixed transverse force of 0 N and 2.94 N. When the longitudinal strain increases, the transmission spectrum of the sensor has a blue shift. It can be seen that the longitudinal strain only leads to the wavelength shift of the transmission spectra of the sensor and almost does not affect the extinction ratio. Fig. 5.10 shows the relationship between the measured wavelength (marked with an arrow in Fig. 5.9) and the longitudinal strain under fixed transverse force of 0 N and 2.94 N. It can be seen that there is a good linear relationship between the wavelength and the longitudinal strain under 0 N transverse force, and the longitudinal strain sensitivity is 0.82×10^{-3} nm/$\mu\varepsilon$. The longitudinal strain resolution is about 12 $\mu\varepsilon$ for the OSA with a 10 pm resolution. The response for nonzero transverse force also has a good linear relationship. For the same longitudinal strain, the measured wavelengths at different fixed transverse forces are slightly different; the maximum wavelength deviation is less than 0.02 nm at zero longitudinal strain. Experimental results show that when the longitudinal strain is larger than 108 $\mu\varepsilon$, the maximum slope difference under different transverse forces is less than 1×10^{-5} nm/$\mu\varepsilon$, and the wavelength deviation induced by the transverse force becomes negligible, as shown in Fig. 5.10. Such a small crosstalk can be relieved by using a pre-applied longitudinal strain.

Fig. 5.11 shows the transmission spectral response to different transverse forces at a

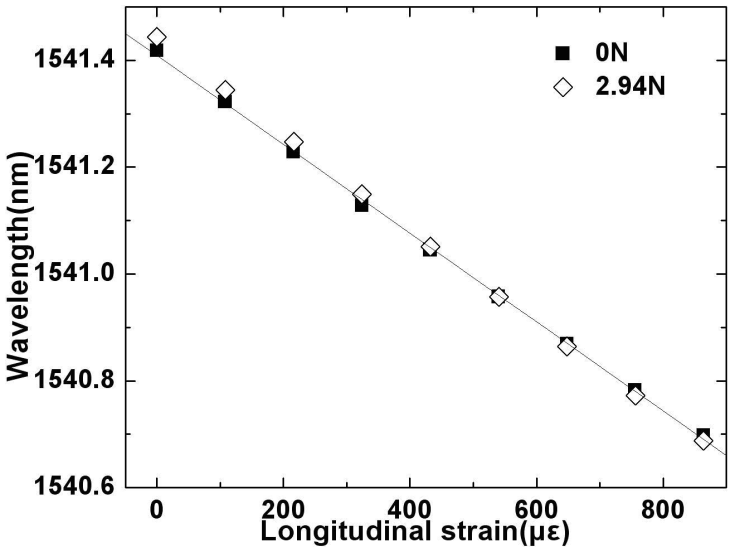

Figure 5.10: Relationship between the wavelength and the longitudinal strain under fixed transverse force of (a) 0 N and (b) 2.94 N.

fixed longitudinal strain of 0 $\mu\varepsilon$ and 432 $\mu\varepsilon$. It can be seen that when the transverse force increases, the extinction ratio decreases accordingly, and the interference phase of the MMF interferometer is almost unaffected. Fig. 5.12 shows the relationships between the measured extinction ratio (between the two marked arrows shown in Fig. 5.11) and the transverse strain ε_x and ε_y induced by the transverse force at a fixed longitudinal strain of 0 $\mu\varepsilon$ and 432 $\mu\varepsilon$, respectively. There is a good quadratic relationship between the extinction ratio and the transverse strain under zero longitudinal strain. The response for nonzero longitudinal strain also has a good quadratic relationship. For the same transverse strain, the measured extinction ratios at different fixed longitudinal strains are slightly different; the maximum extinction ratio deviation is less than 0.1 dB, which has negligible influence on the measured quadratic relationship shown in Fig. 5.12. Note that the transverse strain resolution is related to amplitude noise, which might arise from the fluctuation of the BBS or the accuracy of the power measured by the OSA. In addition, the transverse strain sensitivity increases with an increase of the transverse strain; thus, the resolution is different at different transverse strain. Experimental results show that an extinction ratio response can be observed by applying a minimum transverse strain of 3.18 $\mu\varepsilon$. In order to avoid breaking the MMF, the applied transverse force is controlled in the range of 0-4.41 N, resulting in transverse strain ε_x and ε_y in the range of $0 - 57.3$ $\mu\varepsilon$ and $0 - 114.66$ $\mu\varepsilon$, respectively. The applied longitudinal strain is controlled in the range of $0 - 864$ $\mu\varepsilon$. The measurement ranges of ε_x, ε_y, and ε_z can be increased by encapsulating the MMF sensing head in materials with a high Young's modulus for practical applications.

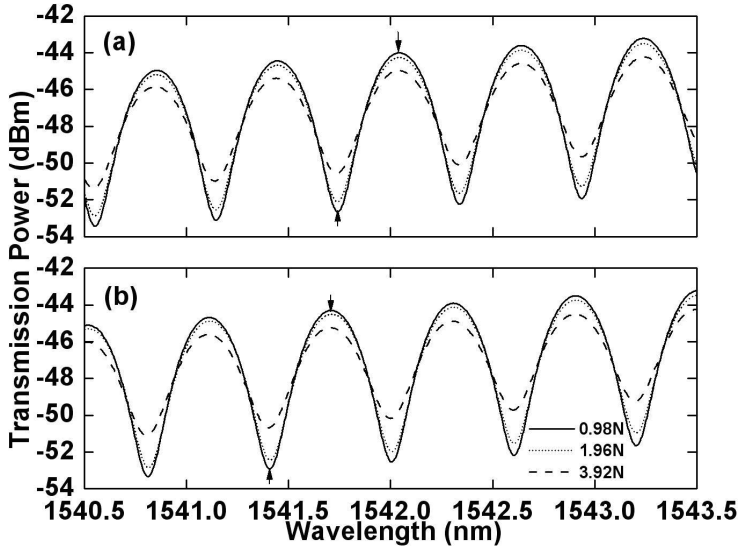

Figure 5.11: Transmission spectral response to different transverse forces at a fixed longitudinal strain of (a) 0 $\mu\varepsilon$ and (b) 432 $\mu\varepsilon$.

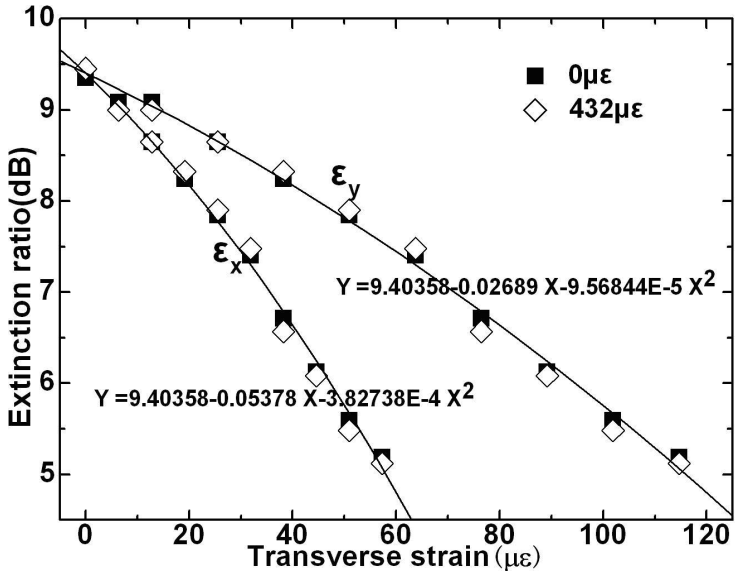

Figure 5.12: Relationship between the extinction ratio and the transverse strain at a fixed longitudinal strain of (a) 0 $\mu\varepsilon$ and (b) 432 $\mu\varepsilon$.

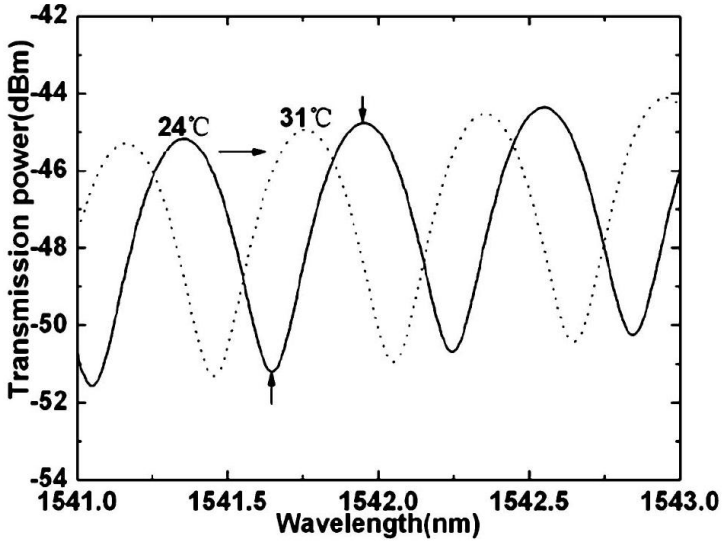

Figure 5.13: Transmission spectral response to temperature under transverse force of 2.94 N.

B. Response to the Temperature and Transverse Force

If only the transverse force is applied to the short section of the MMF, the spectrum of the interferometer will have a redshift with an increase of the ambient temperature, as shown in Fig. 5.13. There is a good linear relationship between the wavelength and temperature change, as shown in Fig. 5.14. The sensitivity reaches 0.058 nm/°C. However, the measured extinction ratio (between the two arrow marks in Fig. 5.13) is almost unaffected, and the extinction ratio fluctuation is less than 0.05 dB for a given transverse force, as shown in Fig. 5.15. The above phenomenon can be used to realize simultaneous measurement of transverse strain and temperature. Additional experiment shows that the extinction ratio response to temperature has variations without applying transverse strain when the temperature is increasing over 60 °C. This is because the core diameter and the length of the MMF will have a relatively large variation under higher temperature, which will have corresponding influences on the coupling of the interfering modes. The proposed MMF interferometer can be used to measure both transverse and longitudinal strains, or both transverse strain and temperature simultaneously with low crosstalk. In addition, if it is used as a two-directional (transverse and longitudinal) strains sensor, the sensing head can be encapsulated in temperature compensation materials in order to reduce the temperature-strain cross effect.

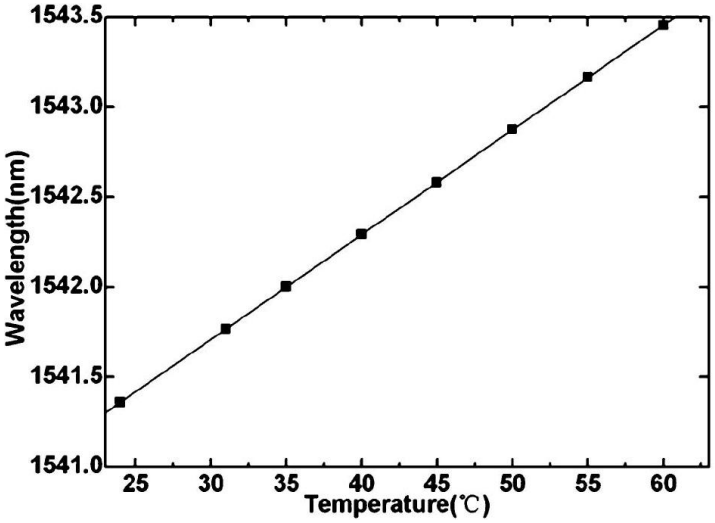

Figure 5.14: Relationship between the wavelength and temperature under transverse force of 2.94 N.

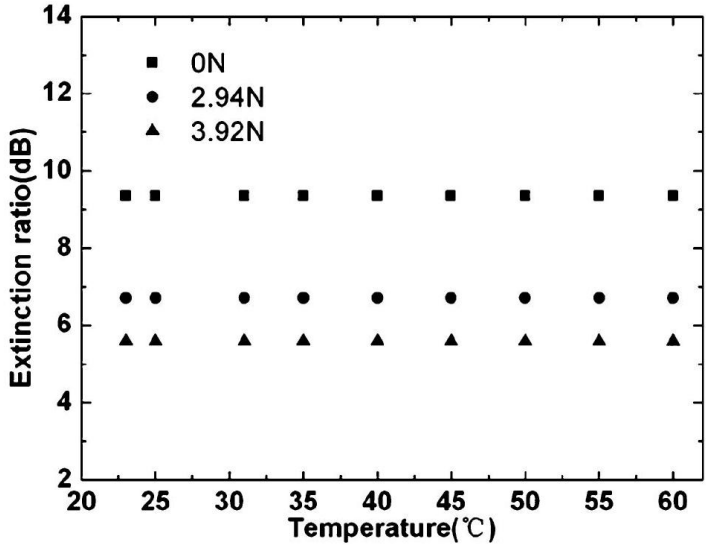

Figure 5.15: Measured extinction ratio response to temperature.

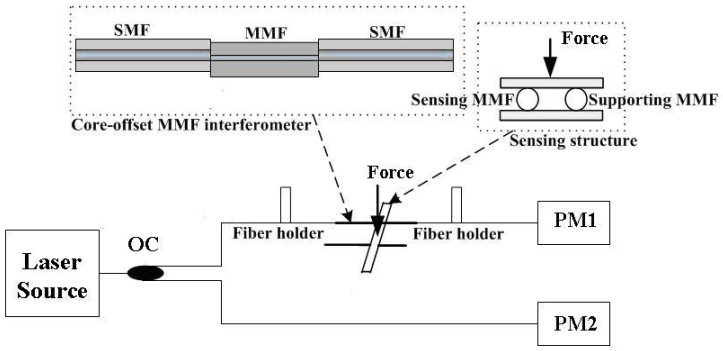

Figure 5.16: Experiment setup. PM: Power meter; OC: Optical coupler.

5.4 Lateral Force Sensor with Intensity-Based Interrogation Technique

A lateral force sensor based on a core-offset MMF interferometer with intensity-based interrogation technique is reported. An offset between the cores of the single-mode fiber and MMF is made to produce high extinction ratio. When a lateral force is applied to a short section of the MMF, the extinction ratio decreases with the interference phase almost unchanged. In addition to serving as a sensing head, the MMF can also act as a filter to realize lateral force measurement by measuring the power change from a power meter. Experiment results show that the power ratio change has a linear relationship with respect to the applied lateral force.

5.4.1 Experiment Setup and Operation Principle

Fig. 5.16 shows the experiment setup. A tunable laser is used as a light source. The light from the laser source is split by a 3-dB OC. In one path, power P2 is directly measured by a power meter (PM2), as a reference to eliminate any power fluctuation from the optical source; in the other path, power P1 is measured by another power meter (PM1) after passing a section of MMF. The MMF was originally designed for dispersion compensation applications, with a large dispersion parameter of -270 ps/nm/km at 1550 nm and a cutoff wavelength of 1663 nm. The core/cladding diameter of the MMF is 1.9/115.7 μm. As shown in Fig. 5.16, the MMF is sandwiched between two SMFs acting as an MZI based on intermodal interference, with an offset between the MMF core and the SMF core. The core offset is made to increase the extinction ratio of the interferometer, since the core-offset splicing is an effective method to control mode coupling. The spectra of the MMF interferometer and the laser source are shown in Fig. 5.17. The central wavelength of the

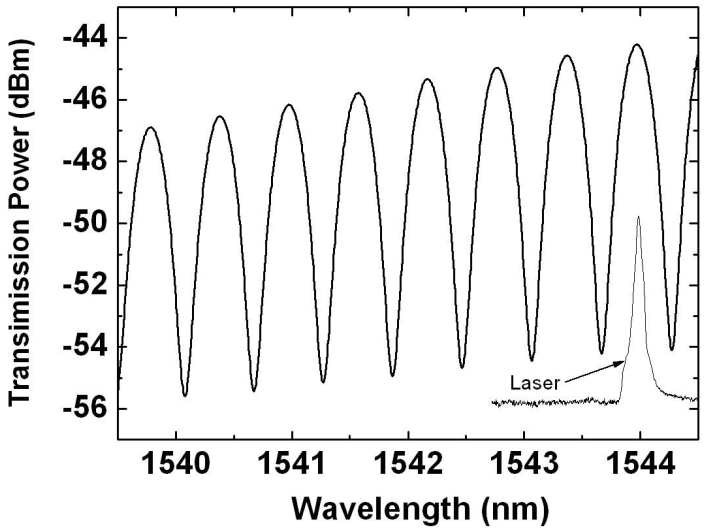

Figure 5.17: Spectra of the MMF interferometer and the laser source.

laser source is adjusted at 1544 nm, one of the peak transmission of the MMF spectrum. The MMF, more strictly speaking the SMF-MMF-SMF structure, act as an MZI based on intermodal interference. Many modes are excited when the light is coupled into the MMF. Each of the modes has a different propagation constant. When they recouple back into the SMF after passing through the MMF, the modes interfere. Each mode has experienced a different phase shift. If only two dominant modes are excited, the resultant interference fringe pattern is approximately sinusoidal with a uniform extinction ratio determined by the ratio of the intensities in the two modes (e.g., the best mode operation is to launch equal power in the two modes). If other higher order modes are excited, the interference fringe pattern will be modulated by their presence. Since the spectrum in Fig. 5.17 is rather uniform, confirming that only two modes primarily interfere in our case. The measured interference shown in Fig. 5.17 can be approximately expressed as

$$I = I_1 + I_2 + 2\sqrt{I_1 I_2}\cos[\frac{2\pi\Delta nL}{\lambda}] \,, \tag{5.6}$$

where I_1 and I_2 are the intensities distributed in the two interference modes, respectively; Δn is the mode index difference of the two modes; and λ is the wavelength of light in vacuum. The free spectral range (FSR) of the interfering spectrum can be given by Eq. (5.6) as

$$FSR \approx \frac{\lambda^2}{\Delta nL}. \tag{5.7}$$

It is clear that FSR of the interfering spectrum is inversely proportional to both the mode index difference Δn and the length of the MMF L. FSR can be found about 0.57 nm from

Fig. 5.17, and the length L of the MMF is about 22 cm in our experiment. Thus the mode index difference of the two interfering modes Δn can be estimated to have the order of 10^{-2}, which is at least 10 times larger than those of the MMFs used in [9, 11, 12]. In other words, our proposed sensor can be made at least 10 times smaller than the sensors above, provided that all the sensors have the same wavelength spacing. This feature indicates that the proposed MMF has the potential to be used as sensing heads to reduce the configuration size in the practical application.

From Eq. (5.6), the peak of the spectrum at 1544 nm can be described as

$$I_{\lambda=1554} = I_1 \left(1 + \sqrt{I_2/I_1}\right)^2, \tag{5.8}$$

determined by the power ratio of the two modes and the power of the fundamental mode. The lateral force applied to the MMF will lead to the deformation of the MMF, which must result in the power losses of all the modes. The higher-order mode will experience more power loss than the lower-order mode; therefore, the intensity ratio I_2/I_1 is reduced. Hence, the power P_1 measured by PM1 decreases when the lateral force increases. In addition, the lateral force is applied to a short section of MMF producing negligible longitudinal strain, thus the phase of the interferometer remains almost constant [17]. These features can be used to realize lateral force measurement by monitoring the power changes instead of the spectrum variations.

5.4.2 Experiment and Discussion

As shown in Fig. 5.16, a core-offset MMF interferometer sensor with the MMF length of about 22 cm is fabricated. The extinction ratio reaches 9 dB, as shown in Fig. 5.17. A section of MMF identical to the sensing MMF is used as a supporting fiber. In order to avoid the rotation of the MMF, the interferometer is supported by two fiber holders placed on an optical table. Both of the MMFs are fixed between two aluminum flakes with smooth surfaces. The width of the aluminum flake is about 1 cm. With increasing lateral forces applied to the MMF, the extinction ratio decreases, while the interference phase remains constant, as shown in Fig. 5.18. Since the maximum at 1544 nm on the spectrum also decreases, the power passed through the MMF reduces; therefore, the power measured by PM1 decreases. Thus, the MMF interferometer also serves as a filter. Fig. 5.19 shows the power ratio (P_1/P_2) changes as a function of the lateral force. P_2 was used as a reference to eliminate any power fluctuation from the optical source. The power ratio variation has a good linear relationship with respect to the applied lateral force. This is different from the result reported in Ref. [17], where the extinction ratio has a quadratic behavior with respect to the lateral force. In fact, the experiment data in Ref. [17] can also be fitted as a first-order exponential function within the operating range, but having a more complicated

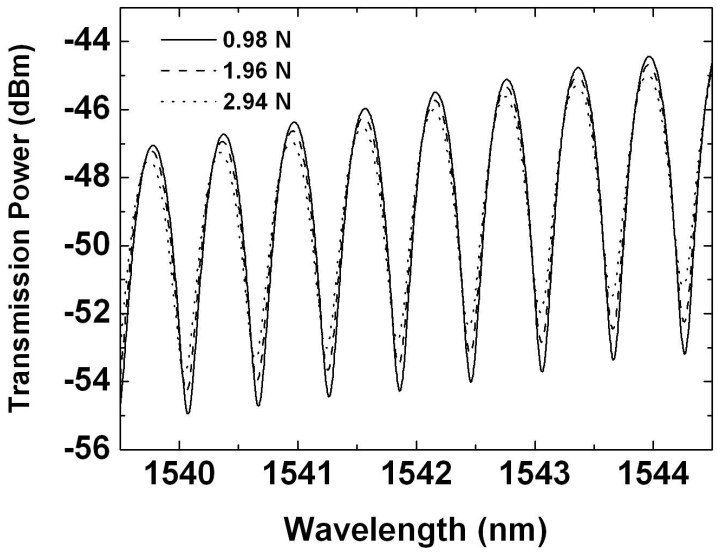

Figure 5.18: Transmission spectra under different lateral forces.

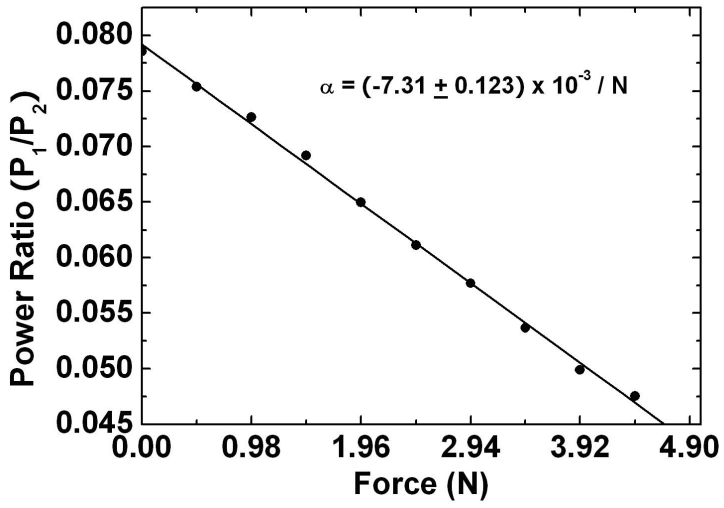

Figure 5.19: Power ratio change as a function of applied lateral force.

appearance. Thus, the linear relationship is reasonable in the present case where the MMF interferometer acts as a filter, because the power changes are measured in μW instead of the extinction ratio measured in dB [17].

In order to avoid breaking the MMF, the force range is controlled in $0 - 4.5$ N. This range can be increased by encapsulating the sensor head in materials with high Young's modulus for practical applications. Moreover, if there is an ambient temperature change, the spectrum of the interferometer has a red shift, which influences the sensing results. This problem may be overcomed by encapsulating the sensing head in temperature compensation materials. In addition, the tunable laser source in our experiment can be changed to other simple sources to further reduce the cost.

5.5 High-Temperature Measurement

A miniature high-sensitivity, high-temperature fiber sensor with an interferometer based on a bare small-core-diameter MMF is reported. The sensing head has a SMF-MMF configuration formed by a 4-mm long bare MMF with one end directly spliced to the SMF and the other end cleaved. Due to the large mode index difference and high thermo-optic coefficient induced by two dominant interfering modes, a miniature high-temperature fiber sensor with a high sensitivity of 68.6 pm/°C is obtained by monitoring the wavelength shift of the interference spectrum. This type of sensor has the features of small size, high sensitivity, high stability, simple structure, and low cost.

5.5.1 Experiment Setup and Principle

Fig. 5.20 shows the schematic diagram of the experimental setup. The temperature is controlled by a tube furnace (Thermolyne type 21100). The temperature of the fiber sensor is measured by a type-K thermocouple, which is connected to a digital thermometer. The sensor head is attached to the thermocouple, and both of them are inserted into the tube furnace. A C-band BBS with an amplified spontaneous emission spectrum centered at 1550 nm is used as the light source. The interference spectra are monitored by an OSA. The sensing head, as shown in the inset of Fig. 5.20, is fabricated by connecting a 4-mm long bare MMF to a standard communications SMF, which serves as an interferometer based on intermode interference. The MMF has a core/cladding diameter of 1.9/115.7 $\mu\varepsilon$, a large dispersion parameter of -270 ps/nm/km at 1550 nm, and a cutoff wavelength of 1663 nm which was originally designed for dispersion compensation applications. The free end of the MMF is cleaved to reflect the light back to the MMF. The emitted light of the BBS propagates to the end surface of the sensing head through a 3-dB coupler, and then the reflected light propagates to the OSA through the coupler again. The fundamental mode

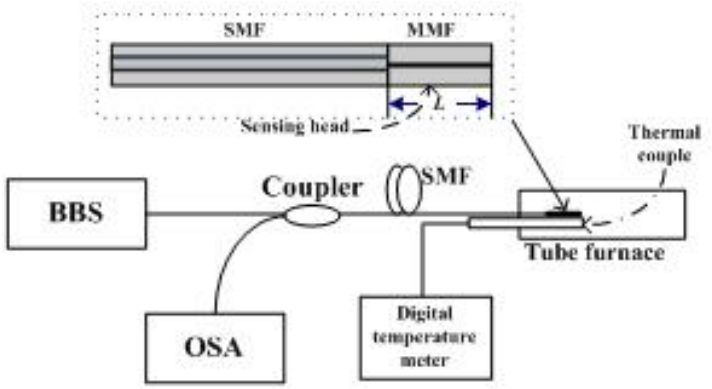

Figure 5.20: Schematic diagram of the experiment setup (Inset shows structure of the sensing head).

that propagates along the SMF will couple into the MMF and excite different interfering modes at the SMF-MMF splice point. After Reflecting back to the MMF by the cleaved end surface of the MMF, these modes will interfere and recouple into the SMF at the MMF-SMF splice point.

Fig. 5.21 shows the measured reflectivity spectrum of the interferometer and the transmission power spectrum of the applied BBS. The interference can be approximately considered to be produced by two dominant modes, which indicates that other weak modes carry much less powers and slightly modulate the interference pattern. The phase difference between the two dominant modes after propagating through the MMF can be written as $\varphi_m = 4\pi\Delta nL/\lambda$, where $\Delta n = n_1 - n_2$ is the mode index difference of the two dominant modes, and n_1, n_2 are the mode indices of the two modes respectively; λ is the signal wavelength in vacuum and L is the length of the MMF. The interference condition of the two dominant modes can be given by

$$\varphi_m = \frac{4\pi\Delta nL}{\lambda} = N2\pi(N \text{ is an integer}). \tag{5.9}$$

When ambient temperature changes, the mode index difference Δn and the fiber length L will change accordingly, and thus the interference spectrum will have a wavelength shift $\Delta\lambda$. According to Eq. (5.9) the relative wavelength shift $\Delta\lambda/\lambda$ caused by a temperature change ΔT can be expressed as

$$\frac{\Delta\lambda}{\lambda} \approx (\alpha + \xi)\Delta T, \tag{5.10}$$

where $\alpha = dL/LdT$ is the thermal expansion coefficient of the MMF material, and $\xi = d(\Delta n)/(\Delta n)dT$ is the thermo-optic coefficient induced by the two interference modes in

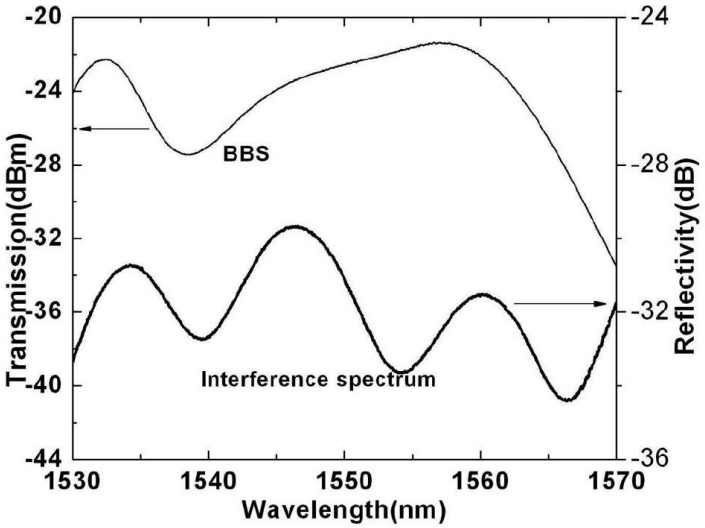

Figure 5.21: Interference spectrum of the MMF interferometer.

the MMF material. The FSR of the interfering spectrum can be approximately given by

$$FSR = \frac{\lambda^2}{2\Delta n L}. \tag{5.11}$$

It can be seen that the FSR is inversely proportional to both the mode index difference Δn and the length of the MMF L. According to Eq. (5.11) and Fig. 5.21, the mode index difference of our proposed MMF interference sensor is about 2.1×10^{-2}. However, the mode index difference of the high-temperature 105/125 μm MMF interference sensor [11] is about 9.6×10^{-4}, and that of the 100/140 μm MMF temperature sensor [9] is only about 2.5×10^{-4}. The mode index difference of our proposed interference sensor is about 22 and 84 times larger than that of the two temperature sensors in [9, 11]. In other words, our proposed sensor can be made by 22 or 84 times smaller than the two sensors above, considering that all the sensors have the same FSR. On the other hand, sensor resolution is a very important parameter and is dependent on wavelength measurement errors that are determined by the resolution of OSA and the bandwidth of the resonance peak. For a fixed value of L, a large value of Δn gives rise to a small FSR and consequently a small bandwidth of the resonance peak, which will be beneficial to the sensor resolution. Therefore, the proposed 1.9/115.7 μm MMF interference sensor with a large mode index difference can be miniaturized readily with a high-temperature resolution. The parameters of the refractive indices of the core and the cladding of the MMF are not known for us. The large mode index difference of the MMF interferometer is attributed to the special design of the MMF.

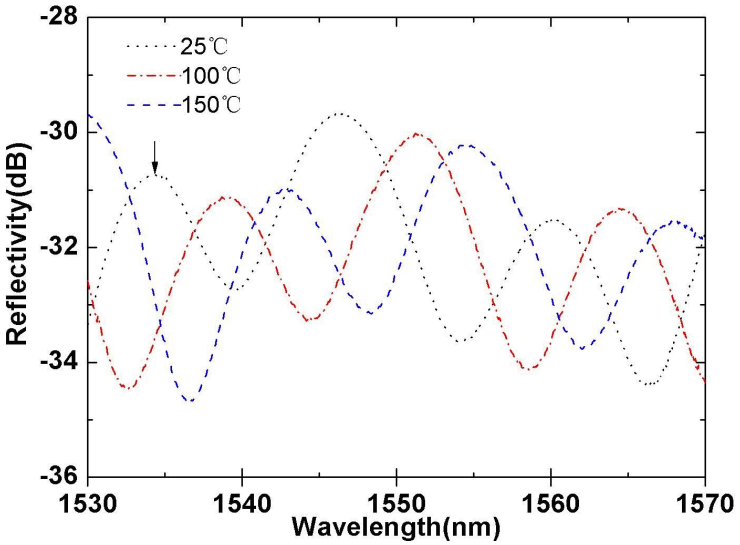

Figure 5.22: Wavelength shifts of the interference spectrum at different temperatures.

5.5.2 Experiment Results and Discussion

The OSA with a resolution of 0.06 nm is used to measure the transmission spectrum of the interferometer. When the temperature increases, the MMF interference spectrum has a red shift while the spectrum almost keeps the same pattern, as shown in Fig. 5.22. To monitor a broad wavelength shift, we measure the wavelength variation of the point at the arrow shown in Fig. 5.22, starting with the wavelength of 1534.28 nm at a room temperature of 25 °C. Fig. 5.23 shows the measured relationship between the wavelength and the temperature. It can be seen that there is a good linear relationship between the wavelength and temperature change. Within the temperature range of $25 - 600$ °C, the temperature sensitivity reaches 68.6 pm/°C. Compared with the high-temperature MMF-based sensors [11], the proposed high-temperature sensor has higher sensitivity, which is mainly because of the higher thermo-optic coefficient. The thermal expansion coefficient is generally lower by 2 orders of magnitude than the thermo-optic coefficient for the optical fiber; ignoring the thermal expansion coefficient, the thermo-optic coefficient of the MMF used in our experiment is about 4.4×10^{-5},while that of the MMF in [11] is about 9.7×10^{-6}. As the FSR of the proposed fiber sensor is much smaller than the bandwidth of the available BBS, the length of the sensing head can be shortened further to obtain ultra compact sensing heads. To test the influence of the ambient disturbance on the sensor, we keep the sensing head under several fixed temperatures, and we find that the interference spectrum does not change and has high stability under a fixed temperature, which is attributed to the small size of the sensing head. In addition, it can be seen that a cleaved surface used as a reflection mirror provides low reflection. However, the low reflection does not affect our

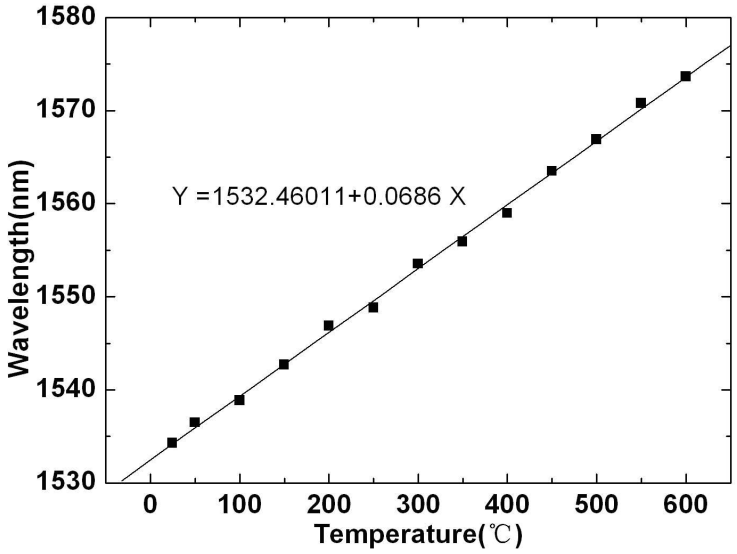

Figure 5.23: Measured relationship between the wavelength and the temperature.

measurement accuracy, since we measure the wavelength shift of the spectrum, although the reflectivity can be increased by coating the MMF end surface with proper materials.

5.6 Conclusion

A simple core-offset MMF interferometer force sensing mechanism has been presented and demonstrated experimentally. The MMF-based interferometer can be obtained by misaligning a fused cross section between the SMF and MMF. The advantages of the sensor include temperature- and phase-independency, high extinction ratio sensitivity, low cost, and simple structure.

Due to the little crosstalk between the extinction ratio change induced by the transverse force and the wavelength shift induced by the longitudinal strain variations or temperature variations, the MMF lateral force sensor could be used to realize simultaneous measurement of transverse and longitudinal strain or simultaneous measurement of transverse strain and temperature.

In order to void using OSAs, the improved lateral force sensor based on a core offset MMF interferometer is presented and demonstrated experimentally. Intensity-based interrogation method is used instead of monitoring the extinction ratio change of the spectrum. The proposed sensor has the advantages of simple structure and low cost.

Finally, a miniature high-temperature fiber sensor with a bare small-core-diameter

MMF-based interferometer has been proposed and demonstrated experimentally. Experimental results show that the MMF interference temperature sensor with an only 4-mm long bare MMF can be operated with high sensitivity of 68.6 pm/°C within the temperature measurement range of $25 - 600$ °C. This type of sensor has the features of small size, high sensitivity, high stability, simple structure, and low cost. It is expected to be applied in smart and practical fiber high-temperature sensing.

Chapter 6

Temperature Insensitive All-Fiber Compact Polarization-Maintaining Photonic Crystal Fiber Based Interferometer and Its Application in Fiber Sensors

A novel temperature insensitive all-fiber compact polarization-maintaining photonic crystal fiber (PMPCF) based interferometer is presented. The coupling between the PMPCF and single-mode fiber (SMF) is investigated experimentally. With an all-fiber compact SMF-PMPCF-SMF structure, the cladding modes propagating in the PMPCF can be effectively excited by core offsetting one splice between the PMPCF and SMF. With the increase of the core-offset, the interference depth of the interference pattern enlarges accordingly. Under a suitable core-offset, the PMPCF based interferometer with high interference depth can be obtained. Moreover, the proposed sensor is temperature insensitive due to the ultra-low thermal characteristics of the PMPCF. We also demonstrate its applications in strain and refractive index measurement. The sensor has the advantages of small size, simple and compact all-fiber structure, high sensitivity, and temperature insensitiveness.

6.1 Introduction

Due to the advantages of compact structure and low cost, modal interferometer based sensors have attracted much interest. Several multimode fiber (MMF) based modal interferometer sensors with single-mode fiber (SMF)-MMF-SMF [1, 2, 3] and MMF-SMF-MMF

[4] structures, have been reported recently. However, when they are used for sensing other measurands such as longitudinal strain, the high thermal response may cause serious cross-sensitivity effects and reduce the measurement accuracy.

With the commercialization of the polarization-maintaining photonic crystal fibers (PMPCFs), the applications of PMPCF in optical filters and sensors have attracted intensive research interests. Zhao *et al.* reported a temperature insensitive PMPCF based optical fiber Sagnac interferometers (OFSI) [5]. Dong *et al.* used this type of OFSI as a temperature-insensitive strain sensor [6]. To construct an all-fiber OFSI, in addition to the polarization-maintaining fiber, other components, such as a 3-dB coupler and a polarization controller (PC), generally have to be applied, which may lead to a complex structure and high cost. Moreover, when the OFSI is used as filters and sensors [5, 6, 7, 8, 9], any disturbance on the components that form the OFSI may lead to the change of the transmission spectrum of the OFSI, which may limit its practical applications.

In this chapter, we present a novel all-fiber PMPCF based modal interferometer that has the unique features of small size, simple and compact structure, and temperature-insensitiveness. We investigate the coupling between the PMPCF and SMF experimentally in detail. With an all-fiber compact SMF-PMPCF-SMF structure, by core offsetting one splice between the PMPCF and SMF, the cladding modes propagating in the PMPCF can be effectively excited. As a result, modal interferences occur due to the coupling between the core mode and cladding modes. With the increase of the core-offset, the interference depth of the interference pattern enlarges accordingly. The PMPCF based interferometer with high interference depth can be obtained under a suitable core-offset. Moreover, the proposed interferometer is temperature insensitive due to the ultra-low thermal characteristics of the PMPCF, which makes it a suitable candidate for the applications of temperature insensitive fiber filters and sensors. By using it as a strain sensor, a strain sensitivity of 1.84 pm/$\mu\varepsilon$ is obtained, which is considerably higher than that of 0.23 pm/$\mu\varepsilon$ for the OFSI based sensor [6]. It also has the potential to be used as a refractive index (RI) sensor to measure the RI in a wide measurement range. For the ordinary PMPCF based OFSI, the interference is constructed by two core modes (i.e., x- and y-polarized modes). Here, based on an all-fiber SMF-PMPCF-SMF structure, we focus on using the core-offset method to excite the cladding modes of the PMPCF to produce the interference with core mode and the cladding modes. Note that we make use of the ultra-low thermal characteristics of the specially designed PMPCF, other than its polarization characteristics, to develop an all-fiber sensor featured with small size, compact and simple structure, as well as temperature insensitiveness.

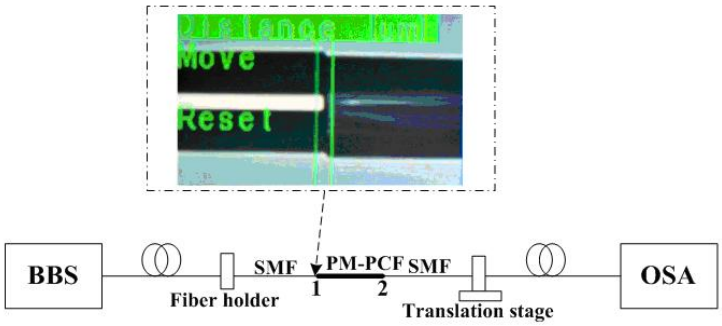

Figure 6.1: Schematic diagram of the experimental setup.

6.2 Principle

6.2.1 Structure of the PMPCF Interferometer and the Coupling Between the PMPCF and SMF

The schematic diagram of the experimental setup is shown in Fig. 6.1. When the mismatch between the cores of two kinds of fibers with different core diameters is introduced, high-order modes can be excited [1, 2, 10, 11, 12]. Here, an all-fiber compact SMF-PMPCF-SMF structure is used to construct the interferometer with splice Point 2 being fused without core-offset and a slight core-offset at splice Point 1. The inset in Fig. 6.1 is a core-offset photograph of the splice Point 1. The PMPCF used in our experiment is fabricated by Blaze-Photonics Com., and it has the same parameters as described in [5, 6]. A C-band broadband source (BBS) with amplified spontaneous emission (ASE) spectrum centered at 1550 nm is used as the light source. The transmission spectrum of the interferometer is measured by an OSA of Agilent 86142B. Figs. 6.2 and 6.3 show the core-offset dependent characteristics of the 7-mm and 11-mm PMPCF based interferometers under different core-offsets. It can be seen that without the core-offset there is no interference. However, when the core-offset is introduced, the interference depth increases with the enlargement of the core-offset, but the insertion loss increases accordingly. A 20-dB interference depth can be obtained with the 7-mm PMPCF based interferometer. Comparing Fig. 6.2 with 6.3, it can also be seen that the longer length PMPCF based interferometer has smaller FSR.

6.2.2 Sensing Principle of Temperature and Strain

When only one dominant cladding mode is considered, the resonance condition (the dip on the spectrum) for the interference can be given by

$$2\pi BL/\lambda = N\pi, \tag{6.1}$$

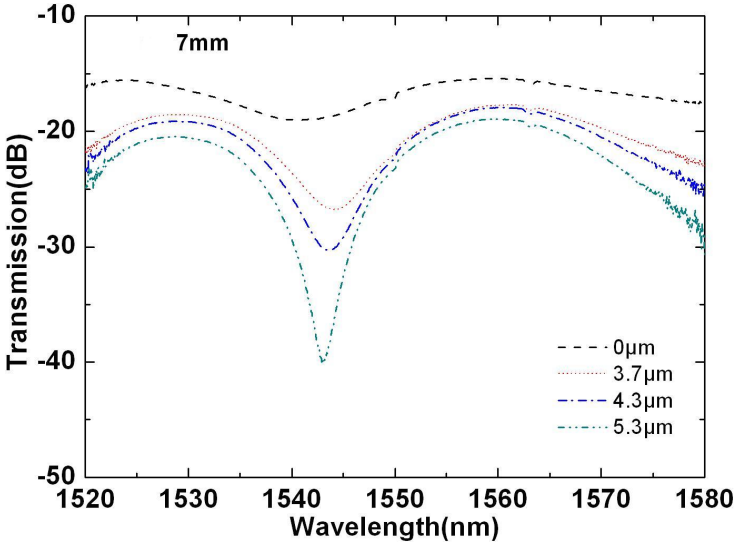

Figure 6.2: Coupling between the 7-mm PMPCF and the SMF under different core-offsets.

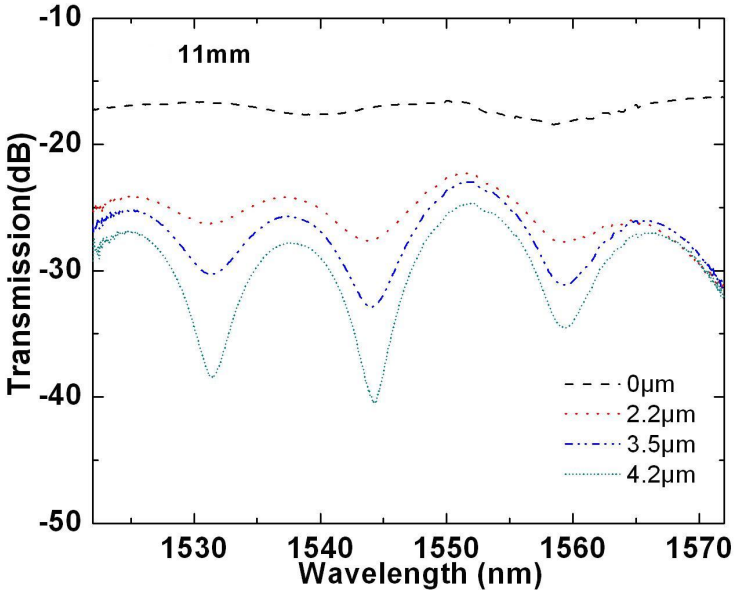

Figure 6.3: Coupling between the 11-mm PMPCF and the SMF under different core-offsets.

where $N = 1, 2, 3, ...$, $B = n_1 - n_2$, n_1 and n_2 are the effective refractive indices of the core and cladding modes; L is the length of the PMPCF, and λ is the wavelength of light in vacuum. The FSR of the interference pattern is given by $FSR \approx \lambda^2/BL$.

When a strain ε is applied to the PMPCF or ambient temperature changes, B and L will have corresponding changes of ΔB ($\Delta B << B$) and ΔL ($\Delta L << L$), thus the transmission spectrum will have a wavelength shift of $\Delta\lambda$. Since the core and cladding modes propagate in different waveguide structures in the PMPCF, the strain and temperature must affect the two modes in different manner. We denote the effective photoelastic constants by p_{e1} and p_{e2}, and the thermo-optic coefficients by ξ_1 and ξ_2 for the two modes, respectively. ΔB and ΔL induced by the strain can be expressed as $\Delta B = (p_{e1}n_1 - p_{e2}n_2)\varepsilon$ and $\Delta L = L\varepsilon$. ΔB and ΔL induced by the temperature variation ΔT can be given by $\Delta B = (\xi_1 n_1 - \xi_2 n_2)\Delta T$ and $\Delta L = \alpha L \Delta T$ (α is the thermal expansion coefficient of the PMPCF). Therefore, the wavelength shift can be obtained as

$$\Delta\lambda \approx [(1 + p_e)\varepsilon + (\alpha + \xi)\Delta T]\lambda, \tag{6.2}$$

where $p_e = (p_{e1}n_1 - p_{e2}n_2)/B$, is a constant that describes the strain-induced variation of the effective index difference of the two modes, and $\xi = (\xi_1 n_1 - \xi_2 n_2)/B$, is a constant that describes the thermal-induced variation of the effective index difference of the two modes.

6.3 Experiment results and discussions

We use the 7-mm PMPCF-based interferometer to demonstrate the temperature, strain and RI sensing. The OSA with a resolution of 0.06 nm is used to measure the transmission spectrum of the interferometer. Due to the mismatch of the mode field and numerical aperture between the PMPCF and the SMF, a large splicing loss is introduced. The total loss of the two splicing points without core-offset is about 7 dB while that with core-offset reaches about 8.5 dB. However, the high insertion loss does not affect our measurement accuracy since we measure the wavelength shift of the spectrum.

6.3.1 Interference Spectrum Response to Temperature

Under the 0.06 nm resolution of the OSA, the interference pattern keeps almost unchanged and the measured transmission dips under different temperatures are almost overlapped when the temperature changes from 25 °C to 60 °C, as shown in Fig. 6.4. The ultra-low thermal characteristic of the sensor is attributed to the low thermal expansion coefficient α and low effective thermo-optic coefficient ξ of the PMPCF. Experimental results show that when the temperature is over 60 °C, a slight shift for the transmission dip can be

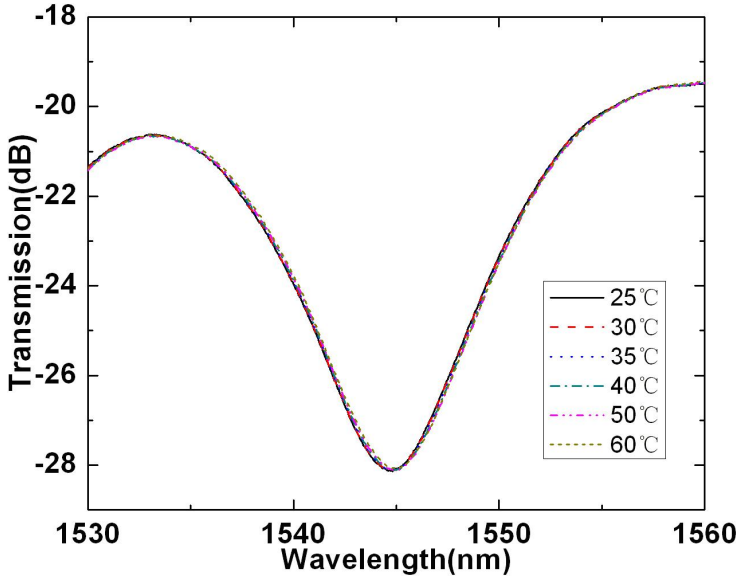

Figure 6.4: Measured transmission spectra under different temperatures.

observed. So the temperature influence on the interferometer can be neglected when it is operated in normal environmental condition without very large temperature variations.

6.3.2 Interference Spectrum Response to Strain

With the increase of the applied strain, the transmission spectrum has a corresponding blue shift, as shown in Fig. 6.5. By measuring the wavelength shift of the transmission minimum at 1544.74 nm against the applied strain, a good linear relationship between the wavelength shift and strain is obtained, as shown in Fig. 6.6; the sensitivity reaches -1.84 pm/$\mu\varepsilon$. The proposed sensor shows a considerably higher sensitivity than the OFSI based sensor (0.23 pm/$\mu\varepsilon$) [6]. The applied strain is controlled in the range of $0 - 1044.4$ $\mu\varepsilon$. The strain resolution is about 32.6 $\mu\varepsilon$, which is limited by the 0.06 nm resolution of the OSA. The operational strain range of the sensor can be increased by encapsulating the sensing head in materials with high Young's modulus for practical applications.

6.3.3 Interference Spectrum Response to RI

Another unique feature of the interferometer is its high sensitivity to surrounding RI. Fig. 6.7 shows the measured transmission spectra under different RIs. By measuring the transmission peak shift, the transmission spectrum response to RI in wavelength shift is obtained. It can be seen that the responses of the sensor with RI in the ranges of $1.36-1.428$

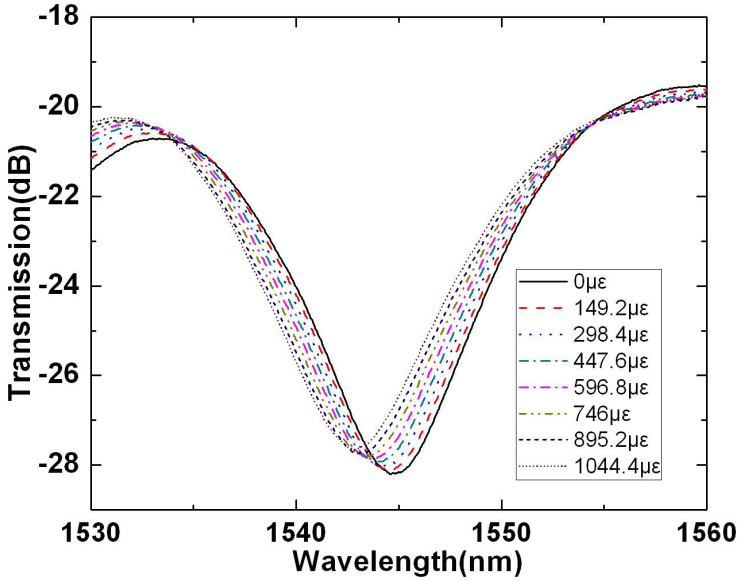

Figure 6.5: Measured transmission spectra under different applied strains.

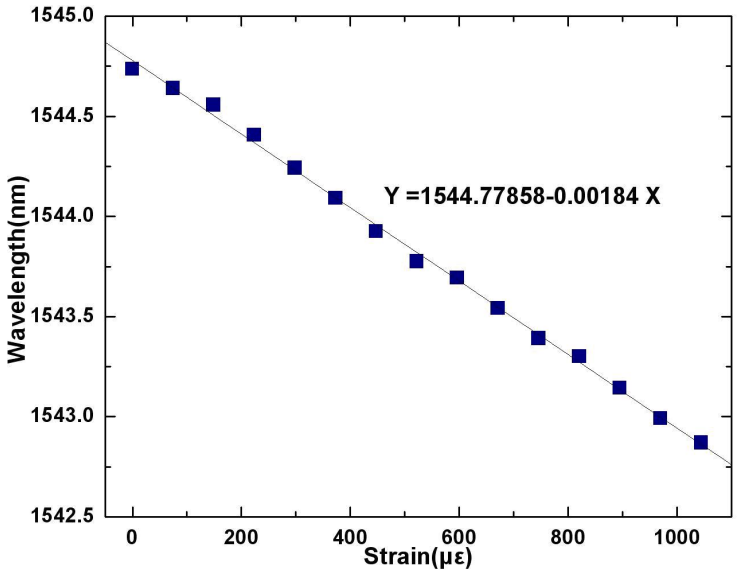

Figure 6.6: Wavelength shift of the transmission minimum at 1544.74 nm against the applied strain.

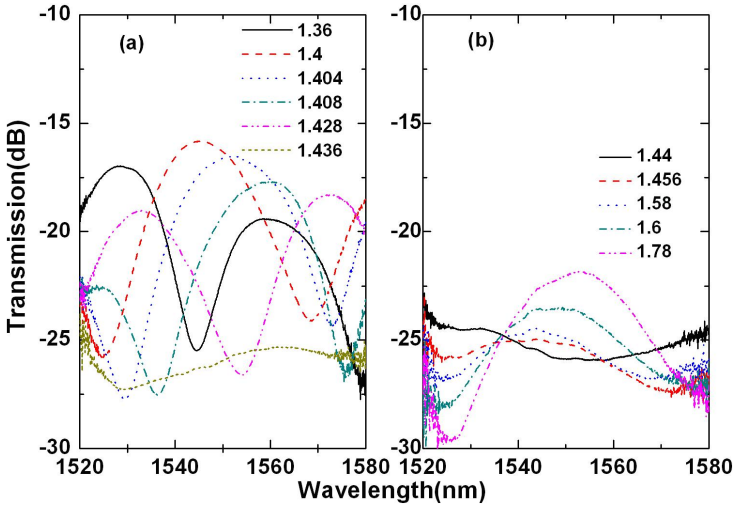

Figure 6.7: Measured transmission spectra under different refractive indices.

and $1.456 - 1.78$ are very different. In RI range of $1.36 - 1.428$, the transmission spectrum has a large red shift (42.824 nm) as the RI increases. In the RI range of $1.456 - 1.78$, red shift also occurs in the transmission spectrum, but the spectrum only shifts 8.883 nm, much less than that in RI range of $1.36 - 1.428$. It can be seen that the interference pattern disappears as the RI locates in the range of $1.436 - 1.44$. This is because the cladding modes are cut-off and propagate out of the cladding of the PMPCF when the ambient RI is close to that of the cladding. This feature of the proposed sensor could have a potential for the application to measure RI. In normal environmental condition without large temperature variations, the proposed strain and RI sensor is temperature insensitive. It should be noted that the characteristics of high sensitivity and temperature insensitiveness also make the RI sensor have potential applications in bio-sensing.

6.4 Conclusion

We present a novel temperature insensitive all-fiber compact PMPCF based interferometer. The coupling between the PMPCF and SMF is investigated experimentally. With an all-fiber compact SMF-PMPCF-SMF structure, a short length interferometer with high interference depth of the interference pattern can be obtained by core-offsetting one splice between the PMPCF and SMF. The sensor is temperature insensitive due to the ultra-low thermal characteristics of the PMPCF. The interferometer based strain and RI sensors have the advantages of small size, simple and compact all fiber structure, high sensitivity, and temperature insensitiveness.

Chapter 7

Future Work: Pulsed Fiber Lasers and Fully Distributed Fiber Sensors Based on Brillouin Scattering

One of the most important advantages of optical fiber sensors is their capability of integrating a large number of passive optical sensors or sensing regions within a single fiber. Because of this superior advantage of distributed sensing, optical fiber sensors have already appeared to have a distinct edge over the competition with the conventional sensors. Such sensors have already been commercialized and penetrated into the markets for the applications of oil and gas pipeline monitoring, power line monitoring, health monitoring of bridges, dams, buildings, aircrafts, wind turbines, etc. (failure of such structures may result in the losses of the human lives, millions of dollars loss, or severe environmental pollution, etc.).

As introduced in the first chapter, there are two types of distributed optical fiber sensors: quasi-distributed optical fiber sensors and fully distributed optical fiber sensors. Quasi-distributed optical fiber sensors usually refer to multiplexing point sensors to form a sensing mesh to measure the parameters of many separate points in the space simultaneously. However, point sensors' localized nature only gives incomplete information about the health of the structure, since the locations over which a strain has been accumulated, or the position that has been deformed, are usually unknown [1]. Fully distributed fiber sensors, which are based on light scattering in an optical fiber, could realize this purpose by not only measuring the amount of the strain or other parameters but also telling where the change happens. Therefore, this kind of sensors provide an excellent opportunity for structural-health monitoring of civil-engineering structures by allowing measurements to be taken along the fiber rather than at discrete points. One of the most successful techniques called Brillouin Optical Time Domain Analysis (BOTDA) [2, 3, 4] based on the

interaction between pulsed and continuous light waves counterpropagating in an optical fiber which enhances the Brillouin backscattering intensity (compared to Brillouin Optical Time Domain Reflectometry where only one pulsed source is used) to realize long distance distributed sensing has already found its way toward the "real-world" applications, since the spatial resolution has been achieved on the order of centimeter with high temperature and strain accuracies [1, 5, 6, 7, 8].

However, the problem of cross sensitivity, when an optical fiber sensor is sensitive to both strain and temperature, also exists for distributed optical fiber sensors. This cross sensitivity would introduce large errors when monitoring strain which is in general an important factor for health monitoring of massive structures. An effective method to solve this problem is to detect two independent physical parameters which have different sensitivities to temperature and strain [9] as introduced in the previous chapters. Since the conventional BOTDA system is to monitor the Brillouin frequency shift (BFS) which is sensitive to both the temperature and strain, another factor has to be found and monitored for temperature and strain discrimination. Many efforts have been made toward this purpose, such as using a pair of optical fibers with different refractive indices [10], monitoring two acoustic resonance peaks at different orders of Brillouin gain spectrum [11], measuring the power and the Brillouin frequency pair [12]. However, the above schemes have their own drawbacks: the sensing head with two fibers makes the system complex, one of the two Brillouin peaks has low signal-to-noise ratio, and the power measurement introduces errors due to the fluctuation; and the accuracies of these schemes are not sufficient [13].

Recently, the discrimination of temperature and strain could be achieved using a polarization-maintaining fiber (PMF) by evaluating the spectrum of stimulated Brillouin scattering (SBS) and that of the Brillouin dynamic grating (BDG) generated in SBS to obtain two independent responses to strain and temperature [13]. A BDG refers to a dynamic acoustic grating generated in SBS. If we consider the case in a PMF, an acoustic phonon generated by SBS between two counterpropagating writing beams of one polarization is used as a tunable and dynamic grating for the orthogonally polarized reading beam at different wavelengths satisfying the phase-matching condition. The reflected probe wave experiences an ordinary Brillouin shift, and the optical frequency difference between the writing and the reading beams is determined by the birefringence of the PMF. The BDG spectrum shift is also sensitive to temperature and strain but with different sensitivities from those of the BFS, so that the BDG spectrum shift could be used as a second factor for temperature and strain discrimination. This method provides a better way compared to the above reports [5, 10, 11, 12] to discriminate temperature and strain using only one piece of fiber with high temperature and strain resolutions; much higher resolution could be achieved. Note that after the BDG was first introduced in a PMF in 2008 [14], many results have been reported on this topic for different applications [15, 16, 17, 18]. More recently, Dong *et al.* reported a high spatial resolution distributed sensor for temperature

and strain discrimination by generating the BDG with two short pulses inside the PMF [19]. However, detailed physical description and the theoretical analysis of the BDG were missing in all the above reports [14, 15, 16, 17, 18, 19]. In the reported experiment results, the BDG spectrum has a Gaussian shape [13, 19], and its bandwidth is much wider than Brillouin linewidth; moreover, the distorted spectrum [14] and even a two-peak structure [18] have been observed. Although a simple modal based on the consideration of the BDG as a moving FBG was developed [20], and a simple explanation that is because of the large non-uniform birefringence in the PMF was mentioned [18], a comprehensive physical and mathematical description is very necessary. In addition, in order to use this BDG technique to design high performance distributed fiber sensors, theoretical analysis and guidance are indispensable for sensor characteristic optimization.

Future work could start with this theoretical work by solving the five coupled wave equations (four are for light waves; the other one is for acoustic wave) to give a detailed investigation on the property of the BDG. Then, with the guidance of the theoretical analysis, fully distributed fiber sensors for temperature and strain discrimination with high spatial resolution could be designed and developed with the BDG technique. The high spatial resolution could be achieved by generating a short BDG inside the fiber. One recent report on this purpose used two counterpropagating writing pulses of 2 ns duration. The length of the BDG was about 20 cm, which corresponds to 20 cm spatial resolution. In order to further improve the resolution, a simple idea is to build a laser source with shorter pulse duration (e.g., 200 ps corresponds to 2 cm resolution). Admittedly, optical pulses with nanosecond duration could be achieved by modulating the continuous wave laser source. When shorter pulses (picosecond range) are needed, Q-switched and mode-locked lasers are necessary. In the following two sections, several schemes of passively Q-switched and mode-locked erbium-doped fiber lasers are presented with single-walled carbon nanotubes as saturable absorbers. They are expected to have the potential to be used as the source for distributed sensing. In addition, when studying short pulse fiber lasers, many nonlinear effects need to be considered. This would in turn help us design and develop better sensing systems. In the last section, Section 7.3, a summary of the future work will be given.

7.1 Tunable Passively Q-Switched Erbium-Doped Fiber Laser with Single-Walled Carbon Nanotubes as a Saturable Absorber

7.1.1 Introduction

Q-switched erbium-doped fiber lasers (EDFLs) have attracted intensive attention for their wide applications in fields such as communications, reflectometry, fiber optical sensing, etc. Compared to actively Q-switched fiber lasers, passively Q-switched ones have the advantages of compactness and simplicity of design. Many kinds of saturable absorbers (SAs) have been used to achieve passive Q-switching of the EDFLs, such as the transition metal-doped crystals that include Co^{+2}:ZnSe [21], Co^{+2}:ZnS [22], Cr^{+2}:ZnSe [23], Co^{+2}:$MgAl_2O_4$ [23], etc., and the semiconductor quantum-well structures that comprise InGaAs-InP [24], AlGaInAs [25], etc. However, extra mirrors, lens, or U-bench units have to be inserted into the laser cavity, which may increase the complexity and the insertion loss of the configuration.

In order to overcome these limitations, single-walled carbon nanotubes (SWNTs) can be used as SAs because of their good compatibility with optical fibers. Besides, they have the advantages of low saturation intensity, subpicosecond recovery time, wide operating bandwidth, and mechanical and environmental robustness. Recently, different techniques have been used to integrate SWNTs into fiber devices to construct SAs, such as synthesizing SWNTs directly onto quartz substrates [26], depositing SWNTs onto tapered fibers [27] or D-shaped fibers [28], making SWNT-polycarbonate composites [29], and optically driven depositing SWNTs on the ends of optical fibers [30]. However, most of the reports are focusing on mode-locking with a ring cavity. Q-switching was also mentioned in [26] and [27], but no detailed demonstration nor tunability was reported. In this section, by introducing a fiber Bragg grating (FBG) serving as a narrowband external mirror of the ring cavity, stable all-fiber passively Q-switched EDFL is achieved and studied in detail. The EDFL can be tuned simply by applying axial strain to the FBG. The SAs are constructed by optically driven depositing commercially available SWNTs on the end of a fiber connector as described in [30], since this method is simple and inexpensive compared to other techniques [26, 27, 28, 29]. The self-mode-locking effect is also observed, and it could be suppressed by splicing an extra unpumped erbium-doped fiber (EDF) into the ring cavity.

However, the pulse duration obtained with this Q-switched technique is pretty long, on the order of μs due to the long cavity length. Although the pulse width could be shortened in principle by using highly doped active fiber to decrease the length of the cavity, the generation of sub-nanosecond pulses is not easy. In Section 7.2, erbium-doped

fiber lasers based on mode-locking technique will be presented. Sub-nanosecond pulse could be generated with a normal dispersion cavity. This has the potential to be used as the optical source for fully distributed fiber sensor systems.

7.1.2 Experiment Setup

A homogeneous solution of nanotubes is prepared by mixing approximately 0.5 mg of SWNTs (diameter of $1-2$ nm) with 10 ml of ethanol and then ultrasonicating for $10-20$ min. The optical power output of a fixed connection/angled physical contact (FC/APC) connector from a 980-nm laser diode is first measured as 7 mW. The connector is then dipped into the solution for around $30-40$ s before being moved out. The optical power is measured again after the ethanol was evaporated completely. The power drops since the SWNTs are deposited on the core of the fiber, and thermophoresis caused by heating due to optical absorption is a likely candidate responsible for the deposition process [30]. This procedure is repeated until the loss of the connector is about 3 dB. The typical scanning electron microscope (SEM) images of the end face of the connector are shown in Figs. 7.1(a)-(c) with different resolutions. The connector with SWNTs is then mated to another clean connector to construct an SA [see Fig. 7.1(d)] that could be easily spliced in the cavity of the fiber laser.

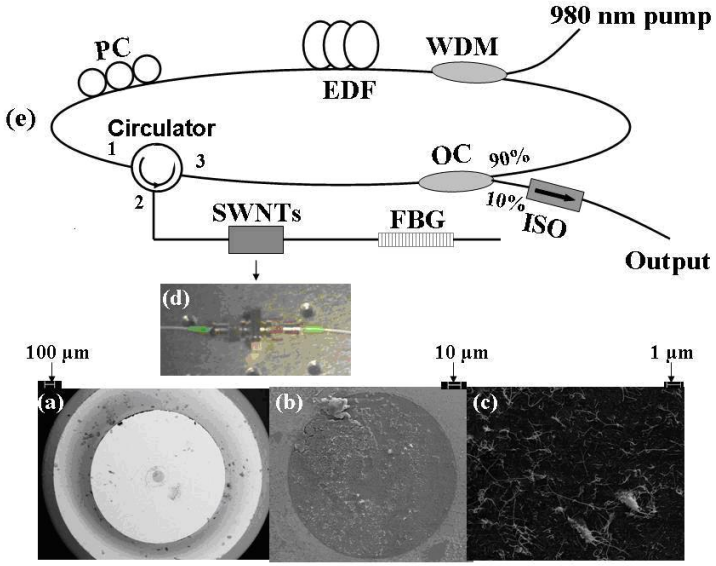

Figure 7.1: SEM images of the connector end deposited with SWNTs with different magnifications (a) ×60, (b) ×1 k, (c) ×10 k. (d) Photo of the SA constructed with the connectors. (e) EDFL configuration.

The Q-switched EDFL configuration is shown in Fig. 7.1(e). The fiber laser is pumped by a 980-nm laser diode through a wavelength division multiplexing (WDM) coupler. A 5-m long single-mode EDF is used as a gain medium. The polarization controller (PC) is utilized for optimization of the laser output. The SA is coupled to the cavity by a circulator which also acts as an isolator to provide unidirectional operation. An FBG, which has a central wavelength of 1554.98 nm, an optical bandwidth of 0.2 nm, and a reflectivity of 99%, serves as an external mirror of the ring cavity. The 10% port of an optical coupler (OC) is used to extract the output power, and an isolator (ISO) is employed to avoid backward reflection. The overall length of the cavity is about 20 m.

7.1.3 Experimental Results and Discussion

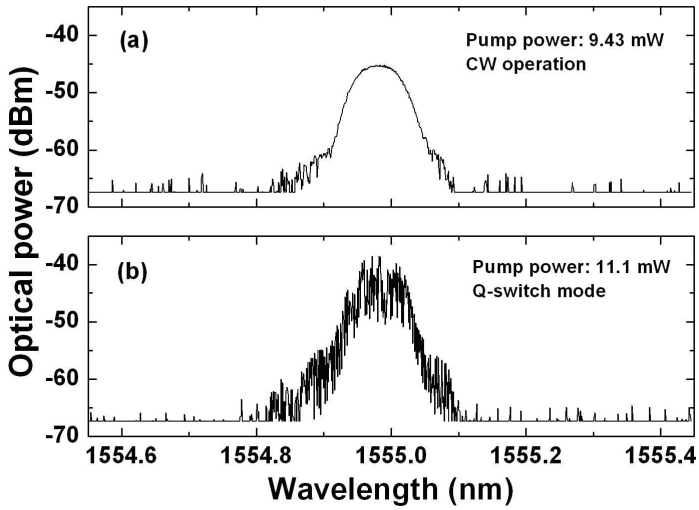

Figure 7.2: Laser output spectrum of (a) CW mode at a pump power of 9.43 mW and (b) Q-switch mode at a pump power of 11.1 mW.

The threshold of continuous-wave (CW) operation of the laser is 9.43 mW at a wavelength of 1554.98 nm. The laser transits to a passive Q-switch mode when the pump power is increased to 11.1 mW. Both the spectra are shown in Fig. 7.2, with a full-width at half-maximum (FWHM) bandwidth of less than 0.15 nm. When Q-switching starts, the spectrum of the laser output shows sideband structure due to multimode oscillation and cavity perturbations. The typical pulse train has a stable repetition rate as shown in Fig. 7.3 (pump power of 29.7 mW), which is measured by a photodetector (PD) with a bandwidth of 100 kHz. The pulse duration (FWHM) in the train is about 7 μs with a peak power of 1.7 mW. The rather long pulse duration is primarily because of the long length of the laser cavity which gives rise to a long cavity lifetime. Note that the pulse duration

could, in principle, be reduced by shortening the length of the cavity, e.g., by using a highly doped EDF of a shorter length. The pulse temporal behavior is further recorded by a faster PD with a bandwidth of 2 GHz. The repetition rate and pulse duration are consistent with those measured by the slower PD, but large amplitude modulation on each Q-switched pulse envelope is observed (red line in the left inset of Fig. 7.3) because of the self-mode-locking effect. The repetition rate of the mode-locked pulses can reach hundreds of megahertz due to higher order harmonics [31]. This self-mode-locking effect could be suppressed by splicing an extra 1-m-long unpumped EDF into the cavity between the SWNTs and the FBG, since the counterpropagating beams in the unpumped EDF form a standing wave that results in periodic spatial hole-burning which could realize lasing mode selection. The suppressed Q-switched pulse recorded by the 2-GHz PD is shown in the right inset of Fig. 7.3. The longer pulse duration is due to the longer cavity length and the absorption induced from the unpumped EDF. Let us mention that the modulation of the pulse envelope is still observed occasionally.

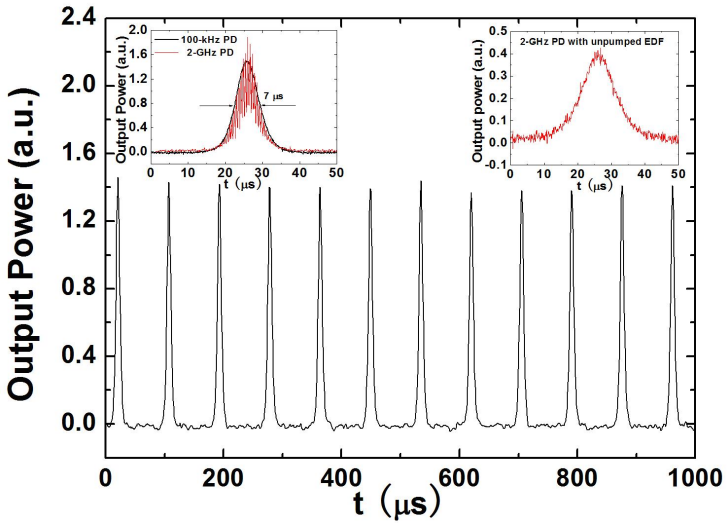

Figure 7.3: Typical oscilloscope trace of the typical laser output at a pump power of 29.7 mW. Left inset: single pulse envelope recorded by 100-kHz PD (black line) and 2-GHz PD (red line). Right inset: single pulse envelope recorded by 2-GHz PD with an extra 1-m long unpumped EDF inserted in the laser cavity.

Fig. 7.4 shows the repetition rate of the Q-switched pulses and the average output power as a function of the pump power. The data is obtained without the extra unpumped EDF. A stable Q-switched mode is observed within the range $11 - 46$ mW of pump power. The pump power is limited within this range to avoid optical power induced thermal damage of the SWNTs. The pulse energy is also found to grow monotonically with the increase of the pump power, since the interpulse period of the proposed Q-switched laser (on the order of

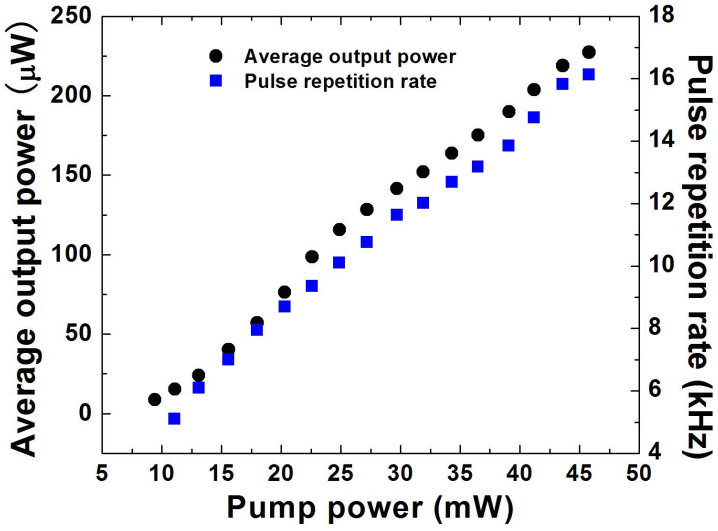

Figure 7.4: Average output power and pulse repetition rate as a function of pump power at a wavelength of 1554.98 nm.

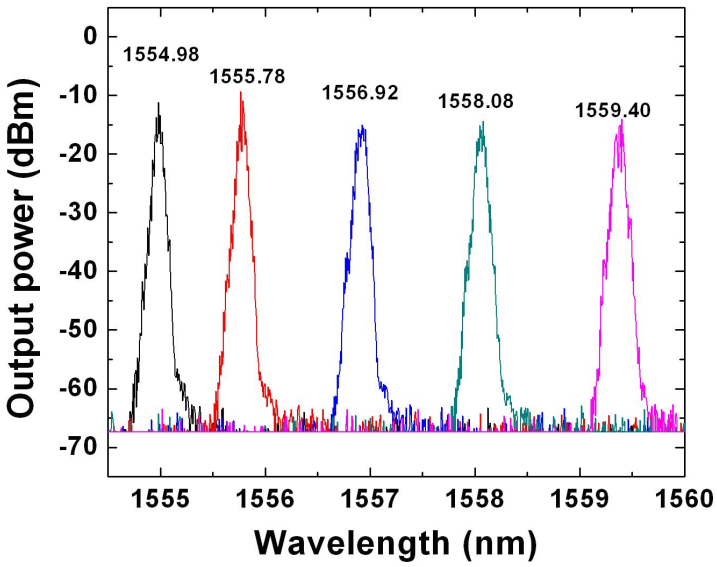

Figure 7.5: Laser output spectra at different wavelengths at a pump power of 29.7 mW.

microseconds) is much longer than the SA's recovery time (in the range of subpicosecond). The maximum pulse energy is measured to be 14.1 nJ at a pump power of 45.8 mW with a pulse peak power of 2 mW. The present laser could be tuned by applying axial strain on the FBG, and the output spectra for different wavelengths are illustrated in Fig. 7.5. The

laser output power stays relatively flat from 1555 to 1560 nm. An average value of 139.7 μW, with a standard deviation of 1.98 μW (1.4%), is obtained for the wavelengths within the tuning range at a pump power of 29.7 mW. The tuning range could be extended by using a highly stretchable FBG [32].

7.1.4 Conclusion

A low pump threshold tunable passively Q-switched EDFL with SWNTs as an SA is presented. The SA is constructed by depositing SWNTs on fiber connectors using optical radiation propagating in the fiber. The work has been repeated by using different SAs constructed with the same method, and similar experimental results confirm the reliability of the laser configuration. Self-mode-locking effect is also observed. By introducing an extra unpumped EDF in the cavity, this effect could be effectively suppressed. Higher output power could be achieved by depositing the SWNTs onto a D-shaped fiber [28], because in this case only part of the optical power of the mode interacts with the SWNTs to give the loss modulation into the laser cavity.

7.2 Passively Mode-Locked Erbium-Doped Fiber Laser with Single-Walled Carbon Nanotubes as a Saturable Absorber

7.2.1 Introduction

Ultrafast lasers which can generate short optical pulses whose durations are from picoseconds down to femtoseconds have a large variety of engineering, industrial, and medical applications. The properties of short duration, high peak power, broad spectral bandwidth, short coherence length of the optical pulses generated by these lasers could be used for the applications of high speed telecommunications, automotive radar, micromachining, high resolution optical coherence tomography, video projection, ablation, etc [33]. On the other hand, compared to conventional solid-state lasers, fiber lasers have the advantages of high stability, high reliability, compact structure, low cost, immunity to tough environmental changes, etc., because of the all-fiber structure which does not need any complex water cooling system used in solid-state laser systems, and the potential for miniaturization and integration due to the small size of the optical fibers. Therefore, many companies are developing these ultrafast fiber lasers to meet the rapidly growing demand for such lasers in various fields, such as IMRA America Inc., Calmar Laser Inc., Avesta Project Ltd., etc.

Mode-locking technique is a key method to generate ultrafast laser pulses. In general, there are two categories, which are active and passive mode-locking. Active mode-locking involves using modulators which have to be controlled externally to modulate the amplitude or phase of the light in the laser cavity. However, the realization of passive mode-locking is simpler and easier by placing a purely passive SA element inside the laser cavity, so that the passively mode-locked laser has the potential to be built with a low cost, and compact structure. Passively mode-locked fiber lasers mostly resort to semiconductor SAs. However, these bulk structures are not compatible with optical fibers which might sacrifice the compactness of fiber lasers. Recently, SWNTs turns out to be excellent SAs, because of their good compatibility with optical fibers, low saturation intensity, fast recovery time, wide operating bandwidth, and mechanical and environmental robustness. Different methods have been reported to deposit SWNTs onto optical fibers or fiber related devices. We will use the same deposition method for SWNT based SA presented in Section 7.1.

The first major concern is the output pulse energy. Soliton fiber lasers are limited to low pulse energies. At higher energies, nonlinear effects cause wave breaking, which results in multiple pulsing. Stretched-pulse fiber laser consists of segments of anomalous and normal group velocity dispersion, which implement the concept of dispersion management [34]. Although it could generate pulse energy higher than that obtained with soliton fiber laser, the pulse energy is still limited. Many efforts have been made to increase the pulse energy obtainable from mode-locked fiber lasers by developing similariton fiber lasers. Similariton fiber lasers generate chirped pulses and operate with positive cavity dispersion comprising positive dispersion gain fiber [35]. Following the first similariton fiber laser was reported by Ilday *et al.* [34], many works have been done on this topic [36, 37, 38, 39, 40, 41, 42, 43].

The second concern is the pulse duration. Fiber lasers working in the normal dispersion region usually have longer pulse durations compared to the anomalous ones. This could also offer an opportunity for us to build a pulsed laser source with sub-nanosecond pulse duration to be used for fully distributed fiber sensor systems. We will first construct an EDFL working with the anomalous dispersion cavity to confirm the reliability of the SA, and then develop the normal dispersion EDFL to generate longer pulses with higher energy in order to find the potential applications in fully distributed fiber sensor systems.

7.2.2 Experiment and Discussion for Anomalous Dispersion Cavity

The mode-locked erbium-doped fiber laser experiment setup with anomalous dispersion cavity is shown in Fig. 7.6. The fiber laser is pumped by a 980-nm laser diode through a WDM coupler. A 60-cm long single-mode highly doped EDF is used as a gain medium. The PC is utilized for optimization of the laser output. The SA (the same SA developed in

Section 7.1) is spliced into the cavity. An ISO is used to ensure unidirectional operation. The 10% port of an OC is used to extract the output power, and a second ISO is employed to avoid backward reflection. Our cavity uses anomalous dispersion fibers, with an overall negative group velocity dispersion, in order to facilitate soliton-like pulse shaping through the interplay of group velocity dispersion and self-phase modulation [44].

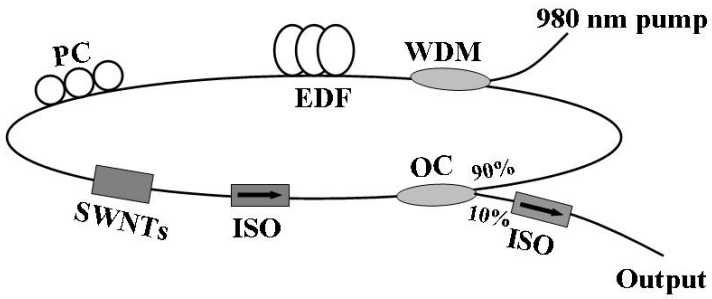

Figure 7.6: Mode-locked EDFL configuration. EDF: erbium-doped fiber laser; PC: polarization controller; SWNT: single-walled carbon nanotube; OC: optical coupler; ISO: isolator.

The typical laser pulse train is shown in Fig. 7.7. The pump power is about 36.5 mW and the average output power is 598.5 μW. The repetition rate is about 20 MHz (interpulse duration $\sim$ 52 ns) which is consistent with the total length of cavity ($\sim$ 10 m) resulting a single pulse energy of 0.03 nJ. Fig. 7.8 shows the autocorrelator trace, and the pulse duration (FWHM) is about 1.5 ps. The output laser spectrum is shown in Fig. 7.9. The

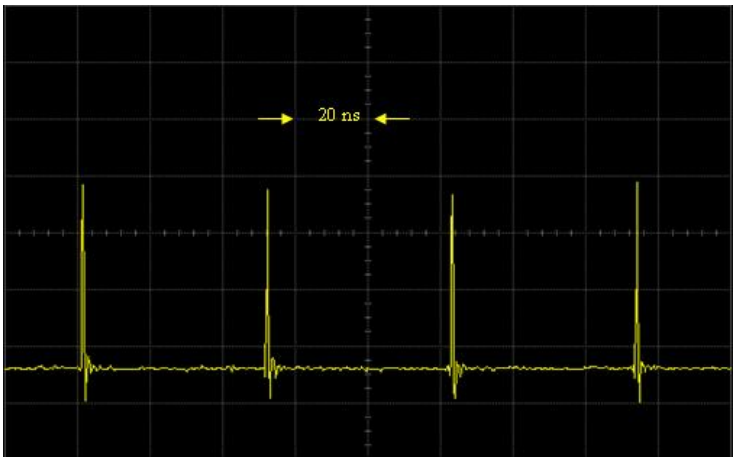

Figure 7.7: Pulse train of the mode-locked fiber laser with anomalous dispersion cavity.

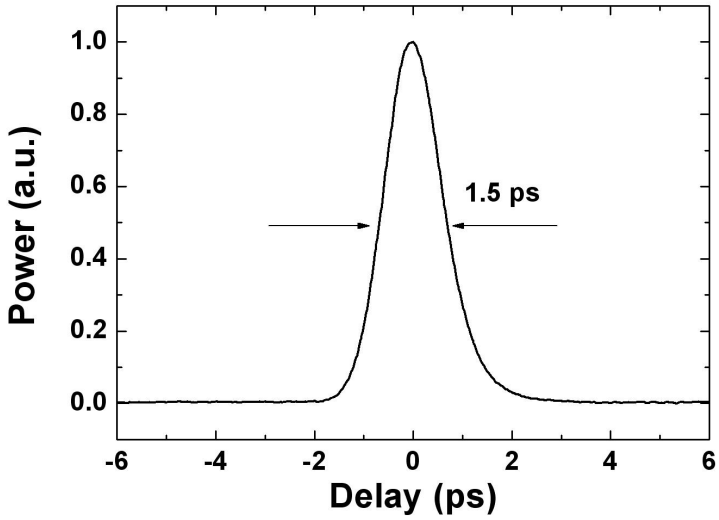

Figure 7.8: Autocorrelator trace of the optical pulse.

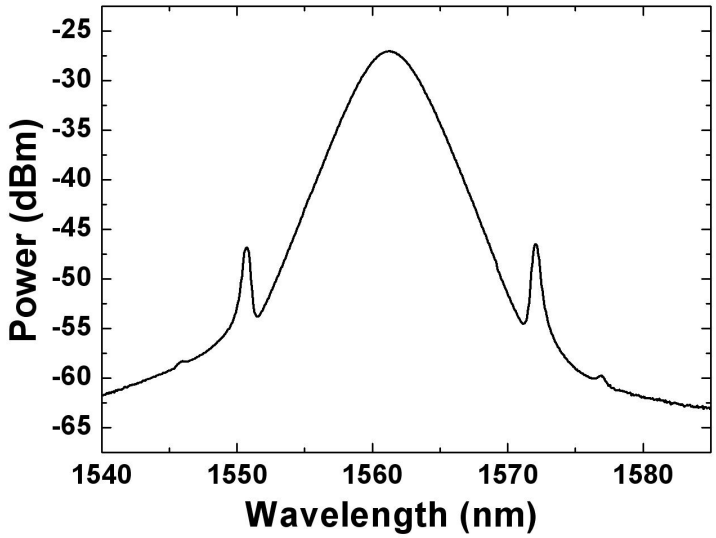

Figure 7.9: Output spectrum of the mode-locked EDFL with a normal dispersion cavity; the spectral sidebands confirm that the laser is operating in soliton region.

sideband structure indicated in the spectrum arising from periodic cavity perturbations [45] confirms that the laser is operating in the soliton region. Further increasing the pump power will result pulse breaking due to the large nonlinear phase accumulation [34]. In order to achieve higher pulse energy, normal dispersion cavity would be adopted in Section 7.2.2, and the pulse duration could be achieved in the sub-nanosecond range which has the

potential to be used as a source to generate short length BDG for fully distributed sensor systems.

7.2.3 Simulation and Experiment for Normal Dispersion Cavity

In order to better understand the features of the normal dispersion cavity mode-locked EDFL, numerical simulation of the laser operation is also performed using the extended nonlinear Schrödinger Equation (NLSE). However, in order to obtain insight on the fundamental effects governing the laser, only scalar NLSE will be considered [45]. Pulse propagation in the gain fiber is described by the scalar NLSE which includes the effects of dispersion, Kerr nonlinearity and saturated gain with a finite bandwidth:

$$\frac{\partial A(z,T)}{\partial z} = -i\frac{1}{2}[\beta_2 + ig(z)T_2^2]\frac{\partial^2}{\partial T^2}A(z,T) + i\gamma\left|A(z,T)\right|^2 A(z,T) + \frac{g(z)}{2}A(z,T), \quad (7.1)$$

where $A(z,T)$ is the complex pulse envelop; T is the time in the co-moving frame; β_2 is the group velocity dispersion parameter; T_2 is the dipole relaxation time which is related to the gain bandwidth. γ is the self-phase modulation coefficient and $g(z)$ is the saturated gain coefficient given by $g(z) = g_0/[1 + E(z)/E_{sat}]$, where g_0 is the small signal gain coefficient; $E(z)$ is the pulse energy and E_{sat} is the gain saturation energy which is pump-power dependent.

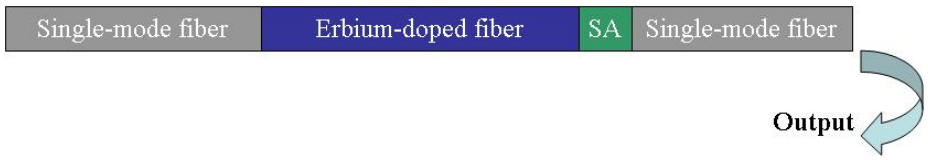

Figure 7.10: Simulation procedure and schematic diagram of the main components of the laser. SA: saturable absorber.

The simulation procedure is shown in Fig. 7.10. The function of the SA is modeled as a transfer function with the transmittance $T = 1 - l_0/[1 + P(T)/P_{sat}]$, where $l_0 = 0.2$ is the unsaturated loss, $P(T)$ is the instantaneous pulse power, and P_{sat} is the saturation power. The pulse amplitude is reduced by a factor of 10 after the SA to account for all linear losses, which can be lumped together without loss of generality.

The numerical model is solved with a standard split-step Fourier method. The simulations are running until the field becomes constant after a finite number of traversals of the cavity. A typical simulation results of pulse shape and the output spectrum are shown in Figs. 7.11 and 7.12. The parameters used to obtain the figures are as follows: $g_0 = 1$ /m; $\gamma = 0.0047$ /(Wm) for EDF while $\gamma = 0.002$ /(Wm) for SMF; $\beta_2 = -0.02$ ps^2/m for SMF

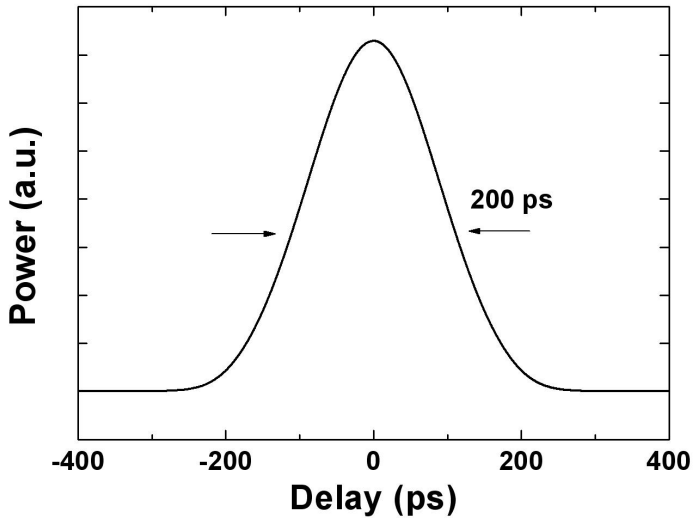

Figure 7.11: Result of the simulation of the output temporal intensity profile.

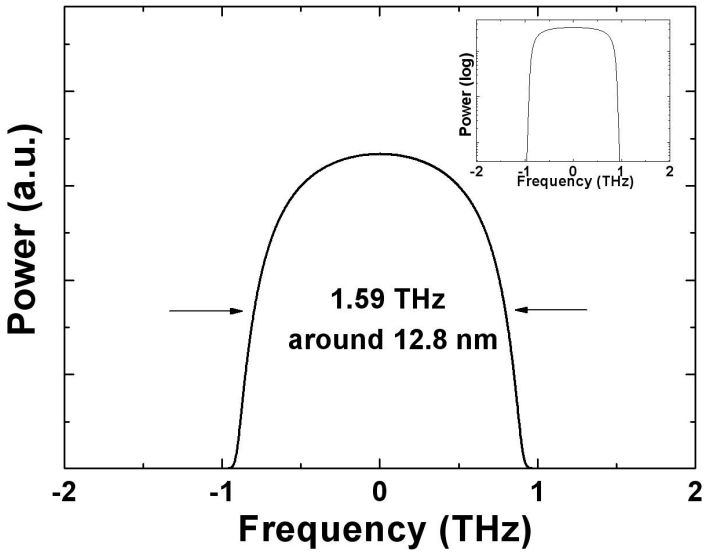

Figure 7.12: Result of the simulation of the output power spectrum. Inset shows the spectrum in logarithm.

while $\beta_2 = 0.03434$ ps^2/m for EDF; $T_2 = 0.025$ ps; $E_{sat} = 1$ nJ; $P_{sat} = 10$ W. The length of the EDF is 32 m; the SMF length is 4.5 m in total. The pulse duration (FWHM) is about 200 ps, and the bandwidth of the spectrum (FWHM) is about 12.8 nm. The simulation results show that with long length of normal dispersion EDF, it is feasible to generate the optical pulses with duration in the range of sub-nanosecond. In addition, the spectrum

shows unique sharp edges which is one of the properties of the normal dispersion fiber laser (see inset of Fig. 7.12).

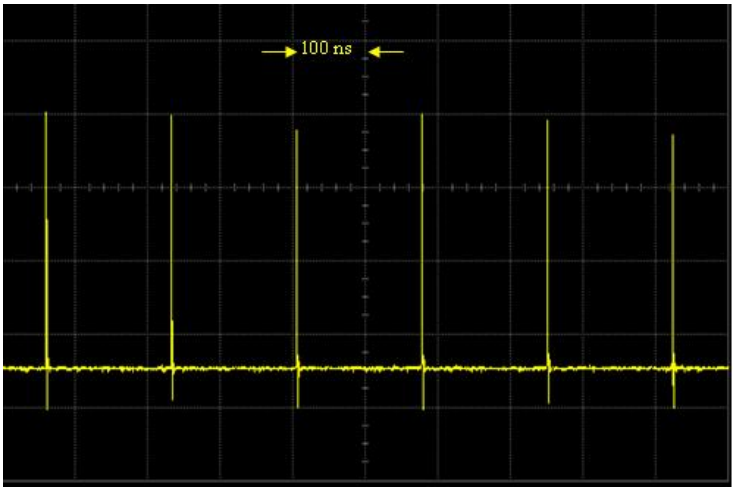

Figure 7.13: Experiment result of the pulse train with normal dispersion cavity.

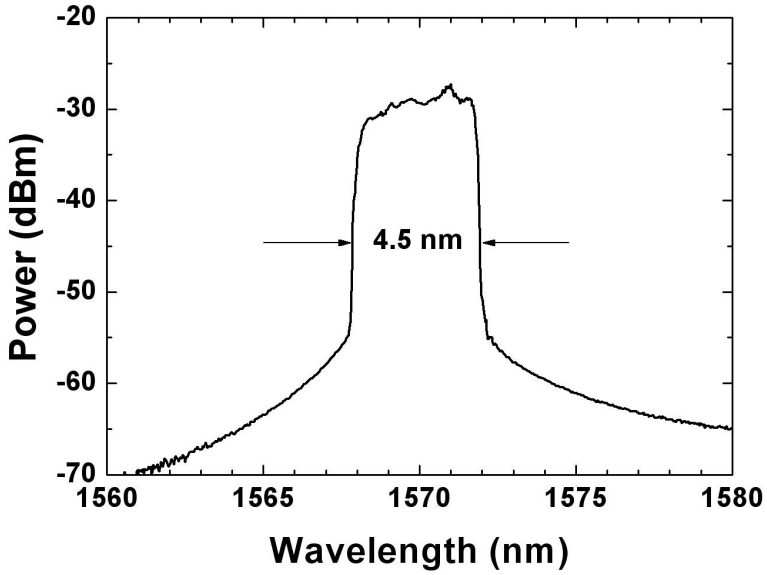

Figure 7.14: Experiment result of the output power spectrum with normal dispersion cavity.

Encouraged by the simulation results, we construct a laser cavity with normal dispersion. The experiment setup is very similar with that for anomalous dispersion cavity as

shown in Fig. 7.6, except that EDF has been replaced with the single-mode high numerical aperture EDF with large normal dispersion parameter of 0.03434 ps^2/m and a 30/70 OC with 30% output to extract the beam. In order to achieve long pulse duration, 32-m long EDF is used in the experiment. The total cavity length is about 36.5 m with 4.5-m long SMF. Therefore, the total dispersion of the cavity is normal. Fig. 7.13 shows the pulse train, where the interpulse duration is about 180 ns which is consistent with the 36.5-m long cavity length under the pump power of 51 mW. The average output power is 6.1 mW resulting a single pulse energy of 1 nJ which is much higher than that obtained with anomalous dispersion cavity. The output spectrum is shown in Fig. 7.14. The wing-structure is because of the amplified spontaneous emission since we are using pretty long length of the EDF. The shape edge shown on the spectrum confirms that the laser is operating in the normal dispersion region which is predicted by the simulation results. Fig. 7.15 shows the

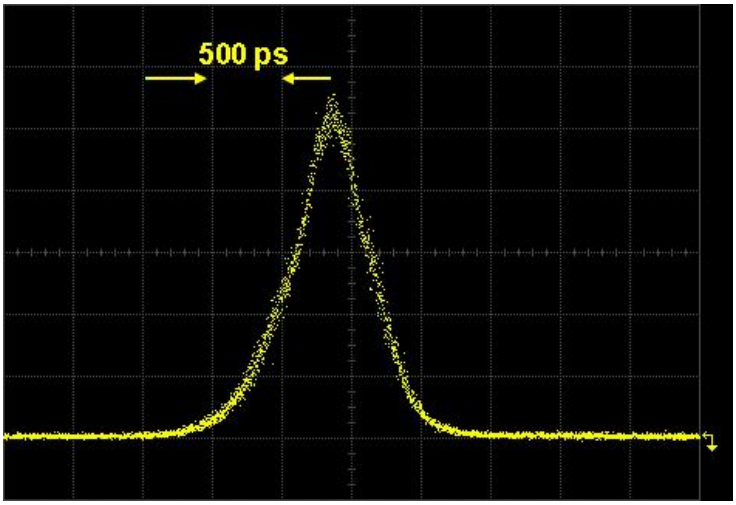

Figure 7.15: Single pulse envelope recorded by the wide-band oscilloscope.

single pulse envelope recorded by a 10 Gb/s wide-band oscilloscope (Agilent 86100A Infiniium DCA wide-band oscilloscope with 86106A module). The pulse duration (FWHM) is about 550 ps. Although the experiment results are different from the simulation results, the trends agree with each other. This discrepancy arises from the unknown parameters of the actual SA and active fiber as well as other influences. Further investigation is also needed here.

7.3 Summary of Future Work

First of all, perform detailed investigations on BDG. The SBS case could be modeled as three wave-mixing; that is two counterpropagating light waves and an acoustic wave which

is described in terms of the material density distribution inside the fiber core [46]. For the BDG case in a PMF, the situation is more complex. Two writing light waves of one polarization counterpropagating inside the PMF generate the BDG; one probe (reading) light wave with the orthogonal polarization is reflected by the BDG, and the reflected wave has the same polarization with the probe beam; the material density obeys the acoustic wave equation which needs to consider the total electric field (the superposition of the four light waves) in the fiber. At the steady state, the five coupled equations could be solved under certain assumptions analytically, and the results are very similar to the general four-wave mixing (FWM) process inside the fiber. The gain spectrum is neither a Gaussian nor a Lorentzian shape, but is very similar to the parametric gain profile of the FWM [44]. However, for the general dynamic case without the assumptions, computer simulations need to be performed. With this comprehensive description, the detailed property of BDG could be understood, such as the spectrum, the reflectance of the BDG, as well as their dependence on the pump and probe power. This theoretical analysis would be very useful in the long run, not only for the understanding of the physical principle but also for the parameter optimization of the sensor system with the BDG spectrum shift as a second factor to achieve temperature and strain discrimination.

Secondly, develop compact stable pulse laser source with the pulse duration of sub-nanosecond for fully distributed fiber sensor system. Although some initial simulation and experiment work has been carried on for this purpose with SWNTs as a SA (Section 7.2), the detailed theoretical analysis of the laser characteristics and comprehensive experiment validation are missing. Actually, mode-locked fiber laser is another important topic which needs long time comprehensive research and study. With in the cavity, many effects such as the group velocity dispersion, self-phase modulation, gain dispersion, etc. interact with each other which makes the problem rather complex. In addition, other deposition method for SWNT based SA could be used and developed in order to make the laser have better performance. When studying these effects, it also help us design better sensor systems since many of the effects are existing in the sensor system as well.

Thirdly, after the source has been developed, we could use the sub-nanosecond optical pulses counterpropagating inside the PMF to generate short length BDG in order to achieve high spatial resolution. To date, the shortest BDG achieved is about 20 cm. If we could generate the BDG with 1-cm length, the spatial resolution could be much improved. Then, we could use the BDG spectrum shift as the second factor to discriminate temperature and strain for fully distributed fiber sensor system. However, when using this technique, theoretical guidance is indispensable to optimize the sensor parameters.

Finally, we could also adopt the differential pulse-pair BOTDA (DPP-BOTDA) method [7, 8] to achieve high spatial resolution. For the case of generating short BDG, the timing of the counterpropagating writing beams has to be controlled in order to cover the whole fiber length. This is not very convenient for fully distributed sensing since this would increase

the scanning time for obtaining the date for all the positions long the fiber. Therefore, the DPP-BOTDA method could be considered. Instead of generating a short length BDG, two CW writing beams could be used to generate the BDG along the whole length of the PMF. By injecting two pulses with slightly different durations as reading pulses, different reflected traces are expected to be obtained since different lengths of the pulses would cover different lengths of the BDG. By subtracting the traces generated by the two pulses respectively, a high spatial resolution is expected to be achieved. However, in this case, the theoretical analysis and computer simulation are also indispensable for the sensor parameter optimization. Therefore, starting with the detailed investigation of the BDG, following by the experimentation and simulating of the mode-locked fiber laser, a new project could be carried on for developing powerful fully distributed fiber sensor with a simple sensing head which could achieve complete temperature and strain discrimination.

APPENDICES

Appendix A

Bragg Wavelength Shifts with Strain and Temperature

The Bragg wavelength λ_B of a fiber Bragg grating (FBG) is given as follows:

$$\lambda_B = 2n_{eff}\Lambda, \tag{A.1}$$

where n_{eff} is the effective refractive index of the core and Λ is the periodicity of the refractive-index modulation (grating pitch).

The change in the Bragg wavelength λ_B of an FBG for a given change in length, assuming isothermal conditions and neglecting higher-order terms, is given by

$$\Delta\lambda_B = 2(\Lambda\frac{\partial n_{eff}}{\partial L} + n_{eff}\frac{\partial\Lambda}{\partial L})\Delta L, \tag{A.2}$$

where L is the length of the grating. Given that the longitudinal strain by

$$\varepsilon = \frac{\Delta L}{L}, \tag{A.3}$$

and

$$\Delta[\frac{1}{n_{eff}^2}] = -2\frac{\Delta n_{eff}}{n_{eff}^3}, \tag{A.4}$$

and assuming that

$$\frac{\partial\Lambda}{\partial L} = \frac{\Lambda}{L}, \tag{A.5}$$

Eq. (A.1) could be rewritten as

$$\Delta\lambda_B = 2\Lambda\left\{-\frac{n_{eff}^3}{2}\Delta\left[\frac{1}{n_{eff}^2}\right]\right\} + 2n_{eff}L\frac{\partial\Lambda}{\partial L}\varepsilon. \tag{A.6}$$

By considering strain-optic theory and assuming for low birefringent optical fibers where the strain-optic tensor is isotropic, the strain sensitivity could be expressed as

$$\frac{\Delta\lambda_B}{\lambda_B} = (1 - p_e)\varepsilon, \tag{A.7}$$

where p_e is the effective photoelastic constant which is given as

$$p_e = \frac{n_{eff}^2}{2}\left[p_{12} - \nu(p_{11} + p_{12})\right], \tag{A.8}$$

where p_{ij} are the Pockel's coefficients of the strain-optic tensor and ν is Poisson's ratio for the fiber.

A change in temperature produces the a Bragg wavelength shift due to the the thermal expansion and a change of the refractive index with temperature. The change for the Bragg wavelength with respect to temperature change could be expressed as follows

$$\Delta\lambda_B = 2(n_{eff}\frac{\partial\Lambda}{\partial T} + \Lambda\frac{\partial n_{eff}}{\partial T})\Delta T, \tag{A.9}$$

where T is the ambient temperature. By rearranging the above equation, the fractional Bragg wavelength shift could be given by

$$\frac{\Delta\lambda_B}{\lambda_B} = (\frac{1}{\Lambda}\frac{\partial\Lambda}{\partial T} + \frac{1}{n_{eff}}\frac{\partial n_{eff}}{\partial T})\Delta T = (\alpha + \frac{1}{n_{eff}}\frac{\partial n_{eff}}{\partial T})\Delta T, \tag{A.10}$$

where α is the coefficient of thermal expansion of the fiber material.

Therefore, the shift in Bragg wavelength with strain and temperature could be given by summing Eqs. (A.7) and (A.10) with the use of Eq. (A.8) as

$$\frac{\Delta\lambda_B}{\lambda_B} = \left\{1 - (\frac{n_{eff}^2}{2})\left[p_{12} - \nu(p_{11} + p_{12})\right]\right\}\varepsilon + (\alpha + \frac{1}{n_{eff}}\frac{\partial n_{eff}}{\partial T})\Delta T. \tag{A.11}$$

Appendix B

Power Ratio Expression for Edge Filter Interrogation Technique of a Fiber Bragg Grating Sensor

We can model the narrow-band, back-reflected fiber Bragg grating (FBG) peak as a Gaussian function of wavelength with a spectral width of $\Delta\lambda$ (at $1/e$-intensity point) and a center wavelength (Bragg wavelength) of λ_B. The spectral intensity of this back-reflected Bragg peak as a function of wavelength can be given as

$$I_B = I_0 R \exp[-(\frac{\lambda - \lambda_B}{\Delta\lambda/2})^2], \tag{B.1}$$

where I_0 is the intensity of the light incident on the FBG and R is the maximum reflectivity at the Bragg wavelength. It is assumed that both the I_0 and R are nonzero over the wavelength range of interest.

As seen from Fig. 2.6, the reflected light from the FBG is split into two paths, and the coupler has the splitting ratio of K_1/K_2. The light split with a coupling ratio of $K_1/(K_1 + K_2)$ is filtered and then detected. The linearized model of the filter function $F(\lambda)$ can be expressed as (see Fig. 2.5)

$$F(\lambda) = S(\lambda - \lambda_0), \tag{B.2}$$

where S is a constant determined by the slope of the filter and $F(\lambda)$ is equal to zero at λ_0. Therefore, the intensity of the filtered and unfiltered optical signals, I_S and I_R can be given as

$$I_S = \frac{K_1}{K_1 + K_2} \int_0^\infty I_B(\lambda) F(\lambda) d\lambda, \tag{B.3}$$

and

$$I_R = \frac{K_2}{K_1 + K_2} \int_0^\infty I_B(\lambda) d\lambda. \tag{B.4}$$

Inserting Eqs. (B.1) and (B.2) into Eqs. (B.3) and (B.4), and using Gaussian integral formula

$$\int_{-\infty}^{\infty} \exp(-x^2) dx = \sqrt{\pi}, \tag{B.5}$$

we could obtain

$$I_S = I_0 R S \frac{K_1}{K_1 + K_2} \frac{\sqrt{\pi}}{4} (\lambda_B - \lambda_0 + \frac{\Delta\lambda}{2\sqrt{\pi}}) \Delta\lambda, \tag{B.6}$$

and

$$I_R = I_0 R \frac{K_2}{K_1 + K_2} \frac{\sqrt{\pi}}{4} \Delta\lambda. \tag{B.7}$$

The ratio of the filtered to unfiltered outputs is therefore given by

$$\frac{I_S}{I_R} = S \frac{K_1}{K_2} (\lambda_B - \lambda_0 + \frac{\Delta\lambda}{2\sqrt{\pi}}). \tag{B.8}$$

Appendix C

Properties of a Fabry-Pérot Interferometer

A Fabry-Pérot interferometer (FPI) consists of two plane mirrors with power reflectivities R_1 and R_2 separated by a distance L and containing a medium of refractive index of n. The corresponding transmissions of the mirrors are T_1 and T_2, such that $T_i + R_i = 1$, $(i = 1, 2)$. We assume a plane wave of a wavelength λ incident on the FPI in a direction making an angle θ_1 with the normal to the two mirrors as shown in Fig. C.1. This wave is indicated

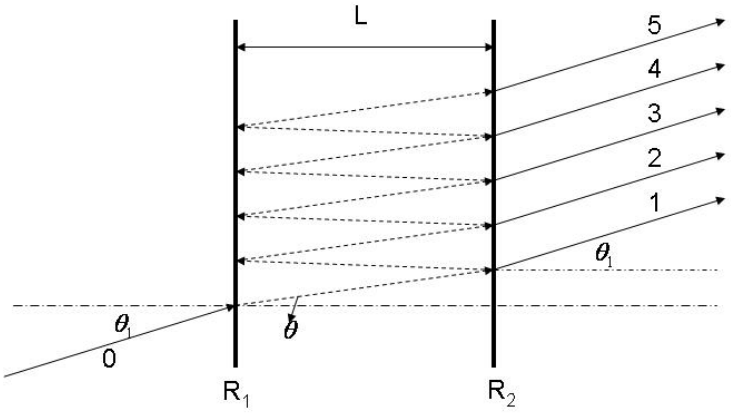

Figure C.1: Multiple beams interference in a Fabry-Pérot interferometer.

by Ray 0. The transmitted beam from the FPI consists of a superposition of the beam resulting from a single pass through the two mirrors and from all multiple reflections. The

transmitted beam, E_T is obtained by summing E_l of all the beams, as

$$E_T = \sum_{l=1}^{\infty} E_l = [E_0 t_1 t_2 \exp(j\phi_1)] \sum_{m=0}^{\infty} (r_1 r_2)^m \exp(2mj\phi), \tag{C.1}$$

where E_0 is amplitude of the incident beam; t_1 and t_2 are electric field transmissions of the two mirrors, while r_1 and r_2 are the corresponding field reflectivities. The relationship between them are $R_1 = r_1^2$, $R_2 = r_2^2$, $T_1 = t_1^2$, and $T_2 = t_2^2$. θ and θ_1 are related by the Snell's law. ϕ_1 is the phase shift for a single pass, which includes any phase shift due to passage through the two mirrors; 2ϕ is the phase difference between successive multiple reflections, and is given by

$$2\phi = 2kL\cos(\theta) = \frac{4\pi n}{\lambda} L\cos(\theta). \tag{C.2}$$

Eq. (C.1) could be summed to give

$$E_T = E_0 \exp(j\phi_1) \frac{t_1 t_2}{1 - (r_1 r_2)\exp(2j\phi)}. \tag{C.3}$$

Note that power transmission of the FPI T_{FPI} is given by

$$T_{FPI} = \frac{|E_T|^2}{|E_0|^2}, \tag{C.4}$$

and inserting Eq. (C.3) into (C.4), one can obtain

$$T_{FPI} = \frac{t_1^2 t_2^2}{1 + r_1^2 r_2^2 - 2r_1 r_2 \cos(2\phi)} = \frac{T_1 T_2}{1 + R_1 R_2 - 2\sqrt{R_1 R_2}\cos(2\phi)}. \tag{C.5}$$

The reflectivity of the FPI, R_{FPI} could be obtained by $R_{FPI} = 1 - T_{FPI}$ as

$$R_{FPI} = \frac{R_1 + R_2 - 2\sqrt{R_1 R_2}\cos(2\phi)}{1 + R_1 R_2 - 2\sqrt{R_1 R_2}\cos(2\phi)}. \tag{C.6}$$

If we consider the beam is normal incident on the mirror of the FPI, $\theta = 0$, so that we have the same results shown by Eqs. (2.9)-(2.11) in Chapter 2.

Appendix D

Resonance Wavelength Shift of Multimode Fiber Interferometer with Temperature and Strain

The expression for the resonance wavelength of a multimode fiber (MMF) interferometer is given as

$$\lambda = \frac{\Delta n L}{N}, \tag{D.1}$$

where $\Delta n = n_2 - n_1$, and n_1 and n_2 are the mode indices; L is the length of MMF; N is an integer given as $N = 1, 2, 3, ...$

When a longitudinal strain is applied on the MMF, by differentiating Eq. (D.1), we could obtain the wavelength shift, $\Delta\lambda$, with respect to the elongation of the fiber ΔL as

$$\Delta\lambda = \left[\frac{\Delta n}{N} + \frac{\partial(\Delta n)}{\partial L}\frac{L}{N}\right]\Delta L. \tag{D.2}$$

Rearranging Eq. (D.2), one could obtain

$$\Delta\lambda = \left[\frac{\Delta n L}{N} + \frac{1}{\Delta n}\frac{\partial(\Delta n)}{\partial L/L}\frac{\Delta n L}{N}\right]\frac{\Delta L}{L}. \tag{D.3}$$

By introducing the longitudinal strain ε which is defined by $\varepsilon = \partial L/L$, Eq. (D.3) could be reduced to

$$\frac{\Delta\lambda}{\lambda} = \left[1 + \frac{1}{\Delta n}\frac{\partial(\Delta n)}{\varepsilon}\right]\varepsilon. \tag{D.4}$$

When there is an ambient temperature change, the resonance wavelength shift could be expressed as

$$\Delta\lambda = \left[\frac{\partial(\Delta n)}{\partial T}\frac{L}{N} + \frac{\partial L}{\partial T}\frac{\Delta n}{N}\right]\Delta T. \tag{D.5}$$

Rearranging,

$$\frac{\Delta\lambda}{\lambda} = \left[\frac{1}{\Delta n}\frac{\partial(\Delta n)}{\partial T} + \frac{1}{L}\frac{\partial L}{\partial T}\right]\Delta T. \tag{D.6}$$

By summing Eqs. (D.4) and (D.6), the resonance wavelength shift of an MMF interferometer with respect to strain and temperature could be expressed as

$$\frac{\Delta\lambda}{\lambda} = \left[1 + \frac{1}{\Delta n}\frac{\partial(\Delta n)}{\partial \varepsilon}\right]\varepsilon + \left[\frac{1}{\Delta n}\frac{\partial(\Delta n)}{\partial T} + \frac{1}{L}\frac{\partial L}{\partial T}\right]\Delta T. \tag{D.7}$$

Appendix E

Transmission of a High-Birefringence Fiber Loop Mirror

The configuration of a high-birefringence fiber loop mirror (HBFLM) is shown in Fig. E.1. It consists of an optical coupler (OC) with the splitting ratio of K, a section of high-birefringence fiber (HBF), and polarization controller (PC). θ_1 and θ_2 are the angles between the light at both ends of the HBF and the fast or slow axis of the HBF, respectively. The incident light at the coupler from Port 1 is split into two beams of clockwise and

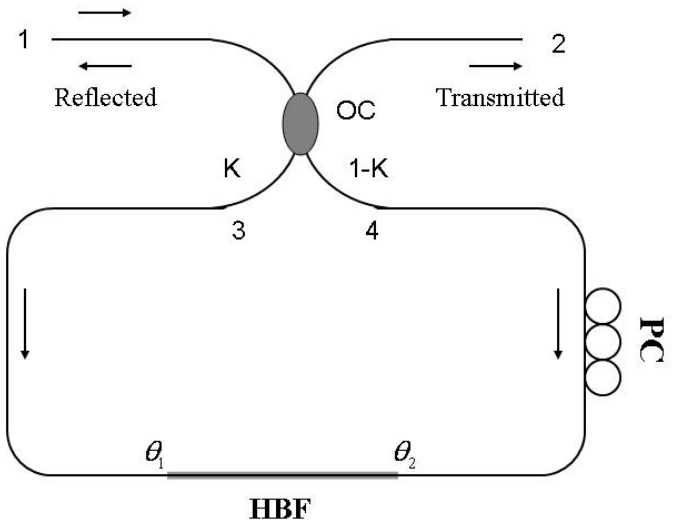

Figure E.1: Schematic illustration of a high-birefringence fiber loop mirror.

counterclockwise propagation. Each of the resultant beams is decomposed into two beams

after it travels through the HBF. Assuming that the input light ,E_{in}, at Port 1 of the coupler is

$$E_{in} = \begin{bmatrix} E_{in,x} \\ E_{in,y} \end{bmatrix}, \tag{E.1}$$

where $E_{in,x}$ and $E_{in,y}$ are x and y components of the input light. The output light at Ports 3 and 4 of the coupler are given by

$$E_3 = \sqrt{K} E_{in} \tag{E.2}$$

and

$$E_4 = \sqrt{1-K} H E_{in}, \tag{E.3}$$

respectively, where K is the power-splitting ratio of the coupler in the clockwise direction and H is the phase delay matrix when the light propagates through the cross arm of the coupler from Port 1 to Port 4 which is given by

$$H = \begin{bmatrix} \exp(\frac{\pi}{2}i) & 0 \\ 0 & \exp(\frac{\pi}{2}i) \end{bmatrix}. \tag{E.4}$$

Next we express the phase delay matrix T induced by the HBF as

$$T = \exp(-i\frac{2\pi n_e L}{\lambda}) \begin{bmatrix} 1 & 0 \\ 0 & \exp(-i\frac{2\pi L(n_o - n_e)}{\lambda}) \end{bmatrix}, \tag{E.5}$$

where L is the length of the HBF; n_o and n_e are the refractive indices of ordinary (o) and extraordinary (e) light respectively; λ is the wavelength. In addition, the polarization state induced by rotation angle θ_i, $i = 1, 2$ could be expressed as polarization-state rotation matrix R_i, $i = 1, 2$,

$$R_i = \begin{bmatrix} \cos(\theta_i) & -\sin(\theta_i) \\ \sin(\theta_i) & \cos(\theta_i) \end{bmatrix}. \tag{E.6}$$

Therefore, the output at Port 1 and Port 2 could be given

$$P_{1,out} = \sqrt{1-K} H R_2 T R_1 E_3 + \sqrt{K} R_1^{-1} T R_2^{-1} E_4, \tag{E.7}$$

and

$$P_{2,out} = \sqrt{K} R_2 T R_1 E_3 + \sqrt{1-K} H R_1^{-1} T R_2^{-1} E_4. \tag{E.8}$$

The expressions for reflectivity $R(\lambda)$ and transmission $T(\lambda)$ of the HBFLM could be calculated as

$$R(\lambda) = \frac{I_{1,out}}{I_{in}} = \frac{(P_{1,out}^*)^T P_{1,out}}{(E_{in}^*)^T E_{in}}, \tag{E.9}$$

and

$$T(\lambda) = \frac{I_{2,out}}{I_{in}} = \frac{(P_{2,out}^*)^T P_{2,out}}{(E_{in}^*)^T E_{in}}. \tag{E.10}$$

Substituting Eqs. (E.1)-(E.8) to Eqs. (E.9) and (E.10), one could obtain

$$R(\lambda) = 4K(1-K)\left[1 - \sin^2(\theta_1+\theta_2)\cos^2(\frac{\pi BL}{\lambda})\right], \tag{E.11}$$

and

$$T(\lambda) = (1-2K)^2 + 4K(1-K)\left[\sin^2(\theta_1+\theta_2)\cos^2(\frac{\pi BL}{\lambda})\right], \tag{E.12}$$

where $B = n_o - n_e$ is the birefringence of HBF. For a 3-dB coupler, $K = 0.5$, we could obtain the following expressions

$$R(\lambda) = 1 - \left[\sin(\theta_1+\theta_2)\cos(\frac{\pi BL}{\lambda})\right]^2, \tag{E.13}$$

and

$$T(\lambda) = \left[\sin(\theta_1+\theta_2)\cos(\frac{\pi BL}{\lambda})\right]^2. \tag{E.14}$$

Appendix F

Permissions

Part of the contents in Chapter 3, Chapter 4, Chapter 6, and Chapter 7 have been granted reprint permission by IEEE as

©2010 IEEE. Reprinted, with permission, from IEEE Journal of Lightwave Technology, Temperature insensitive all-fiber compact polarization-maintaining photonic crystal fiber based interferometer and its applications in fiber sensors, B. Dong, D. P. Zhou, and L. Wei.

©2010 IEEE. Reprinted, with permission, from IEEE Photonics Technology Letters, Tunable passively Q-switched Erbium-doped fiber laser with carbon nanotubes as a saturable absorber, D. P. Zhou, L. Wei, B. Dong, and W. K. Liu.

©2010 IEEE. Reprinted, with permission, from 2010 Symposium on Photonics and Optoelectronics, Simultaneous strain/temperature measurement with fiber Bragg grating and high-birefringence fiber loop mirrors using an intensity-based interrogation method, D. P. Zhou, L. Wei, and W. K. Liu.

©2009 IEEE. Reprinted, with permission, from IEEE Photonics Technology Letters, Simultaneous strain and temperature measurement with fiber Bragg grating and multimode fibers using an intensity-based interrogation method, D. P. Zhou, L. Wei, W. K. Liu, and J. W. Y. Lit.

This material is posted here with permission of the IEEE. Such permission of the IEEE does not in any way imply IEEE endorsement of any of the University of Waterloo's products or services. Internal or personal use of this material is permitted. However, permission to reprint/republish this material for advertising or promotional purposes or for creating new collective works for resale or redistribution must be obtained from the IEEE by writing to pubs-permissions@ieee.org. By choosing to view this material, you agree to all provisions of the copyright laws protecting it.

References

References for Chapter 1

[1] K. C. Kao and G. A. Hockham. Dielectric-fibre surface waveguides for optical frequencies. *Proc. IEE*, 113(7):1151–1158, 1966. 1

[2] F. T. S. Yu and S. Yin. *Fiber Optic Sensors*. Marcel Dekker, Inc., New York, 2002. 1, 9

[3] H. Nakstad and J. T. Kringlebotn. Oil and gas applications: Probing oil fields. *Nature Photonics*, 2(3):147–149, 2008. 3

[4] L. Zou, X. Bao, F. Ravet, and L. Chen. Distributed Brillouin fiber sensor for detecting pipeline buckling in an energy pipe under internal pressure. *Applied Optics*, 45(14):3372–3377, 2006. 3, 4

[5] L. Zou, G. A. Ferrier, S. Afshar V., Q. Yu, L. Chen, and X. Bao. Distributed Brillouin scattering sensor for discrimination of wall-thinning defects in steel pipe under internal pressure. *Applied Optics*, 43(7):1583–1588, 2004. 3, 4

[6] X. Bao, E. Ponomarev, Y. Li, F. Ravet, L. Zou, and O. M. Sezerman. Distributed Brillouin sensor system based on DFB lasers using offset locking. *United States Patent*, US 7,499,151 B2, 2009. 3

[7] L. Zou and O. M. Sezerman. Method and system for simultaneous measurement of strain and temperature. *United States Patent*, US 7,599,047 B2, 2009. 3

[8] S. C. Huang, W. W. Lin, M. T. Tsai, and M. H. Chen. Fiber optic in-line distributed sensor for detection and localization of the pipeline leaks. *Sensors and Actuators A*, 135:570–579, 2007. 3

[9] R. Bernini, A. Minardo, and L. Zeni. Vectorial dislocation monitoring of pipelines by use of Brillouin-based fiber-optics sensors. *Smart Materials and Structures*, 17(1):015006, 2008. 3

[10] L. Zou, X. Bao, S. Afshar V., and L. Chen. Dependence of the Brillouin frequency shift on strain and temperature in a photonic crystal fiber. *Optics Letters*, 29(13):1485–1487, 2004. 4

[11] L. Zou, X. Bao, Y. Wan, and L. Chen. Coherent probe-pump-based Brillouin sensor for centimeter-crack detection. *Optics Letters*, 30(4):370–372, 2005. 4

[12] W. Li, X. Bao, Y. Li, and L. Chen. Differential pulse-width pair BOTDA for high spatial resolution sensing. *Optics Express*, 16(26):21616–21625, 2008. 4

[13] H. Liang, W. Li, N. linze, L. Chen, and X. Bao. High-resolution DPP-BOTDA over 50 km LEAF using return-to-zero coded pulses. *Optics Letters*, 35(10):1503–1505, 2010. 4

[14] M. Jones. Structural-health monitoring: A sensitive issue. *Nature Photonics*, 2(3):153–154, 2008. 4

[15] X. Bao, C. Zhang, W. Li, M. Eisa, S. El-Gamal, and B. Benmokrane. Monitoring the distributed impact wave on a concrete slab due to the traffic based on polarization dependence on stimulated Brillouin scattering. *Smart Materials and Structures*, 17(1):015003, 2008. 5, 11

[16] X. Bévenot, A. Trouillet, C. Veillas, H. Gagnaire, and M. Clément. Hydrogen leak detection using an optical fibre sensor for aerospace applications. *Sensors and Actuators B*, 67:57–67, 2000. 5

[17] J. C. Juarez and H. F. Taylor. Polarization discrimination in a phase-sensitive optical time-domain reflectometer intrusion-sensor system. *Optics Letters*, 30(24):3284–3286, 2005. 5, 11

[18] J. C. Juarez and H. F. Taylor. Field test of a distributed fiber-optic intrusion sensor system for long perimeters. *Applied Optics*, 46(11):1968–1971, 2007. 5, 11

[19] Z. Zhang and X. Bao. Continuous and damped vibration detection based on fiber diversity detection sensor by Rayleigh backscattering. *Journal of Lightwave Technology*, 26(7):832–838, 2008. 5

[20] Z. Zhang and X. Bao. Distributed optical fiber vibration sensor based on spectrum analysis of polarization-OTDR system. *Optics Express*, 16(14):10240–10247, 2008. 5

[21] Q. Sun, D. Liu, J. Wang, and H. Liu. Distributed fiber-optic vibration sensor using a ring Mach-Zehnder interferometer. *Optics Communications*, 281(6):1538–1544, 2008. 5

[22] É. Pinet. Medical applications: Saving lives. *Nature Photonics*, 2(3):150–152, 2008. 5

[23] M. E. Bosch, A. J. R. Sánchez, F. S. Rojas, and C. B. Ojeda. Recent development in optical fiber biosensors. *Sensors*, 7:797–859, 2007. 6

[24] R. Wolthuis, D. McCrae, E. Saaski, J. Hartl, and G. Mitchell. Development of a medical fiber-optic pH sensor based on optical absorption. *IEEE Transactions on Biomedical Engineering*, 39(5):531–537, 1992. 6

[25] R. A. Wolthuis, D. McCrae, J. C. Hartl, E. Saaski, G. L. Mitchell, K. Garcin, and R. Willard. Development of a medical fiber-optic oxygen sensor based on optical absorption change. *IEEE Transactions on Biomedical Engineering*, 39(2):185–193, 1992. 6

[26] P. A. E. Piunno, U. J. Krull, R. H. E. Hudson, M. J. Damha, and H. Cohen. Fiber optic biosensor for fluorimetric detection of DNA hybridization. *Analytica Chimica Acta*, 288(3):205–214, 1994. 6

[27] P. A. E. Piunno, U. J. Krull, R. H. E. Hudson, M. J. Damha, and H. Cohen. Fiber-Optic DNA sensor for fluorometric nucleic acid determination. *Analytical Chemistry*, 67. 6

[28] Y. Zhang, X. Chen, Y. Wang, K. L. Cooper, and A. Wang. Microgap multicavity Fabry-Pérot biosensor. *Journal of Lightwave Technology*, 25(7):1797–1804, 2007. 6

[29] V. Vali and R. W. Shorthill. Fiber ring interferometer. *Applied Optics*, 15(5):1099–1100, 1976. 6

[30] P. Hariharan. Sagnac or Michaelson-Sagnac interferometer. *Applied Optics*, 14(10):2319–2321, 1975. 6

[31] T. Kumagai, H. Soekawa, T. Yuhara, and H. Kajioka. Fiber optic gyroscopes for vehicle navigation systems. *Proceedings of SPIE*, 2070:181–191, 1994. 6

[32] G. A. Sanders, B. Szafraniec, R. Y. Liu, C. Laskoskie, and L. Strandjord. Fiber optic gyros for space, marine and aviation applications. *Proceedings of SPIE*, 2837:61–71, 1996. 6

[33] G. A. Sanders and B. Szafraniec. Progress in fiber-optic gyroscope applications II with emphasis on the theory of depolarized gyros. *AGARD/NATO Conference Report on Optical Gyros and Their Applications*, 339:11–42, 1998. 6

[34] P. Shajenko, J. P. Flatley, and M. B.Moffett. On fiber-optic hydrophone sensitivity. *Journal of the Acoustical Society of America*, 64(5):1286–1288, 1978. 6

[35] H. L. Price. On the mechanism of transduction in optical fiber hydrophones. *Journal of the Acoustical Society of America*, 66(4):976–979, 1979. 6

[36] A. D. Kersey, M. A. Davis, H. J. Patrick, M. LeBlanc, K. P. Koo, C. G. Askins, M. A. Putnam, and E. J. Friebele. Fiber grating sensors. *Journal of Lightwave Technology*, 15(8):1442–1463, 1997. 10

[37] C. E. Lee, H. F. Taylor, A. M. Markus, and E. Udd. Optical-fiber Fabry-Perot embedded sensor. *Optics Letters*, 14(21):1225–1227, 1989. 10, 11

[38] B. Dong, L. Wei, and D. P. Zhou. Miniature high-sensitivity high-temperature fiber sensor with a dispersion compensation fiber-based interferometer. *Applied Optics*, 48(33):6466–6469, 2009. 10

[39] M. A. Davis, D. G. Bellemore, T. A. Berkoff, and A. D. Kersey. Design amd performance of a fiber Bragg grating distributed strain sensor system. *Proceedings of SPIE*, 2446:227–235, 1995. 11

[40] A. D. Kersey, M. A. Davis, and D. Bellemore. Development of fiber sensors for structural monitoring. *Proceedings of SPIE*, 2456:262–268, 1995. 11

[41] M. G. Xu, H. Geiger, J. L. Archambault, L. Reekie, and J. P. Dakin. Novel interrogating system for fibre Bragg grating sensors using an acousto-optic tunable filter. *Electronics Letters*, 29(17):1510–1511, 1993. 11

[42] M. A. Davis and A. D. Kersey. Matched-filter interrogation technique for fibre Bragg grating arrays. *Electronics Letters*, 31(10):822–823, 1995. 11

[43] A. H. Hartog. A distributed temperature sensor based on liquid-core optical fibers. *Journal of Lightwave Technology*, 1(3):498–509, 1983. 11

[44] J. P. Dakin, D. J. Pratt, G. W. Bibby, and J. N. Ross. Distributed optical fibre Raman temperature sensor using a semiconductor light source and detector. *Electronics Letters*, 21(13):569–570, 1985. 11

[45] X. Bao, D. J. Webb, and D. A. Jackson. 22-km distributed temperature sensor using Brillouin gain in an optical fiber. *Optics Letters*, 18(7):552–554, 1993. 11

[46] O. Frazão, J. M. Baptista, and J. L. Santos. Recent advantages in high-birefringence fiber loop mirror sensors. *Sensors*, 7(11):2970–2983, 2007. 11

References for Chapter 2

[1] R. Kashyap. *Fiber Bragg gratings*. Elsevier Academic Press, San Diego, 1999. 14

[2] K. O. Hill, Y. Fujii, D. C. Johnson, and B. S. Kawasaki. Photosensitivity in optical fiber waveguides: Application to reflection filter fabrication. *Applied Physics Letters*, 32(10):647–649, 1978. 14

[3] J. Stone. Photorefractivity of GeO_2-doped silica fibers. *Journal of Applied Physics*, 62(11):4371–4374, 1987. 14

[4] F. P. Payne. Photorefractive gratings in single-mode optical fibers. *Electronics Letters*, 25(8):498–499, 1989. 14

[5] G. Meltz, W. W. Morey, and W. H. Glenn. Formation of Bragg gratings in optical fibers by a transverse holographic method. *Optics Letters*, 14(15):823–825, 1989. 14

[6] D. P. Hand and P. St. J. Russell. Photoinduced refractive-index changes in germanosilicate fibers. *Optics Letters*, 15(2):102–104, 1990. 14

[7] R. Kashyap. Photosensitive optical fibers: Devices and applications. *Opticical Fiber Technology*, 1(1):17–34, 1994. 14

[8] G. Keiser. *Optical Fiber Communications*. The McGraw-Hill Companies, Inc., United States, 3rd edition, 2000. 15

[9] A. M. Vengsarkar, P. J. Lemaire, J. B. Judkins, V. Bhatia, T. Erdogan, and J. E. Sipe. Long-period fiber gratings as band-rejection filters. In *Tech. Dig. Conf. Opt. Fiber Commun.*, pages Postdeadline paper PD4–2, Sandiego, CA, 1995. 15

[10] A. D. Kersey, M. A. Davis, H. J. Patrick, M. LeBlanc, K. P. Koo, C. G. Askins, M. A. Putnam, and E. J. Friebele. Fiber grating sensors. *Journal of Lightwave Technology*, 15(8):1442–1463, 1997. 16, 19, 22

[11] A. M. Vengsarkar, P. J. Lemaire, J. B. Judkins, V. Bhatia, T. Erdogan, and J. E. Sipe. Long-period fiber gratings as band-rejection filters. *Journal of Lightwave Technology*, 21(1):58–65, 1996. 16

[12] A. M. Vengsarkar, J. R. Pedrazzani, J. B. Judkins, P. J. Lemaire, N. S. Bergano, and C. R. Davidson. Long-period fiber-grating-based gain equalizers. *Optics Letters*, 21(5):336–338, 1996. 16

[13] V. Bhatia and A. M. Vengsarkar. Optical fiber long-period grating sensors. *Optics Letters*, 21(9):692–694, 1996. 16

[14] H. J. Patrick, G. M. Williams, A. D. Kersey, J. R. Pedrazzani, and A. M. Vengsarkar. Hybrid fiber Bragg grating/long period fiber grating sensor for strain/temperature discrimination. *IEEE Photonics Technology Letters*, 8(9):1223–1225, 1996. 16

[15] V. Bhatia, K. A. Murphy, R. O. Claus, and A. M. Vengsarkar. Simultaneous measurement systems employing long-period grating sensors. In *Optical Fiber Sensors*, Sapporo, Japan, paper Fr25, 1996. 16

[16] Y. Y. Shevchenko and J. Albert. Plasmon resonances in gold-coated tilted fiber Bragg gratings. *Optics Letters*, 32(3):211–213, 2007. 16

[17] T. Guo, A. Ivanov, C. Chen, and J. Albert. Temperature-independent tilted fiber grating vibration sensor based on cladding-core recoupling. *Optics Letters*, 33(9):1004–1006, 2008. 16

[18] T. Guo, H. Y. Tam, P. A. Krug, and J. Albert. Reflective tilted fiber Bragg grating refractometer based on strong cladding to core recoupling. *Optics Express*, 17(7):5736–5742, 2009. 16

[19] Y. X. Jin, C. C. Chan, X. Y. Dong, and Y. F. Zhang. Temperature-independent bending sensor with tilted fiber Bragg grating interacting with multimode fiber. *Optics Communications*, 282(19):3905–3907, 2009. 16

[20] F. Ouellette. All-fiber filter for efficient dispersion compensation. *Optics Letters*, 16(5):303–305, 1991. 17

[21] K. C. Byron, K. Sugden, T. Bricheno, and I. Bennion. Fabrication of chirped Bragg gratings in photosensitive fiber. *Electronics Letters*, 29(18):1659–1660, 1993. 17

[22] P. C. Hill and B. J. Eggleton. Strain gradient chirp of fibre Bragg gratings. *Electronics Letters*, 30(14):1172–1174, 1994. 17

[23] M. A. Putnam, G. M. Williams, and E. J. Friebele. Fabrication of tapered, strain-gradient chirped fiber Bragg gratings. *Electronics Letters*, 31(4):309–310, 1995. 17

[24] A. Othonos, X. Lee, and R. M. Measures. Superimposed multiple Bragg gratings. *Electronics Letters*, 30(23):1972–1974, 1994. 17

[25] B. G. Eggleton, P. A. Krug, L. Poladian, and F. Ouellette. Long periodic superstructure Bragg gratings in optical fibres. *Electronics Letters*, 30(19):1620–1622, 1994. 17

[26] L. A. Ferreira, F. M. Araújo, J. L. Santos, and F. Farahi. Simultaneous measurement of strain and temperature using interferometrically interrogated fiber Bragg grating sensors. *Optical Engineering*, 39(8):2226–2234, 2000. 18

[27] S. W. James, M. L. Dockney, and R. P. Tatam. Simultaneous independent temperature and strain measurement using in-fibre Bragg gratings sensors. *Electronics Letters*, 32(12):1133–1134, 1996. 18, 30

[28] P. M. Cavaleiro, A. M. Araújo, L. A. Ferreira, J. L. Santos, and F. Farahi. Simultaneous measurement of strain and temperature using Bragg gratings written in germanosilicate and boron-codoped germanosilicate fibers. *IEEE Photonics Technology Letters*, 11(12):1635–1637, 1999. 18, 30

[29] S. M. Melle, K. Liu, and R. M. Measures. A passive wavelength demodulation system for guided-wave Bragg grating sensors. *IEEE Photonics Technology Letters*, 4(5):516–518, 1992. 22

[30] M. A. Davis and A. D. Kersey. All-fibre Bragg grating strain-sensor demodulation technique using a wavelength division coupler. *Electronics Letters*, 30(1):75–77, 1994. 22

[31] A. B. L. Ribeiro, L. A. Ferreira, M. Tsvetkov, and J. L. Santos. All-fibre interrogation technique for fibre Bragg sensors using a biconical fibre filter. *Electronics Letters*, 32(4):382–383, 1996. 22

[32] S. Chung, J. Kim, B. A. Yu, and B. Lee. A fiber Bragg grating sensor demodulation technique using a polarization maintaining fiber loop mirror. *IEEE Photonics Technology Letters*, 13(12):1343–1345, 2001. 22

[33] R. W. Fallon, L. Zhang, A. Gloag, and I. Bennion. Identical broadband chirped grating interrogation technique for temperature and strain sensing. *Electronics Letters*, 33(8):705–707, 1997. 22

[34] L. Zhang, R. W. Fallon, A. Gloag, I. Bennion, F. W. Haran, and P. Foote. Spatial and wavelength multiplexing architectures for extreme strain monitoring system using identical-chirped-grating-interrogation technique. In *Optical Fiber Sensors*, Williamsburg, VA, paper OThC12, 1997. 22

[35] S. Chen, Y. Hu, L. Zhang, and I. Bennion. Digital spatial and wavelength domain multiplexing of fiber Bragg grating based sensors. In *Optical Fiber Sensors*, Williamsburg, VA, paper OThC11, 1997. 22

[36] Y. Hu, S. Chen, L. Zhang, and I. Bennion. Multiplexing Bragg gratings using combined wavelength and spatial division techniques with digital resolution enhancement. *Electronics Letters*, 33(23):1973–1975, 1997. 22

[37] M. A. Davis and A. D. Kersey. Application of a fiber Fourier transform spectrometer to the detection of wavelength-encoded signals from Bragg grating sensors. *Journal of Lightwave Technology*, 13(7):1289–1295, 1995. 23

[38] D. A. Flavin, R. McBride, and J. D. C. Jones. Short optical path scan interferometric interrogation of a fibre Bragg grating embedded in a composite. *Electronics Letters*, 33(4):319–321, 1997. 23

[39] A. D. Kersey, T. A. Berkoff, and W. W. Morey. Multiplexed fiber Bragg grating strain-sensor system with a fiber Fabry-Perot wavelength filter. *Optics Letters*, 18(16):1370–1372, 1993. 23

[40] M. G. Xu, H. Geiger, and J. P. Dakin. Modeling and performance analysis of a fiber Bragg grating interrogation system using an acousto-optic tunable filter. *Journal of Lightwave Technology*, 14(3):391–396, 1996. 23

[41] D. A. Jackson, A. B. L. Ribeiro, L. Reekie, and J. L. Archambault. Simple multiplexing scheme for a fiber-optic grating sensor network. *Optics Letters*, 18(14):1192–1194, 1993. 23

[42] A. D. Kersey, T. A. Berkoff, and W. W. Morey. High-resolution fibre-grating based strain sensor with interferometric wavelength-shift detection. *Electronics Letters*, 28(3):236–238, 1992. 23

[43] F. T. S. Yu and S. Yin. *Fiber Optic Sensors*. Marcel Dekker, Inc., New York, 2002. 23

[44] C. Fabry and A. Pérot. Interferential measurement in lengths and thickness. *Ann. Chem. Phys*, 16:289, 1899. 23

[45] C. E. Lee and H. F. Taylor. Sensors for smart structures based upon the Fabry-Pérot interferometer. In *Fiber Optic Smart Structures*, pages 249–269, New York, 1995. Wiley. 24

[46] B. H. Verbeek, C. H. Henry, N. A. Olsson, K. J. Orlowsky, R. F. Kazarinov, and B. H. Johnson. Integrated four-channel Mach-Zehnder multi/demultiplexer fabricated with phosphorous doped SiO_2 waveguides on Si. *Journal of Lightwave Technology*, 6(6):1011–1015, 1988. 25

[47] Q. Wang and G. Farrell. All-fiber multimode-interference-based refractometer sensor: proposal and design. *Optics Letters*, 31(3):317–319, 2006. 26

[48] A. Mehta, W. Mohammed, and E. G. Johnson. Multimode interference-based fiber-optic displacement sensor. *IEEE Photonics Technology Letters*, 15(8):1129–1131, 2003. 26

[49] O. Frazão, J. Viegas, P. Caldas, J. L. Santos, F. M. Araújo, L. A. Ferreira, and F. Farahi. All-fiber Mach-Zehnder curvature sensor based on multimode interference combined with a long-period grating. *Optics Letters*, 32(21):3074–3076, 2007. 26

[50] Q. Li, C. H. Lin, P. Y. Tseng, and H. P. Lee. Demonstration of high extinction ratio modal interference in a two-mode fiber and its applications for all-fiber comb filter and high-temperature sensor. *Optics Communications*, 250(4-6):280–285, 2005. 26

[51] W. S. Mohammed, P. W. E. Smith, and X. Gu. All-fiber multimode interference bandpass filter. *Optics Letters*, 31(17):2547–2549, 2006. 26

[52] E. Li. Temperature compensation of multimode-interference-based fiber devices. *Optics Letters*, 32(14):2064–2066, 2007. 26

[53] Y. Liu and L. Wei. Low-cost high-sensitivity strain and temperature sensing using graded-index multimode fibers. *Applied Optics*, 46(13):2516–2519, 2007. 26

[54] D. B. Mortimore. Fiber loop reflectors. *Journal of Lightwave Technology*, 6(7):1217–1224, 1988. 28

[55] M. G. Xu, J. L. Archambault, L. Reekie, and J. P. Dakin. Simultaneous measurement of strain and temperature using fibre grating sensors. *Proceedings of SPIE*, 2360:191–194, 1994. 30

[56] M. G. Xu, J. L. Archambault, L. Reekie, and J. P. Dakin. Discrimination between strain and temperature effects using dual-wavelength fibre grating sensors. *Electronics Letters*, 30(13):1085–1087, 1994. 30

[57] B. O. Guan, H. Y. Tam, S. L. Ho, W. H. Chung, and X. Y. Dong. Simultaneous strain and temperature measurement using a single fibre Bragg grating. *Electronics Letters*, 36(12):1018–1019, 2000. 30

[58] O. Frazão and J. L. Santos. Simultaneous measurement of strain and temperature using a Bragg grating structure written in germanosilicate fibres. *Journal of Optics A: Pure and Applied Optics*, 6(6):553–556, 2004. 30

[59] V. Bhatia, D. Campbell, R. O. Claus, and A. M. Vengsarkar. Simultaneous strain and temperature measurement with long-period gratings. *Optics Letters*, 22(9):648–650, 1997. 30

[60] B. O. Guan, H. Y. Tam, X. M. Tao, and X. Y. Dong. Simultaneous strain and temperature measurement using a superstructure fiber Bragg grating. *IEEE Photonics Technology Letters*, 12(6):675–677, 2000. 30

[61] L. A. Ferreira, A. B. Lobo Ribeiro, J. L. Santos, and F. Farahi. Simultaneous measurement of displacement and temperature using a low finesse cavity and a fiber Bragg grating. *IEEE Photonics Technology Letters*, 8(11):1519–1521, 1996. 30

[62] L. A. Ferreira, A. B. Lobo Ribeiroy, J. L. Santos, and F. Farahi. Simultaneous displacement and temperature sensing using a white light interrogated low finesse cavity in line with a fiber Bragg grating. *Smart Materials and Structures*, 7(2):189–198, 1998. 30

[63] X. Dong, Y. Liu, Z. Liu, and X. Dong. Simultaneous displacement and temperature measurement with cantilever-based fiber Bragg grating sensor. *Optics Communications*, 192(3-6):213–217, 2001. 30

[64] W. Zhang, X. Dong, Q. Zhao, G. Kai, and S. Yuan. FBG-type sensor for simultaneous measurement of force (or displacement) and temperature based on bilateral cantilever beam. *IEEE Photonics Technology Letters*, 13(12):1340–1342, 2001. 30

[65] Y. Yu, H. Tam, W. Chung, and M. S. Demokan. Fiber Bragg grating sensor for simultaneous measurement of displacement and temperature. *Optics Letters*, 25(16):1141–1143, 2000. 30

[66] Y. J. Rao, M. R. Cooper, D. A. Jackson, C. N. Pannell, and L. Reekie. Simultaneous measurement of displacement and temperature using in-fibre-Bragg-grating-based extrinsic Fizeau sensor. *Electronics Letters*, 36(19):1610–1612, 2000. 30

[67] Y. Zhao, Y. Liao, and S. Lai. Simultaneous measurement of down-hole high pressure and temperature with a bulk-modulus and FBG sensor. *IEEE Photonics Technology Letters*, 14(11):1584–1586, 2002. 30

[68] G. Chen, L. Liu, H. Jia, J. Yu, L. Xu, and W. Wang. Simultaneous pressure and temperature measurement using Hi-Bi fiber Bragg gratings. *Optics Communications*, 228(1-3):99–105, 2003. 30

[69] Y. Liu, Z. Guo, Y. Zhang, K. S. Chiang, and X. Dong. Simultaneous pressure and temperature measurement with polymer-coated fibre Bragg grating. *Electronics Letters*, 36(6):564–566, 2000. 30

[70] B. A. L. Gwandu, X. W. Shu, Y. Liu, W. Zhang, L. Zhang, and I. Bennion. Simultaneous measurement of strain and curvature using superstructure fibre Bragg gratings. *Sensors and Actuators A: Physical*, 96(2-3):133–139, 2002. 31

References for Chapter 3

[1] F. Farahi, D. J. Webb, J. D. C. Jones, and D. A. Jackson. Simultaneous measurement of temperature and strain: cross-sensitivity considerations. *Journal of Lightwave Technology*, 8(2):138–142, 1990. 33

[2] W. Jin, W. C. Michie, G. Thursby, M. Konstantaki, and B. Culshaw. Simultaneous measurement of strain and temperature: error analysis. *Optical Engineering*, 36(2):598–609, 1997. 33

[3] M. G. Xu, J. L. Archambault, L. Reekie, and J. P. Dakin. Simultaneous measurement of strain and temperature using fibre grating sensors. *Proceedings of SPIE*, 2360:191–194, 1994. 33

[4] M. G. Xu, J. L. Archambault, L. Reekie, and J. P. Dakin. Discrimination between strain and temperature effects using dual-wavelength fibre grating sensors. *Electronics Letters*, 30(13):1085–1087, 1994. 33

[5] E. Chehura, S. W. James, and R. P. Tatam. Temperature and strain discrimination using a single tilted fibre Bragg grating. *Optics Communications*, 275(2):344–347, 2007. 33

[6] S. W. James, M. L. Dockney, and R. P. Tatam. Simultaneous independent temperature and strain measurement using in-fibre Bragg grating sensors. *Electronics Letters*, 32(12):1133–1134, 1996. 33

[7] P. M. Cavaleiro, F. M. Araújo, L. A. Ferreira, J. L. Santos, and F. Farahi. Simultaneous measurement of strain and temperature using Bragg gratings written in germanosilicate and boron-codoped germanosilicate fibers. *IEEE Photonics Technology Letters*, 11(12):1635–1637, 1999. 33

[8] B. O. Guan, H. Y. Tam, H. L. W. Chan, C. L. Choy, and M. S. Demokan. Discrimination between strain and temperature with a single fiber Bragg grating. *Microwave and Optical Technology Letters*, 33(3):200–202, 2002. 33

[9] O. Frazão and J. L. Santos. Simultaneous measurement of strain and temperature using a Bragg grating structure written in germanosilicate fibres. *Journal of Optics A: Pure and Applied Optics*, 6(6):553–556, 2004. 33, 38

[10] H. J. Patrick, G. M. Williams, A. D. Kersey, J. R. Pedrazzani, and A. M. Vengsarkar. Hybrid fiber Bragg grating/long period fiber grating sensor for strain/temperature discrimination. *IEEE Photonics Technology Letters*, 8(9):1223–1225, 1996. 33

[11] B. O. Guan, H. Y. Tam, X. M. Tao, and X. Y. Dong. Simultaneous strain and temperature measurement using a superstructure fiber Bragg grating. *IEEE Photonics Technology Letters*, 12(6):675–677, 2000. 33, 36

[12] O. Frazão, R. Romero, G. Rego, P. V. S. Marques, H. M. Salgado, and J. L. Santos. Sampled fibre Bragg grating sensors for simultaneous strain and temperature measurement. *Electronics Letters*, 38(14):693–695, 2002. 33

[13] O. Frazão, L. M. Marques, and J. M. Baptista. Fibre Bragg grating interrogation based on high-birefringence fibre loop mirror for strain-temperature discrimination. *Microwave and Optical Technology Letters*, 48(11):2326–2328, 2006. 33

[14] O. Frazão, L. A. Ferreira, F. M. Araújo, and J. L. Santos. Appications of fiber optic grating technology to multi-parameter measurement. *Fiber and Integrated Optics*, 24(3&4):227–244, 2005. 33, 51

[15] Q. Wang and G. Farrell. All-fiber multimode-interference-based refractometer sensor: proposal and design. *Optics Letters*, 31(3):317–319, 2006. 34

[16] A. Mehta, W. Mohammed, and E. G. Johnson. Multimode interference-based fiber-optic displacement sensor. *IEEE Photonics Technology Letters*, 15(8):1129–1131, 2003. 34

[17] O. Frazão, J. Viegas, P. Caldas, J. L. Santos, F. M. Araújo, L. A. Ferreira, and F. Farahi. All-fiber Mach-Zehnder curvature sensor based on multimode interference combined with a long-period grating. *Optics Letters*, 32(21):3074–3076, 2007. 34

[18] Q. Li, C. H. Lin, P. Y. Tseng, and H. P. Lee. Demonstration of high extinction ratio modal interference in a two-mode fiber and its applications for all-fiber comb filter and high-temperature sensor. *Optics Communications*, 250(4-6):280–285, 2005. 34

[19] W. S. Mohammed, P. W. E. Smith, and X. Gu. All-fiber multimode interference bandpass filter. *Optics Letters*, 31(17):2547–2549, 2006. 34

[20] E. Li. Temperature compensation of multimode-interference-based fiber devices. *Optics Letters*, 32(14):2064–2066, 2007. 34

[21] Y. Liu and L. Wei. Low-cost high-sensitivity strain and temperature sensing using graded-index multimode fibers. *Applied Optics*, 46(13):2516–2519, 2007. 34

[22] D. P. Zhou, L. Wei, W. K. Liu, Y. Liu, and J. W. Y. Lit. Simultaneous measurement for strain and temperature using fiber Bragg gratings and multimode fibers. *Applied Optics*, 47(10):1668–1672, 2008. 34, 45, 46, 47, 51

[23] S. M. Melle, K. Liu, and R. M. Measures. A passive wavelength demodulation system for guided-wave Bragg grating sensors. *IEEE Photonics Technology Letters*, 4(5):516–518, 1992. 34, 35, 45, 51

[24] M. A. Davis and A. D. Kersey. All-fibre Bragg grating strain-sensor demodulation technique using a wavelength division coupler. *Electronics Letters*, 30(1):75–77, 1994. 34, 35, 51

[25] A. B. L. Ribeiro, L. A. Ferreira, M. Tsvetkov, and J. L. Santos. All-fibre interrogation technique for fibre Bragg sensors using a biconical fibre filter. *Electronics Letters*, 32(4):382–383, 1996. 34, 35, 45, 51

[26] S. Chung, J. Kim, B. A. Yu, and B. Lee. A fiber Bragg grating sensor demodulation technique using a polarization maintaining fiber loop mirror. *IEEE Photonics Technology Letters*, 13(12):1343–1345, 2001. 34, 35, 51

[27] A. D. Kersey, M. A. Davis, H. J. Patrick, M. LeBlanc, K. P. Koo, C. G. Askins, M. A. Putnam, and E. J. Friebele. Fiber grating sensors. *Journal of Lightwave Technology*, 15(8):1442–1463, 1997. 34, 51

[28] A. D. Kersey, T. A. Berkoff, and W. W. Morey. Multiplexed fiber Bragg grating strain-sensor system with a fiber Fabry-Perot wavelength filter. *Optics Letters*, 18(16):1370–1372, 1993. 34, 51

[29] M. A. Davis, D. G. Bellemore, M. A. Putnam, and A. D. Kersey. Interrogation of 60 fibre Bragg grating sensors with microstrain resolution capability. *Electronics Letters*, 32(15):1393–1394, 1996. 34, 51

[30] A. D. Kersey and T. A. Berkoff. Fiber-optic Bragg-grating differential-temperature sensor. *IEEE Photonics Technology Letters*, 4(10):1183–1185, 1992. 34, 51

[31] P. Sivanesan, J. S. Sirkis, Y. Murata, and S. G. Buckley. Optimal wavelength pair selection and accuracy analysis of dual fiber grating sensors for simultaneously measuring strain and temperature. *Optical Engineering*, 41(10):2456–2463, 2002. 42

References for Chapter 4

[1] M. G. Xu, J. L. Archambault, L. Reekie, and J. P. Dakin. Discrimination between strain and temperature effects using dual-wavelength fibre grating sensors. *Electronics Letters*, 30(13):1085–1087, 1994. 52

[2] E. Chehura, S. W. James, and R. P. Tatam. Temperature and strain discrimination using a single tilted fibre Bragg grating. *Optics Communications*, 275(2):344–347, 2007. 52

[3] D. P. Zhou, L. Wei, W. K. Liu, Y. Liu, and J. W. Y. Lit. Simultaneous measurement for strain and temperature using fiber Bragg gratings and multimode fibers. *Applied Optics*, 47(10):1668–1672, 2008. 52, 53, 56

[4] O. Frazão, L. M. Marques, S. Santos, J. M. Baptista, and J. L. Santos. Simultaneous measurement for strain and temperature based on a long-period grating combined with a high-birefringence fiber loop mirror. *IEEE Photonics Technology Letters*, 18(22):2407–2409, 2006. xii, 52, 53, 60, 65, 66

[5] O. Frazão, L. A. Ferreira, F. M. Araújo, and J. L. Santos. Applications of fiber optic grating technology to multi-parameter measurement. *Fiber and Integrated Optics*, 24(3&4):227–244, 2005. 52, 53, 54

[6] S. Li, K. S. Chiang, and W. A. Gambling. Gain flattening of an erbium-doped fiber amplifier using a high-birefringence fiber loop mirror. *IEEE Photonics Technology Letters*, 13(9):942–944, 2001. 52

[7] S. Kim and J. U. Kang. Polarization-independent figure-eight birefringent Sagnac variable comb-filter/attenuator. *IEEE Photonics Technology Letters*, 16(2):494–496, 2004. 52

[8] X. P. Dong, S. Li, K. S. Chiang, M. N. Ng, and B. C. B. Chu. Multiwavelength erbium-doped fibre laser based on a high-birefringence fibre loop mirror. *Electronics Letters*, 36(19):1609–1610, 2000. 52

[9] M. Campbell, G. Zheng, A. S. Holmes-Smith, and P. A. Wallace. A frequency-modulated continuous wave birefringent fibre-optic strain sensor based on a Sagnac ring configuration. *Measurement Science and Technology*, 10(3):218–224, 1999. 52

[10] E. De la Rosa, L. A. Zenteno, A. N. Starodumov, and D. Monzon. All-fiber absolute temperature sensor using an unbalanced high-birefringence Sagnac loop. *Optics Letters*, 22(7):481–483, 1997. 53

[11] Y. Liu, B. Liu, X. Feng, W. Zhang, G. Zhou, S. Yuan, G. Kai, and X. Dong. High-birefringence fiber loop mirrors and their applications as sensors. *Applied Optics*, 44(12):2382–2390, 2005. 53, 58

[12] D. Bo, Z. Qida, L. Feng, G. Tuan, X. Lifang, L. Shuhong, and G. Hong. Liquid-level sensor with a high-birefringence-fiber loop mirror. *Applied Optics*, 45(30):7767–7771, 2006. 53

[13] G. Sun, D. S. Moon, and Y. Chung. Simultaneous temperature and strain measurement using two types of high-birefringence fibers in Sagnac loop mirror. *IEEE Photonics Technology Letters*, 19(24):2027–2029, 2007. 53

[14] O. Frazão, J. L. Santos, and J. M. Baptista. Strain and temperature discrimination using concatenated high-birefringence fiber loop mirrors. *IEEE Photonics Technology Letters*, 19(16):1260–1262, 2007. 53

[15] H. J. Patrick, G. M. Williams, A. D. Kersey, J. R. Pedrazzani, and A. M. Vengsarkar. Hybrid fiber Bragg grating/long period fiber grating sensor for strain/temperature discrimination. *IEEE Photonics Technology Letters*, 8(9):1223–1225, 1996. 53, 65

[16] S. M. Melle, K. Liu, and R. M. Measures. A passive wavelength demodulation system for guided-wave Bragg grating sensors. *IEEE Photonics Technology Letters*, 4(5):516–518, 1992. 53, 54

[17] M. A. Davis and A. D. Kersey. All-fibre Bragg grating strain-sensor demodulation technique using a wavelength division coupler. *Electronics Letters*, 30(1):75–77, January 1994. 53, 54

[18] A. B. L. Ribeiro, L. A. Ferreira, M. Tsvetkov, and J. L. Santos. All-fiber interrogation technique for fibre Bragg sensors using a biconical fibre filter. *Electronics Letters*, 32(4):382–383, 1996. 53, 54

[19] S. Chung, J. Kim, B. A. Yu, and B. Lee. A fiber Bragg grating sensor demodulation technique using a polarization maintaning fiber loop mirror. *IEEE Photonics Technology Letters*, 13(12):1343–1345, 2001. 53, 54

[20] A. D. Kersey, M. A. Davis, H. J. Patrick, M. LeBlanc, K. P. Koo, C. G. Askins, M. A. Putnam, and E. J. Friebele. Fiber grating sensors. *Journal of Lightwave Technology*, 15(8):1442–1463, 1997. 53, 54

[21] A. D. Kersey, T. A. Berkoff, and W. W. Morey. Multiplexed fiber Bragg grating strain-sensor system with a fiber Fabry-Perot wavelength filter. *Optics Letters*, 18(16):1370–1372, 1993. 53, 54

[22] M. A. Davis, D. G. Bellemore, M. A. Putnam, and A. D. Kersey. Interrogation of 60 fiber Bragg grating sensors with microstrain resolution capability. *Electronics Letters*, 32(15):1393–1394, 1996. 53, 54

[23] A. D. Kersey and T. A. Berkoff. Fiber-optic Bragg-grating differential-temperature sensor. *IEEE Photonics Technology Letters*, 4(10):1183–1185, 1992. 53, 54

[24] W. Jin, W. C. Michie, G. Thursby, M. Konstantaki, and B. Culshaw. Simultaneous measurement of strain and temperature: error analysis. *Optical Engineering*, 36(2):598–609, 1997. 56

[25] D. P. Zhou, L. Wei, W. K. Liu, and J. W. Y. Lit. Simultaneous measurement of strain and temperature based on a fiber Bragg grating combined with a high-birefrigence fiber loop mirror. *Optics Communications*, 281(18):4640–4643, 2008. 65, 66, 68

[26] D. P. Zhou, L. Wei, W. K. Liu, and J. W. Y. Lit. Simultaneous strain and temperature measurement with fiber Bragg grating and multimode fibers using an intensity-based interrogation method. *IEEE Photonics Technology Letters*, 21(7):468–470, 2009. 69

References for Chapter 5

[1] W. Zhang, X. Dong, Q. Zhao, G. Kai, and S. Yuan. FBG-Type Sensor for simultaneous measurement of force (or displacement) and temperature based on bilateral cantilever beam. *IEEE Photonics Technology Letters*, 13(12):1340–1342, 2001. 73

[2] L. Xue, Q. Zhao, J. Liu, G. Huang, T. Guo, and X. Dong. Force sensing with temperature self-compensated based on a loop thin-wall section beam. *IEEE Photonics Technology Letters*, 18(1):271–273, 2006. 73

[3] B. Dong, Q. Zhao, L. Zhao, L. Jin, Y. Miao, T. Liao, and X. Zeng. Simultaneous measurement of temperature and force based on a special-strain-function-chirped FBG. *Sensors and Actuators A: Physical*, 147(1):169–172, 2008. 73

[4] J. Hao, Z. Cai, J. H. Ng, Y. Gong, and P. Varghese. Simultaneous temperature and lateral force measurement using simple arc-shaped FBG sensor module. *Electronics Letters*, 42(25):1446–1447, 2006. 73

[5] S. Takahashi, J. Z. Hao, Y. W. A. Lee, Z. Cai, T. T. Do, and B. Y. R. Ng. Effect of bending methods on FBG lateral force sensor. *Electronics Letters*, 41(23):1270–1271, 2005. 73

[6] K. S. Lau, X. L. Chan, and K. M. Wong. Force measurement by visibility modulated fiber optic sensor. *Applied Optics*, 38(34):7163–7164, 1999. 73

[7] H. Shanglian, L. Fei, and P. Yingjun. A fiber optic sensor for measuring distributed forces. *Journal of Intelligent Material Systems and Structures*, 5(3):427–431, 1994. 73

[8] J. Canning and A. L. G. Carter. Modal interferometer for *in situ* measurements of induced core index change in optical fibers. *Optics Letters*, 22(8):561–563, 1997. 73

[9] Y. Liu and L. Wei. Low-cost high-sensitivity strain and temperature sensing using graded-index multimode fibers. *Applied Optics*, 46(13):2516–2519, 2007. 73, 74, 76, 79, 92, 96

[10] L. V. Nguyen, D. Hwang, S. Moon, D. S. Moon, and Y. Chung. High temperature fiber sensor with high sensitivity based on core diameter mismatch. *Optics Express*, 16(15):11369–11375, 2008. 73, 75

[11] E. Li, X. Wang, and C. Zhang. Fiber-optic temperature sensor based on interference of selective higher-order modes. *Applied Physics Letters*, 89(9):091119, 2006. 73, 76, 79, 92, 96, 97

[12] E. Li. Temperature compensation of multimode-interference-based fiber devices. *Optics Letters*, 32(14):2064–2066, July 2007. 73, 92

[13] E. Li. Sensitivity-enhanced fiber-optic strain sensor based on interference of higher order modes in circular fibers. *IEEE Photonics Technology Letters*, 19(16):1266–1268, 2007. 73, 74

[14] D. P. Zhou, L. Wei, W. K. Liu, Y. Liu, and J. W. Y. Lit. Simultaneous measurement for strain and temperature using fiber bragg gratings and multimode fibers. *Applied Optics*, 47(10):1668–1672, 2008. 73

[15] B. G. Grossmann and L. T. Huang. Fiber optic sensor array for multi-dimensional strain measurement. *Smart Materials and Structures*, 7(2):159–165, 1998. 74

[16] L. Yuan, Q. Li, Y. Liang, J. Yang, and Z. Liu. Fiber optic 2-D sensor for measuring the strain inside the concrete specimen. *Sensors and Actuators A: Physical*, 94(1-2):25–31, 2001. 74

[17] B. Dong, D. P. Zhou, L. Wei, W. K. Liu, and J. W. Y. Lit. Temperature- and phase-independent lateral force sensor based on a core-offset multi-mode fiber interferometer. *Optics Express*, 16(23):19291–19296, 2008. 74, 83, 84, 92, 94

[18] C. Belleville and G. Duplain. White-light interferometric multimode fiber-optic strain sensor. *Optics Letters*, 18(1):78–80, 1993. 74

[19] S. M. Melle, K. Liu, and R. M. Measures. A passive wavelength demodulation system for guided-wave Bragg grating sensors. *IEEE Photonics Technology Letters*, 4(5):516–518, 1992. 75

[20] M. A. Davis and A. D. Kersey. All-fibre Bragg grating strain-sensor demodulation technique using a wavelength division coupler. *Electronics Letters*, 30(1):75–77, 1994. 75

[21] A. B. L. Ribeiro, L. A. Ferreira, M. Tsvetkov, and J. L. Santos. All-fibre interrogation technique for fibre Bragg sensors using a biconical fibre filter. *Electronics Letters*, 32(4):382–383, 1996. 75

[22] S. Chung, J. Kim, B. A. Yu, and B. Lee. A fiber Bragg grating sensor demodulation technique using a polarization maintaning fiber loop mirror. *IEEE Photonics Technology Letters*, 13(12):1343–1345, 2001. 75

[23] A. D. Kersey, M. A. Davis, H. J. Patrick, M. LeBlanc, K. P. Koo, C. G. Askins, M. A. Putnam, and E. J. Friebele. Fiber grating sensors. *Journal of Lightwave Technology*, 15(8):1442–1463, 1997. 75

[24] A. D. Kersey, T. A. Berkoff, and W. W. Morey. Multiplexed fiber Bragg grating strain-sensor system with a fiber Fabry-Perot wavelength filter. *Optics Letters*, 18(16):1370–1372, 1993. 75

[25] M. A. Davis, D. G. Bellemore, M. A. Putnam, and A. D. Kersey. Interrogation of 60 fiber Bragg grating sensors with microstrain resolution capability. *Electronics Letters*, 32(15):1393–1394, 1996. 75

[26] A. D. Kersey and T. A. Berkoff. Fiber-optic Bragg-grating differential-temperature sensor. *IEEE Photonics Technology Letters*, 4(10):1183–1185, 1992. 75

[27] X. Chen, F. Shen, Z. Wang, Z. Huang, and A. Wang. Micro-air-gap based intrinsic Fabry-Perot interferometric fiber-optic sensor. *Applied Optics*, 45(30):7760–7766, 2006. 75

[28] T. Wei, Y. Han, H. L. Tsai, and H. Xiao. Miniaturized fiber inline Fabry-Perot interferometer fabricated with a femtosecond laser. *Optics Letters*, 33(6):536–538, 2008. 75

[29] H. Y. Choi, K. S. Park, S. J. Park, U. C. Paek, B. H. Lee, and E. S. Choi. Miniature fiber-optic high temperature sensor based on a hybrid structured Fabry-Perot interferometer. *Optics Letters*, 33(21):2455–2457, 2008. 75

[30] T. Guo, A. Ivanov, C. Chen, and J. Albert. Temperature-independent tilted fiber grating vibration sensor based on cladding-core recoupling. *Optics Letters*, 33(9):1004–1006, 2008. 77

[31] S. C. Rashleigh. Origins and control of polarization effects in single-mode fibers. *Journal of Lightwave Technology*, 1(2):312–331, 1983. 79

References for Chapter 6

[1] Y. Liu and L. Wei. Low-cost high-sensitivity strain and temperature sensing using graded-index multimode fibers. *Applied Optics*, 46(13):2516–2519, 2007. 100, 102

[2] B. Dong, D. P. Zhou, L. Wei, W. K. Liu, and J. W. Y. Lit. Temperature- and phase-independent lateral force sensor based on a core-offset multi-mode fiber interferometer. *Optics Express*, 16(23):19291–19296, 2008. 100, 102

[3] B. Dong, L. Wei, D. P. Zhou, W. K. Liu, and J. W. Y. Lit. Core-offset small-core-diameter dispersion compensation fiber interferometer and its applications in fiber sensors. *Applied Optics*, 48(23):4577–4581, 2009. 100

[4] J. Hao, Z. Cai, J. H. Ng, Y. Gong, and P. Varghese. Simultaneous temperature and lateral force measurement using simple arc-shaped FBG sensor module. *Electronics Letters*, 42(25):1446–1447, 2006. 101

[5] S. Takahashi, J. Z. Hao, Y. W. A. Lee, Z. Cai, T. T. Do, and B. Y. R. Ng. Effect of bending methods on FBG lateral force sensor. *Electronics Letters*, 41(23):1270–1271, 2005. 101, 102

[6] X. Dong, H. Y. Tam, and P. Shum. Temperature-insensitive strain sensor with polarization-maintaining photonic crystal fiber based Sagnac interferometer. *Applied Physics Letters*, 90(15):151113, 2007. 101, 102, 105

[7] E. De la Rosa, L. A. Zenteno, A. N. Starodumov, and D. Monzon. All-fiber absolute temperature sensor using an unbalanced high-birefringence Sagnac loop. *Optics Letters*, 22(7):481–483, 1997. 101

[8] Y. Liu, B. Liu, X. Feng, W. Zhang, G. Zhou, S. Yuan, G. Kai, and X. Dong. High-birefringence fiber loop mirrors and their applications as sensors. *Applied Optics*, 44(12):2382–2390, 2005. 101

[9] D. Bo, Z. Qida, L. Feng, G. Tuan, X. Lifang, L. Shuhong, and G. Hong. Liquid-level sensor with a high-birefringence-fiber loop mirror. *Applied Optics*, 45(30):7767–7771, 2006. 101

[10] B. J. Eggleton, P. S. Westbrook, C. A. White, C. Kerbage, R. S. Windeler, and G. L. Burdge. Cladding-mode-resonances in air-silica microstructure optical fibers. *Journal of Lightwave Technology*, 18(8):1084–1100, 2000. 102

[11] J. G. Liu, L. F. Xue, G. Y. Kai, Y. G. Liu, W. G. Zhang, Y. Li, Z. Wang, C. S. Zhang, and X. Y. Dong. Mode exciting propertities of photonic crystal fiber with optical field

incident from a single mode fibre. *Chinese Physics Letters*, 23(8):2125–2128, 2006. 102

[12] J. Liu, L. Xue, Z. Wang, G. Kai, Y. Liu, W. Zhang, and X. Dong. Large anomalous dispersion at short wavelength and modal properties of a photonic crystal fiber with large air holes. *IEEE Journal of Quantum Electronics*, 42(9):961–968, 2006. 102

References for Chapter 7

[1] L. Zou, X. Bao, Y. Wan, and L. Chen. Coherent probe-pump-based Brillouin sensor for centimeter-crack detection. *Optics Letters*, 30(4):370–372, 2005. 108, 109

[2] T. Kurashima, T. Horiguchi, and M. Tateda. Distributed-temperature sensing using stimulated Brillouin scattering in optical silica fibers. *Optics Letters*, 15(18):1038–1040, 1990. 108

[3] X. Bao, D. J. Webb, and D. A. Jackson. 22-km distributed temperature sensor using Brillouin gain in an optical fiber. *Optics Letters*, 18(7):552–554, 1993. 108

[4] X. Bao, D. J. Webb, and D. A. Jackson. 32-km distributed temperature sensor based on Brillouin loss in an optical fiber. *Optics Letters*, 18(18):1561–1563, 1993. 108

[5] L. Zou, X. Bao, S. Afshar V., and L. Chen. Dependence of the Brillouin frequency shift on strain and temperature in a photonic crystal fiber. *Optics Letters*, 29(13):1485–1487, 2004. 109

[6] L. Zou, X. Bao, S. Yang, L. Chen, and F. Ravet. Effect of Brillouin slow light on distributed Brillouin fiber sensors. *Optics Letters*, 31(18):2698–2700, 2006. 109

[7] W. Li, X. Bao, Y. Li, and L. Chen. Differential pulse-width pair BOTDA for high spatial resolution sensing. *Optics Express*, 16(26):21616–21625, 2008. 109, 124

[8] H. Liang, W. Li, N. Linze, L. Chen, and X. Bao. High-resolution DPP-BOTDA over 50 km LEAF using return-to-zero coded pulses. *Optics Letters*, 35(10):1503–1505, 2010. 109, 124

[9] W. Jin, W. C. Michie, G. Thursby, M. Konstantaki, and B. Culshaw. Simultaneous measurement of strain and temperature: error analysis. *Optical Engineering*, 36(2):598–609, 1997. 109

[10] L. Zou and O. M. Sezerman. Method and system for simultaneous measurement of strain and temperature. *United States Patent*, No.:US 7,599,047 B2. 109

[11] C. C. Lee, P. W. Chiang, and S. Chi. Utilization of a dispersion-shifted fiber for simultaneous measurement of distributed strain and temperature through Brillouin frequency shift. *IEEE Photonics Technology Letters*, 13(10):1094–1096, 2001. 109

[12] X. Bao, Q. Yu, and L. Chen. Simultaneous stain and temperature measurements with polarization-maintaining fibers and their error analysis by use of a distributed Brillouin loss system. *Optics Letters*, 29(12):1342–1344, 2004. 109

[13] W. Zou, Z. He, and K. Hotate. Complete discrimination of strain and temperature using Brillouin frequency shift and birefringence in a polarization-maintaining fiber. *Optics Express*, 17(3):1248–1255, 2009. 109, 110

[14] K. Y. Song, W. Zou, Z. He, and K. Hotate. All-optical dynamic grating generation based on Brillouin scattering in polarization-maintaining fiber. *Optics Letters*, 33(9):926–928, 2008. 109, 110

[15] K. Y. Song, W. Zou, Z. He, and K. Hotate. Optical time-domain measurement of Brillouin dynamic grating spectrum in a polarization-maintaining fiber. *Optics Letters*, 34(9):1381–1383, 2009. 109, 110

[16] Y. Dong, X. Bao, and L. Chen. Distributed temperature sensing based on birefringence effect on transient Brillouin grating in a polarization-maintaining photonic crystal fiber. *Optics Letters*, 34(17):2590–2592, 2009. 109, 110

[17] K. Y. Song and H. J. Yoon. High-resolution Brillouin optical time domain analysis based on Brillouin dynamic grating. *Optics Letters*, 35(1):52–54, 2010. 109, 110

[18] Y. Dong, L. Chen, and X. Bao. Truly distributed birefringence measurement of polarization-maintaining fibers based on transient Brillouin grating. *Optics Letters*, 35(2):193–195, 2010. 109, 110

[19] Y. Dong, L. Chen, and X. Bao. High-spatial-resolution time domain simultaneous strain and temperature sensor using Brillouin scattering and birefringence in a polarization-maintaining fiber. *IEEE Photonics Technology Letters*, 22(18):1364–1366, 2010. 110

[20] Y. Dong, L. Chen, and X. Bao. Characterization of the Brillouin grating spectra in a polarization-maintaining fiber. *Optics Express*, 18(8):18960–18967, 2010. 110

[21] V. N. Filippov, A. N. Starodumov, and A. V. Kir'yanov. All-fiber passively Q-switched low-threshold erbium laser. *Optics Letters*, 26(6):343–345, 2001. 111

[22] M. Laroche, A. M. Chardon, J. Nilsson, D. P. Shepherd, W. A. Clarkson, S. Girard, and R. Moncorgẽ. All-fiber passively Q-switched low-threshold erbium laser. *Optics Letters*, 26(6):343–345, 2001. 111

[23] V. Philippov, J. Nilsson, W. A. Clarkson, A. Abdolvand, V. E. Kisel, V. G. Shcherbitsky, N. V. Kuleshov, V. I. Konstantinov, and V. I. Levchenko. Passively Q-switched Er-Yb double clad fiber laser with Cr^{2+}:ZnSe and Co^{2+}:$MgAl_2O_4$ as a saturable absorber. *Proceedings of SPIE*, 5335:8–15, 2004. 111

[24] J. B. Lecourt, G. Martel, M. Guẽzo, C. Labbẽ, and S. Loualiche. Erbium-doped fiber laser passively Q-switched by an InGaAs/InP multiple quantum well saturable absorber. *Optics Communications*, 263(1):71–83, 2006. 111

[25] J. Y. Huang, S. C. Huang, H. L. Chang, K. W. Su, Y. F. Chen, and K. F. Huang. Passive Q-switching of Er-Yb fiber laser with semiconductor saturable absorber. *Optics Express*, 16(5):3002–3007, 2008. 111

[26] S. Y. Set, H. Yaguchi, Y. Tanaka, M. Jablonski, Y. Sakakibara, M. Tokumoto, H. Kataura, Y. Achiba, and K. Kikuchi. A dual-regime mode-locked/Q-switched laser using a saturable absorber incorporating carbon nanotubes. *Proc. CELO'03*, 16(5):3002–3007, 2008. 111

[27] K. Kieu and M. Mansuripur. Femtosecond laser pulse generation with a fiber taper embedded in carbon nanotube/polymer composite. *Optics Letters*, 32(15):2242–2244, 2007. 111

[28] Y. W. Song, S. Yamashita, and S. Maruyama. Single-walled carbon nanotubes for high-energy optical pulse formation. *Applied Physics Letters*, 92(2):021115, 2008. 111, 116

[29] F. Wang, A. G. Rozhin, V. Scardaci, Z. Sun, F. Hennrich, I. H. White, W. I. Milne, and A. C. Ferrari. Wideband-tuneable, nanotube modelocked, fiber laser. *Nature Nanotechnology*, 3(12):738–742, 2008. 111

[30] J. W. Nicholson, R. S. Windeler, and D. J. DiGiovanni. Optically driven deposition of single-walled carbon-nanotube saturable absorbers on optical fiber end-faces. *Optics Express*, 15(15):9176–9183, 2007. 111, 112

[31] K. H. Lin, J. J. Kang, H. H. Wu, C. K. Lee, and C. R. Lin. Manipulation of operation states by polarization control in an erbium-doped fiber laser with a hybrid saturable absorber. *Optics Express*, 17(6):4806–4814, 2009. 114

[32] Y. W. Song, S. A. Havstad, D. Starodubov, Y. Xie, A. E. Willner, and J. Feinberg. 40-nm-wide tunable fiber ring laser with single-mode operation using a highly stretchable FBG. *IEEE Photonics Technology Letters*, 13(11):1167–1169, 2001. 116

[33] M. E. Fermann, A. Galvanauskas, and G. Sucha. *Ultrafast lasers: technology and applications*. Marcel Dekker, Inc, 2003. 116

[34] F. Ö. Ilday, J. R. Buckley, W. G. Clark, and E. W. Wise. Self-similar evolution of parabolic pulses in a laser. *Physical Review Letters*, 92(21):213902, 2004. 117, 119

[35] M. E. Fermann and I. Hartl. Ultrafast fiber laser technology. *IEEE Journal of Selected Topics in Quantum Electronics*, 15(1):191–206, 2009. 117

[36] L. M. Zhao, D. Y. Tang, T. H. Cheng, and C. Lu. Gain-guided solitons in dispersion-managed fiber lasers with large net cavity dispersion. *Optics Letters*, 31(20):2957–2959, 2006. 117

[37] L. M. Zhao, D. Y. Tang, and J. Wu. Gain-guided solitons in a positive group-dispersion fiber laser. *Optics Letters*, 31(12):1788–1790, 2006. 117

[38] L. M. Zhao, D. Y. Tang, H. Zhang, T. H. Cheng, H. Y. Tam, and C. Lu. Dynamics of gain-guided solitons in an all-normal-dispersion fiber laser. *Optics Letters*, 32(13):1806–1808, 2007. 117

[39] W. H. Renninger A. Chong and F. W. Wise. Properties of normal-dispersion femtosecond fiber lasers. *Journal of the Optical Society of America B*, 25(2):140–148, 2008. 117

[40] K. Kieu and F. W. Wise. All-fiber normal-dispersion femtosecond laser. *Optics Express*, 16(15):11453–11458, 2008. 117

[41] X. Liu. Dissipative soliton evolution in ultr-large normal-cavity-dispersion fiber lasers. *Optics Express*, 17(12):9549–9557, 2009. 117

[42] A. Cabasse, G. Martel, and J. L. Oudar. High power dissipative soliton in an erbium-doped fiber laser mode-locked with a high modulation depth saturable absorber mirror. *Optics Express*, 17(12):9537–9542, 2009. 117

[43] Z. Sun, A. G. Rozhin, F. Wang, T. Hasan, D. Popa, W. O'Neill, and A. C. Ferrari. A compact, high power, ultrafast laser mode-locked by carbon nanotubes. *Applied Physics Letters*, 95(25):253102, 2009. 117

[44] G. P. Agrawal. *Nonlinear Fiber Optics*. Academic Press, 4th edition, 2007. 118, 124

[45] G. P. Agrawal. *Applications of Nonlinear Fiber Optics*. Academic Press, 2001. 119, 120

[46] R. W. Boyd. *Nonlinear Optics*. Academic Press, 3rd edition, 2003. 124